POLITECNICO DI TORINO

Collegio di Ingegneria Chimica e dei Materiali

Master of Science Course
in Materials Engineering for Industry 4.0

Laser Powder Directed Energy Deposition of C103 Niobium Alloy: Process Development



Advisor
Prof. Abdollah Saboori

Candidate
Jacopo Ciccarelli
s346874

Tutor
Ing. John Stavridis

September 2026

Abstract

C103 is a niobium-based refractory alloy widely employed in aerospace propulsion systems, particularly for rocket nozzle extensions, owing to its excellent high-temperature mechanical properties and relatively low density. However, the manufacture of C103 components through conventional processing routes, such as machining, forging, and casting, remains challenging because of the alloy's poor machinability, long production lead times, and high material waste. In this context, Laser Powder Directed Energy Deposition (LP-DED) represents a promising alternative for the fabrication of large and geometrically complex C103 components.

This thesis investigates the development of suitable LP-DED process parameters for the manufacture of C103 alloy. The experimental campaign was designed following a comprehensive literature review on LP-DED technology, niobium alloys, and the processing of C103 by laser powder DED. Process development followed a progressive optimization strategy, beginning with single-track experiments to identify suitable combinations of laser power, scanning speed, and powder feed rate. The selected parameters were subsequently validated through the manufacture of cubic specimens, whose relative density was assessed by metallographic image analysis. Based on the experimental results, the process parameters were iteratively refined to reduce porosity and improve deposition quality, ultimately identifying a process parameter set capable of producing C103 components with an average relative density of 99.50%.

The developed process was further proven through the manufacture of a tensile specimen and a representative case-study component. Although the tensile specimen was produced using an intermediate parameter set, before completion of the optimization procedure, the measured yield strength and ultimate tensile strength satisfied the requirements, whereas the elongation at failure remained limited to approximately 3%. Finally, the successful manufacture of the case-study component demonstrated the feasibility of producing C103 alloy components by LP-DED.

Acknowledgment

I would like to express my sincere gratitude to my advisor, Professor Abdollah Saboori, for his guidance, support, and valuable advice throughout the development of this thesis. His expertise and constructive feedback were fundamental to the progress of this work and to my growth as an engineer.

I would also like to express my deepest gratitude to AltForm for giving me the opportunity to turn my passion for Additive Manufacturing into a real professional experience. A special mention goes to the entire AltForm Application Team, to John, my Tutor, and to all my colleagues, Guido, Palmiria, Andrea, Matteo, and Lorenzo. Thank you for sharing not only good moments, but also valuable experiences, discussions, and insights that I will carry with me throughout my future career.

TABLE OF CONTENTS

1 Introduction 1
1.1 Introduction to Additive Manufacturing 1
1.1.1 Process workflow 2
1.2 Additive manufacturing processes 3
1.2.1 Binder jetting 3
1.2.2 Directed energy deposition 4
1.2.3 Material extrusion 4
1.2.4 Material jetting 5
1.2.5 Powder bed fusion 6
1.2.6 Sheet lamination 6
1.2.7 Vat photopolymerization 7
1.3 Motivation 8
1.4 Roadmap 9
2 State of the art 10
2.1 Laser powder-based directed energy deposition process 10
2.1.1 DED process overview 10
2.1.2 LP-DED working principles 11
2.1.3 Process variables 13
2.1.4 Defects 15
2.1.5 Materials and applications 23
2.2 Refractory alloys 25
2.2.1 Overview 25
2.2.2 Niobium 25
2.2.3 C103 alloy 27
3 Methodology and materials 29
3.1 DED machine 29
3.2 Powder 30
3.3 Deposition strategy 32
3.4 Cutting 33
3.5 Mounting 35
3.6 Grinding and polishing 35
3.7 Micrography 36

3.8 Porosity analysis 37
3.9 Tensile test 37
4 Results and discussion 38
4.1 Single-tracks analysis 38
4.1.1 Parameters overview 38
4.1.2 Visual inspection 40
4.1.3 Micrography 41
4.2 Cube analysis 45
4.2.1 I manufacturing trial 45
4.2.2 II manufacturing trial 47
4.2.3 III manufacturing trial 52
4.3 Tensile test 57
4.4 Case-study component 58
5 Conclusions and future work 60
6 References 61

TABLE OF FIGURES

Figure 1.1. Process workflow schematization [12]. 2

Figure 1.2. Schematic of Binder Jetting process [9]. 3

Figure 1.3. Schematic of typical Directed Energy Deposition process [9]. 4

Figure 1.4. Schematic of Material Extrusion process [22]. 5

Figure 1.5. Schematic of Material Jetting process [24]. 5

Figure 1.6. Schematic of a) Laser Powder Bed Fusion technology [29] and b) Electron Beam Powder Bed Fusion technology [30]. 6

Figure 1.7. Schematic of Sheet Lamination process [33]. 7

Figure 1.8. Schematic of a typical Vat Photopolymerization process [36]. 8

Figure 2.1. AltForm's machine laser powder deposition head. 11

Figure 2.2. Schematic illustration of the Marangoni effect according to the Heiple-Roper theory. a) Melt pool geometry for a negative surface tension gradient; b) melt pool geometry for a positive surface tension gradient; c) transition in melt pool geometry associated with a change in the surface tension gradient from positive to negative. Rearranged from [50]. 13

Figure 2.3. Cross-sectional view schematic of a deposited track. a) Zero penetration (p = 0) or low penetration. b) optimal level of dilution. c) high penetration. Rearranged from [50]. 15

Figure 2.4. Model for residual stress formation during heating (left) and cooling (right) cycles [56]. 16

Figure 2.5. Different deposition pattern strategies [56]. 17

Figure 2.6. Taxonomy of keyholing and Lack-of-Fusion. a) Images i and iii are SEM of keyhole pores, image ii shows an XCT reconstruction. b) Image iv shows an XCT reconstruction of LoF pore, images v and vi are SEM of LoF pore. Rearranged from [77]. 18

Figure 2.7. Gas porosity [78]. 19

Figure 2.8. Optimal processing regions for different alloys, along with the unsuitable processing zones. Rearranged from [50]. 20

Figure 2.9. Example of a) delamination and b) solidification cracking [85]. 21

Figure 2.10. Economic importance as function of supply risk for different Critical Raw Materials, including niobium, as per the European Community. Rearranged from [126]. 26

Figure 2.11. Example of C103 aerospace components manufactured through AM. NASA MSFC a) Green Propulsion Thruster and b) Stand-off. Rearranged from [37]. 28

Figure 3.1. Gas shielding deposition head. 30

Figure 3.2. EDS analysis performed on virgin C103 powder sample from 6K Additive. . 30

Figure 3.3. Virgin C103 powder morphology SEM image, taken at 20.0 kV and 500x magnification. 31

Figure 3.4. Powder flow rate analysis. 32

Figure 3.5. Schematic of the deposition strategy. Boundary passes in orange and filling in blue. 32

Figure 3.6. a) complete case-study geometry; b) Region; c) Region 2; d) region 3. 33

Figure 3.7. Presi Mecatome T330 cutting machine. 34

Figure 3.8. Single-track scans cutting layout. 34

Figure 3.9. Cubes cutting layout. 35

Figure 3.10. Presi Mecapress 3 mounting machine. 35

Figure 3.11. Presi Mecatech 234 polishing machine. 36

Figure 3.12. Motic AE2000 MET microscope. 36

Figure 3.13. Cube surface subdivision for porosity analysis and points where images were taken for each region. 37

Figure 3.14. Instron 68FM-100 Dual Column Floor Model. 37

Figure 4.1. Deposited tracks A.1-A.27, where s indicates the deposition starting point. 39

Figure 4.2. Deposited tracks A.28-A.35, where s indicates the deposition starting point. 40

Figure 4.3. Tracks with visible pores. 40

Figure 4.4. Cross-sectional images tracks A.1-A.9. 43

Figure 4.5. Cross-sectional images tracks A.10-A.18. 43

Figure 4.6. Cross-sectional images tracks A.19-A.28. 44

Figure 4.7. Cross-sectional images tracks A.29-A.35. 44

Figure 4.8. Cube B.1. a) side view; b) top view. 45

Figure 4.9. Cube B.2. a) side view; b) top view. 46

Figure 4.10. Cube B.1 YZ plane micrograph. a) taken from region 1; b) taken from region 2; c) taken from region 3; d) taken from region 4; e) taken from region 5. 46

Figure 4.11. Cube C.1. a) side view; b) top view. 48

Figure 4.12. Cube C.2. a) side view; b) top view. 48

Figure 4.13. Cube C.1 YZ plane micrograph. a) taken from region 1; b) taken from region 2; c) taken from region 3; d) taken from region 4; e) taken from region 5. 48

Figure 4.14. Cube C.1 XY plane micrograph. a) taken from region 1; b) taken from region 2; c) taken from region 3; d) taken from region 4; e) taken from region 5. 49

Figure 4.15. Cube C.2 YZ plane micrograph. a) taken from region 1; b) taken from region 2; c) taken from region 3; d) taken from region 4; e) taken from region 5. 50

Figure 4.16. Cube C.2 XY plane micrograph. a) taken from region 1; b) taken from region 2; c) taken from region 3; d) taken from region 4; e) taken from region 5. 51

Figure 4.17. Cube D.1. a) side view; b) top view. 52

Figure 4.18. Cube D.2. a) side view; b) top view. 52

Figure 4.19. Cube D.1 YZ plane micrograph. a) taken from region 1; b) taken from region 2; c) taken from region 3; d) taken from region 4; e) taken from region 5. 53

Figure 4.20. Cube D.1 XY plane micrograph. a) taken from region 1; b) taken from region 2; c) taken from region 3; d) taken from region 4; e) taken from region 5. 54

Figure 4.21. Cube D.2 YZ plane micrograph. a) taken from region 1; b) taken from region 2; c) taken from region 3; d) taken from region 4; e) taken from region 5. 55

Figure 4.22. Cube D.2 XY plane micrograph. a) taken from region 1; b) taken from region 2; c) taken from region 3; d) taken from region 4; e) taken from region 5. 56

Figure 4.23. Specimen D.3 a) side view; b) top view. 57

Figure 4.24. Tensile test specimen after failure. 58

Figure 4.25. As-built case-study component. a) side view; b) top view. 59

LIST OF TABLES

Table 2.1. DED process classification. Rearranged from [41]. 10

Table 2.2. Summary table of the main materials used in Laser Powder Directed Energy Deposition and their applications. 24

Table 2.3. General C103 alloy chemical composition [135]. 27

Table 3.1. C103 powder chemical composition. 30

Table 3.2.C103 powder properties. 30

Table 3.3. Grinding and polishing parameters 36

Table 4.1. Scientific papers identified for process parameters development. 38

Table 4.2. Process parameters choice after literature review. 39

Table 4.3. Second set of process parameters choice. 40

Table 4.4. Tracks dimensions report. 41

Table 4.5. Parameter sets chosen for I manufacturing trial.. 42

Table 4.6. Parameters for the I manufacturing trial. 45

Table 4.7. Cube B.1 YZ plane porosity measurements. 47

Table 4.8. Parameters for the II manufacturing trial. 47

Table 4.9. Cube C.1 YZ plane porosity measurements. 49

Table 4.10. Cube C.1 XY plane porosity measurements. 49

Table 4.11. Cube C.2 YZ plane porosity measurements. 50

Table 4.12. Cube C.2 XY plane porosity measurements. 51

Table 4.13. Parameters for the III manufacturing trial. 52

Table 4.14. Cube D.1 YZ plane porosity measurements. 53

Table 4.15. Cube D.1 XY plane porosity measurements. 54

Table 4.16. Cube D.2 YZ plane porosity measurements. 55

Table 4.17. Cube D.2 XY plane porosity measurements. 56

Table 4.13. C103 specimen mechanical properties. 58

GLOSSARY

µCT	X-ray Micro-Computed Tomography
AFM	Atomic Force Microscopy
AM	Additive Manufacturing
ANOVA	Analysis of Variance
BCC	Body-Centered Cubic
BJT	Binder Jetting
BTF	Buy-to-Fly
CAD	Computer Aided Design
CLSM	Confocal Laser Scanning Microscopy
DED	Directed Energy Deposition
DfAM	Design for Additive Manufacturing
DoF	Degrees of Freedom
EB-PBF	Electron Beam Powder Bed Fusion
EDS	Energy-Dispersive X-ray Spectroscopy EDS
FCC	Face-Centered Cubic
GA	Gas-Atomize
GD	Generative Design
HIP	Hot Isostatic Pressing
I4.0	Industry 4.0
LCF	Low-Cycle Fatigue
LoF	Lack-of-Fusion
L-PBF	Laser Powder Bed Fusion
LP-DED	Laser Powder Directed Energy Deposition
LSP	Laser Shock Peening
MAF	Magnetic Field-Assisted Finishing
MEX	Material Extrusion
MJ	Material Jetting
NDT	Non-Destructive Testing
PBF	Powder Bed Fusion
PMZ	Partially Melted Zone
PREP	Plasma Rotating Electrode Process

SEM	Scanning Electron Microscope
SHL	Sheet Lamination
STL	Standard Tessellation Language
TO	Topological Optimization
UTS	Ultimate Tensile Strength
UV	Ultraviolet
VED	Volumetric Energy Density
VPP	Vat Photopolymerization
WAAM	Wire Arc Additive Manufacturing
WEAM	Wire Electron Beam Additive Manufacturing
W-EDM	Wire Electrical Discharge Machining
WLAM	Wire Laser Additive Manufacturing
XCT	X-ray Computed Tomography

1 INTRODUCTION

1.1 INTRODUCTION TO ADDITIVE MANUFACTURING

In 2011 the term “Industrie 4.0” (I 4.0) was used for the first time [1] , coined by a German initiative of the federal government with universities and private companies. The initiative was originally conceived as a strategic program aimed at developing advanced manufacturing systems to enhance industrial productivity and efficiency. The key objective of the program was to ensure sustainability, both economic and environmental [2], [3]. I 4.0 is based on nine enabling technologies (i) additive manufacturing, (ii) augmented reality, (iii) autonomous robot, (iv) big data, (v) cloud computing, (vi) cybersecurity, (vii) internet of things, (viii) simulations, and (ix) system integration [4], [5]. Among all the enabling technologies, additive manufacturing (AM) will be deeply discussed throughout the document.

Additive manufacturing is defined as “a process of joining materials to make parts from 3D model data, usually layer upon layer, as opposed to subtractive manufacturing and formative manufacturing methodologies” [6]. AM represents a disruptive shift in the landscape of industrial fabrication: rather than relying on material removal or plastic deformation, it creates components through the sequential deposition of material layer by layer, employing a thermal or bonding energy source to consolidate feedstock supplied in solid, powder, or liquid form [7]. The field is governed by the ISO/ASTM 52900:2021 [6], standard which provides a unified framework encompassing process classification, workflow definitions, and terminology across all AM categories. This technology is also commonly referred to as 3D-printing, rapid prototyping, freeform fabrication, or layer manufacturing, reflecting its evolution from a prototyping tool to a mature manufacturing technology [7].

The origins of AM can be traced to 9 March 1983, when Charles W. Hull successfully fabricated the first object using stereolithography, a photopolymerization-based process later protected under US Patent No. 4,575,330 (1984) [8]. Since then, AM technologies have undergone rapid development and have attracted considerable interest from both academia and industry due to their ability to fabricate geometrically complex components with a high degree of design freedom. One of the most distinctive characteristics of AM is the so-called complexity-for-free paradigm, whereby the production of intricate geometries, internal channels, lattice structures, porous architectures, and consolidated assemblies can be achieved without the significant manufacturing penalties typically associated with conventional processes [9]. This capability has fostered the development of Design for Additive Manufacturing (DfAM), a research field focused on exploiting the unique design opportunities offered by layer-wise manufacturing. Moreover, compared with conventional manufacturing routes, AM offers several potential advantages, including reduced material waste, improved buy-to-fly ratios for high-value alloys, lower tooling requirements, and a higher degree of process automation from design to fabrication [10]. These characteristics can contribute to shorter production lead times, enhanced resource efficiency, and the manufacture of integrated structures that would be difficult or impossible to produce using traditional manufacturing techniques [9].

1.1.1 Process workflow

The workflow of an Additive Manufacturing process, from geometry creation to final component realization, typically involves the following steps [11], [12]:

- 3D CAD model realization;
- Model conversion into STL file;
- Slicing;
- Layer-by-layer model manufacturing;
- Cleaning and post-processing.

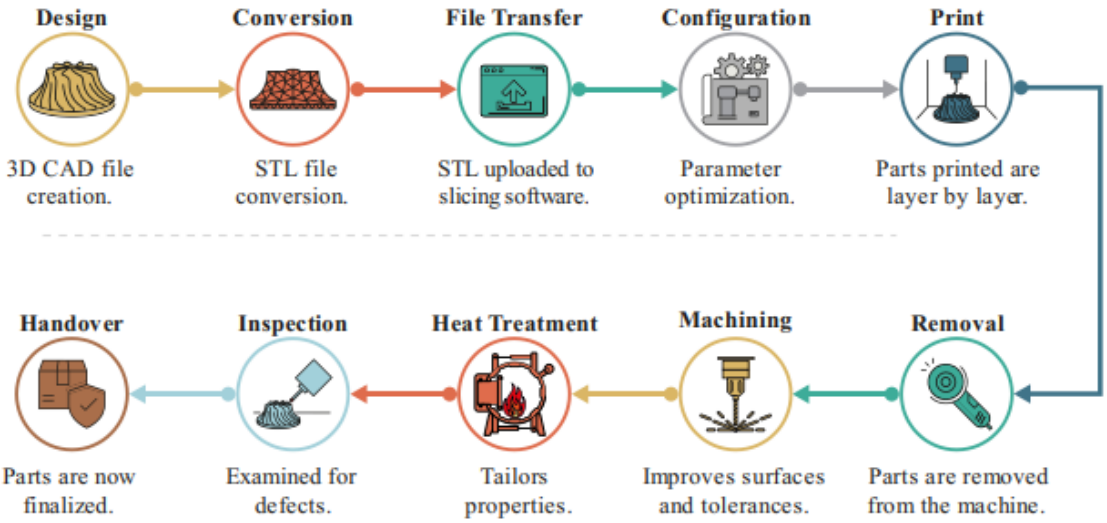


Figure 1.1. *Process workflow schematization [12].*

The design phase initiates the additive manufacturing workflow through the development of a three-dimensional digital model using Computer-Aided Design (CAD) software. This stage enables designers and engineers to create geometrically complex components that meet the functional and dimensional requirements of the intended application. During the design process, particular attention should be given to the selection of the build orientation, as it directly influences manufacturability, surface quality, support structure requirements, thermal history, residual stress accumulation, and, consequently, the final dimensional accuracy and mechanical performance of the component [11].

Once the digital model is finalized, it is exported as an STL file, which provides the link between the digital design environment and the additive manufacturing process. In this format, the component surface is approximated by a tessellated mesh of triangular facets, each defined by a three vertex coordinates and an outward-pointing vector normal to the facet plane. The accuracy of the geometric representation depends on the tessellation density, with finer meshes offering greater geometric fidelity at the expense of larger file sizes and increased computational requirements. Through this discretized representation, complex geometries can be converted into a standardized format suitable for subsequent processing steps [12].

The STL file is subsequently imported into slicing software, where the three-dimensional geometry is partitioned into a series of planar layers, typically of uniform thickness, perpendicular to the build direction. During this stage, the software generates the machine instructions required for fabrication, including the toolpath strategy, scanning or deposition speed, and the locations at which material deposition or laser exposure begins and ends. As

such, slicing constitutes the critical transition between the digital model and its layer-by-layer physical realization [13].

Following fabrication, the component undergoes post-processing operations intended to enhance its dimensional accuracy, surface integrity, and overall performance. These operations may include the removal of support structures, where required, together with surface finishing treatments and application-specific processes such as coating or metallic plating. For metallic components, post-processing commonly involves stress-relief heat treatments to reduce process-induced residual stress, followed by machining operations to achieve the dimensional tolerances and surface finish specified for the intended application [12], [13].

1.2 ADDITIVE MANUFACTURING PROCESSES

According to the ISO/ASTM 52900:2021 standard, additive manufacturing technologies are classified into seven process categories, each of which is described in the following sections.

1.2.1 Binder jetting

Binder jetting (BJT) is a powder-based additive manufacturing process in which a liquid bonding is selectively deposited onto a thin layer of powder to join particles according to the cross-sectional geometry of the component [9]. The process begins with the deposition of a uniform powder layer over the build platform using a recoating mechanism, after which an inkjet printhead selectively dispenses polymeric binder droplets onto the required region. Once a layer is completed, the build platform is lowered by one layer thickness, a new powder layer is spread, and the deposition sequence is repeated until the entire component is produced. BJT does not employ a high-energy source during manufacturing, consequently, the part is initially obtained as a low strength green body, which requires post-processing to achieve its final properties [14]. For metallic components, these operations typically include curing, depowdering, and sintering to remove the binder and densify the material, while additional infiltration or finishing treatments may be performed depending on the application [15]. Since the surrounding loose powder naturally supports overhanging features, dedicated support structures are generally unnecessary. Binder jetting is compatible with a broad range of feedstock materials, including metals, ceramics, polymers, foundry sands, and gypsum-based powders. This makes the technology suitable for applications ranging from visual prototypes and casting molds to functional metallic components, provided that appropriate post-processing is carried out [15].

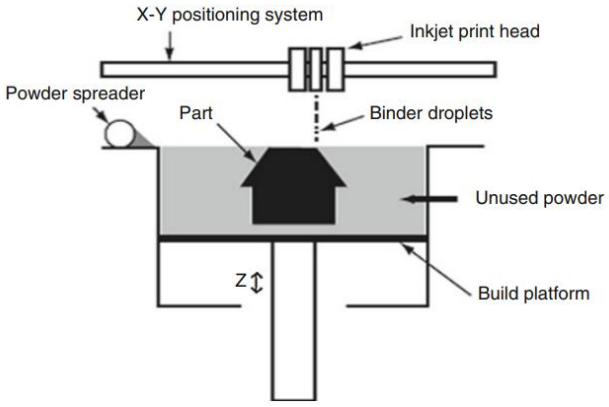


Figure 1.2. *Schematic of Binder Jetting process [9].*

1.2.2 Directed energy deposition

Directed Energy Deposition (DED) is an additive manufacturing process primarily employed for the fabrication of metallic components, in which a concentrated energy source and a continuous stream of feedstock material converge at a common focal point, typically within an inert shielding gas atmosphere. The feedstock, supplied either as powder or wire, is delivered through a deposition nozzle into the interaction zone, where it is melted by the focused energy source to generate a localized molten pool on the substrate or the previously deposited layer [16]. By controlling the relative motion between the deposition head and the workpiece, material is deposited layer by layer to produce near-net-shape metallic components. Depending on the process configuration, the deposition head is commonly mounted on a multi-axis motion system and incorporates a high-energy heat source, such as laser, plasma or electric arc, together with the feedstock delivery system, enabling the fabrication of complex three-dimensional geometries [17]. Although DED offers considerable flexibility in component fabrication, the as-built parts generally require post-processing operations, including machining and surface finishing, to achieve the dimensional tolerances and surface quality required for the intended application [16].

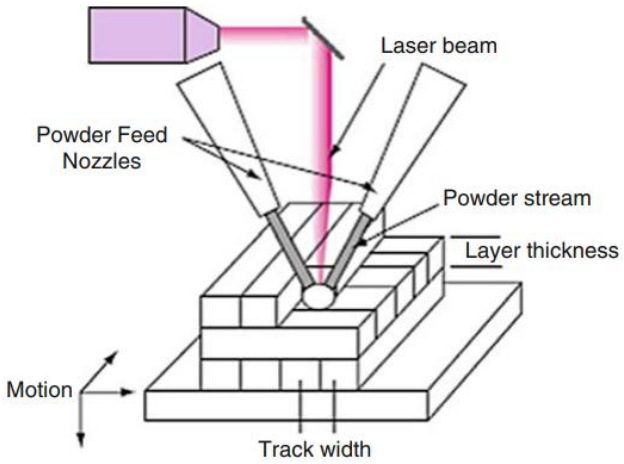


Figure 1.3. *Schematic of typical Directed Energy Deposition process [9].*

1.2.3 Material extrusion

Material extrusion (MEX) is an additive manufacturing process in which feedstock material is selectively dispensed through a nozzle and deposited onto a build platform or previously deposited layers by the relative motion between the extrusion system and the workpiece. During deposition, the material is extruded in a semi-solid or molten state and subsequently solidifies, allowing the component to be fabricated layer by layer according to the prescribed geometry [18]. Feedstock is commonly supplied as filament or pellets, although other forms such as rods may also be employed depending on the machine configuration [19]. Owing to its simple operating principle, low equipment cost, and broad material compatibility, Material Extrusion is among the most widely adopted additive manufacturing technologies. While thermoplastic polymers remain the predominant feedstock, the process has also been extended to fiber-reinforced composites, highly filled metal and ceramic feedstocks, and cementitious materials for large-scale construction applications [20]. Furthermore, the high deposition rates achievable with material extrusion have enabled the development of large-format additive manufacturing systems capable of producing components with build volumes exceeding 1 m^3 [21].

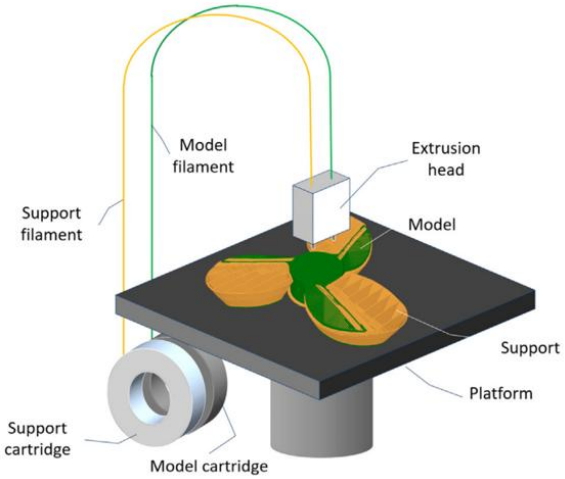


Figure 1.4. *Schematic of Material Extrusion process [22].*

1.2.4 Material jetting

In Material Jetting (MJ) process, droplets of build material are selectively deposited through one or more printheads to fabricate three-dimensional components in a layer-by-layer manner [23]. The process typically employs one or more deposition heads, a material delivery system, and a build platform that is progressively lowered after the completion of each layer. Feedstock materials are supplied in liquid or molten form from dedicated reservoirs and delivered to the deposition nozzles, enabling the processing of a range of materials, including photopolymers, waxes, and other jettable formulations. Once deposited, the material solidifies through a material-dependent mechanism, such as photopolymerization induced by ultraviolet (UV) radiation or thermal cooling, before the next layer is deposited [24]. Owing to the precise droplet placement and relatively high surface quality that can be achieved, MJ is particularly suitable for manufacturing components with fine geometric details and smooth surface finishes. However, because the deposited material generally exhibits limited mechanical stability before solidification, support structures are typically required to sustain overhanging features and complex geometries during fabrication. These supports are produced simultaneously using dedicated support material and are subsequently removed through mechanical, thermal, or chemical post-processing methods, depending on the material system employed [25].

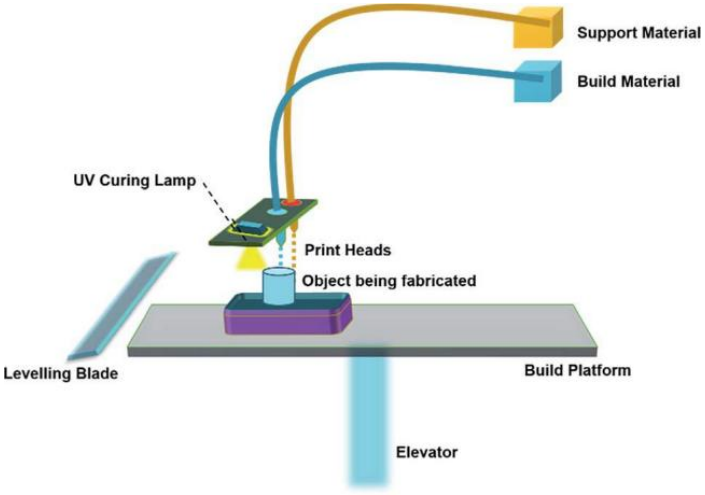


Figure 1.5. *Schematic of Material Jetting process [24].*

1.2.5 Powder bed fusion

Powder Bed Fusion (PBF) is an additive manufacturing process in which thermal energy is selectively applied to fuse regions of a powder bed, producing three-dimensional components [26]. A typical PBF system comprises a build platform, a powder reservoir, a recoating mechanism that distributes successive layers of powder across the build area, and an energy source that selectively scans the powder bed according to the cross-sectional geometry of the component. After each layer has been consolidated, the build platform is lowered by one layer thickness, a new powder layer is deposited, and the process is repeated until the part is completed. The feedstock consists of fine powders, with metallic alloys representing the predominant materials [27]. According to the energy source employed, PBF processes are primarily classified into Laser Powder Bed Fusion (L-PBF) and Electron Beam Powder Bed Fusion (EB-PBF). In L-PBF, a laser beam is directed onto the powder bed by galvanometric scanners and focusing optics, selectively melting the material under a controlled inert gas atmosphere. Conversely, EB-PBF employs a focused electron beam, controlled by electromagnetic lenses, and operates under high-vacuum conditions to ensure beam stability while simultaneously limiting the oxidation of highly reactive alloys [28]. Owing to their capability to manufacture near-net-shape components with complex geometries, high dimensional accuracy, and efficient material utilization, PBF technologies are widely adopted in high-value industries, including aerospace, biomedical, automotive, and energy applications [26].

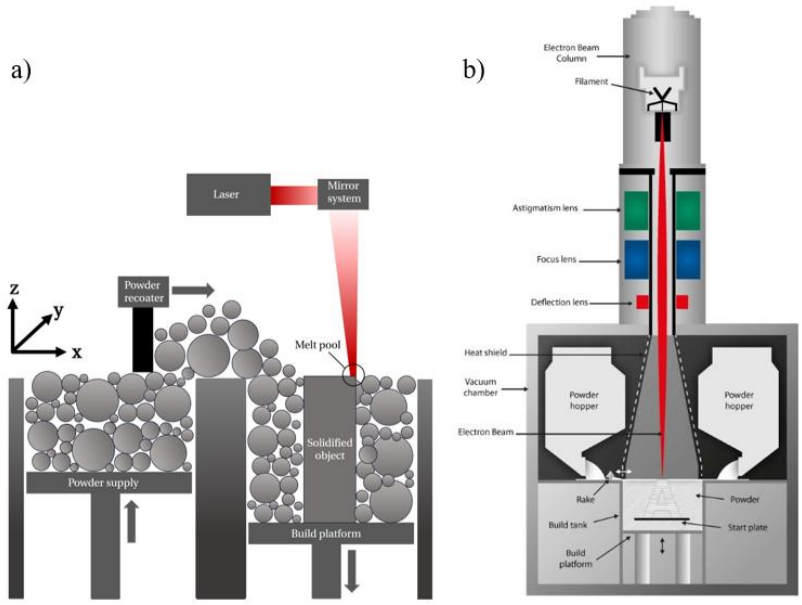


Figure 1.6. *Schematic of a) Laser Powder Bed Fusion technology [29] and b) Electron Beam Powder Bed Fusion technology [30].*

1.2.6 Sheet lamination

Sheet Lamination (SHL) is an additive manufacturing process in which three-dimensional components are produced by successively bonding sheets of material and cutting each layer to the required geometry [31]. A typical SHL system consists of a sheet feeding mechanism, a bonding unit, and a cutting device, such as a laser or a mechanical blade, which defines the cross-sectional profile of each layer. After a sheet has been positioned on the build platform, it is bonded to the previously deposited layer through the application of pressure, heat, adhesive, or other joining mechanisms, depending on the specific process configuration. The bonded sheet is subsequently cut to the desired geometry,

and the sequence is repeated until the component is completed. Unlike fusion-based additive manufacturing technologies, most Sheet Lamination processes join successive sheets without completely melting the feedstock material. Consequently, they involve lower thermal input than fusion-based processes, reducing the likelihood of thermally induced residual stresses and distortion [9]. Feedstock materials are supplied in sheet form and may include paper, polymer composites, ceramics, and metal-filled laminates, provided they can be rolled, bonded, and accurately cut during processing. Owing to its relatively simple processing route and high deposition rate, SHL is particularly suitable for the rapid fabrication of large components, visual prototypes, architectural models, and tooling, depending on the feedstock material employed. Nevertheless, the process may be affected by defects such as delamination, sheet deformation, and dimensional distortion, while certain material systems may require additional post-processing treatments, including thermal processing, to achieve the desired mechanical properties and dimensional accuracy [32].

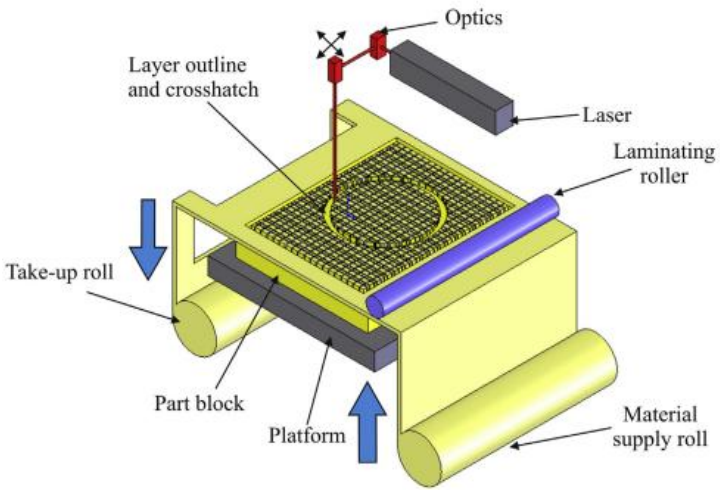


Figure 1.7. *Schematic of Sheet Lamination process [33].*

1.2.7 Vat photopolymerization

Vat Photopolymerization (VPP) is an additive manufacturing process in which liquid photopolymer resin contained within a vat is selectively cured by a light source to produce three-dimensional components. A typical VPP system consists of a resin vat, a movable build platform, and a light source, such as UV or visible light laser or a projected light engine, which selectively exposes the resin according to the cross-sectional geometry of the component. Upon exposure to the curing light, photoinitiators contained within the resin generate reactive species that initiate the polymerization of the monomers and oligomers, forming a cross-linked polymer network that irreversibly solidifies the material [34]. Once a layer has been cured, the build platform is repositioned to allow fresh liquid resin to cover the previously solidified layer, and the process is repeated until the component is completed. The feedstock consists of light-curable photopolymer resins specifically formulated to provide the rheological and optical properties required for controlled polymerization [35]. Owing to its excellent dimensional accuracy, fine feature resolution, and superior surface finish, VPP is widely employed for the fabrication of prototypes, dental and medical devices, investment casting patterns, and components requiring high geometric precision. However, the mechanical properties and long-term environmental stability of photopolymer resins are generally inferior to those of engineering thermoplastics and metallic materials, and post-curing treatments are commonly required to achieve the final material properties [34].

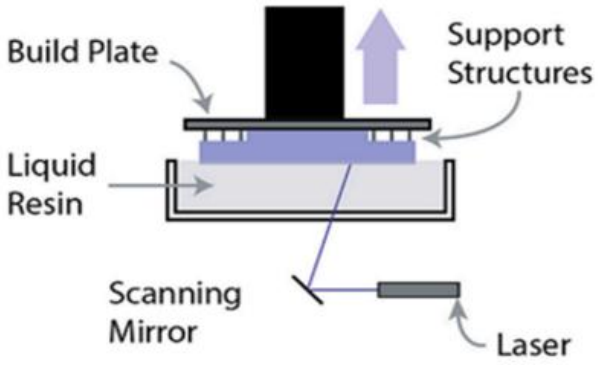


Figure 1.8. *Schematic of a typical Vat Photopolymerization process [36].*

1.3 MOTIVATION

Niobium alloys are widely employed in advanced engineering applications, particularly in the aerospace sector, owing to their excellent high-temperature mechanical properties, corrosion resistance, and thermal stability. Among them, the C103 alloy is extensively used for high-value propulsion components, such as rocket nozzle extensions and other high-temperature aerospace structures, which operate under severe thermomechanical conditions and therefore require exceptional structural integrity and reliability [37]. The large dimensions, complex geometries, and demanding service conditions of these components make their manufacture particularly challenging using conventional subtractive processes, often resulting in extensive machining operations, high production costs, and significant material waste. Consequently, the traditional manufacture of C103 aerospace components is frequently associated with very high buy-to-fly (BTF) ratios, which may vary between 20:1 and 50:1 depending on the component geometry and manufacturing route [38]. In this context, additive manufacturing represents a promising alternative by enabling near-net-shape fabrication, substantially improving material utilization and reducing production waste. Among the available additive manufacturing technologies, Laser Powder Directed Energy Deposition (LP-DED) is particularly well suited to the manufacture and repair of large metallic components owing to its high deposition rates, scalability, and capability to selectively deposit material only where required. Furthermore, unlike additive manufacturing processes based on a confined powder bed, LP-DED is not inherently limited by the dimensions of the build chamber, making it particularly attractive for the fabrication of large-scale aerospace structures such as those manufactured from C103 [27]. Furthermore, niobium and hafnium are included in the European Union's list of Critical Raw Materials because of their strategic importance and potential supply risk [39]. Therefore, improving the manufacturing efficiency of niobium-based components is of both technological and strategic interest. Consequently, this thesis aims to develop and optimize the LP-DED process parameters for the deposition of the C103 niobium alloy, contributing to the advancement of additive manufacturing technologies for refractory metallic materials.

1.4 ROADMAP

This thesis is organized into five chapters. Following the present introductory chapter, Chapter 2 provides a comprehensive review of the current state of the art. The first part of the chapter introduces Directed Energy Deposition technologies, with particular emphasis on Laser Powder Directed Energy Deposition, discussing its main process characteristics, relevant process parameters, typical defects, feedstock materials, and industrial applications. The second part focuses on refractory metals, with particular attention to niobium and its alloys, and provides a detailed overview of their properties, applications, and manufacturing challenges, with a specific focus on the C103 niobium alloy. Chapter 3 describes the experimental methodology adopted throughout the study, including the materials, equipment, and experimental procedures employed. Chapter 4, together with the rationale underlying the selection of the processing parameters, presents and discusses the experimental results, analyzing the influence of the investigated process parameters on the quality and characteristics of the deposited material. Finally, Chapter 5 summarizes the main findings of the research, highlights its principal contributions, discusses its limitations, and outlines potential directions for future work.

2 STATE OF THE ART

2.1 LASER POWDER-BASED DIRECTED ENERGY DEPOSITION PROCESS

2.1.1 DED process overview

According to the ISO/ASTM 52900 standard, Directed Energy Deposition is defined as an "additive manufacturing process in which focused thermal energy is used to fuse materials by melting as they are being deposited" [6]. Among metal additive manufacturing technologies, DED is characterized by the simultaneous delivery of both the energy source and the feedstock, allowing material to be deposited directly onto a substrate or onto previously solidified layers to produce near-net-shape components [40].

The process is derived from the concepts of welding and cladding technologies, in which a concentrated heat source generates a localized molten pool while the feedstock is continuously supplied to the deposition region [7]. Depending on the adopted system, thermal energy can be provided by a laser beam, an electron beam, an electric arc, or a plasma arc. At the same time, the feedstock, supplied either in powder or wire form, is delivered into the melt pool through dedicated feeding systems [41]. The interaction between the energy source, the incoming material, and the previously deposited layer produces localized melting, ensuring metallurgical bonding between successive layers. As the heat source moves along the programmed deposition path, the molten material rapidly solidifies, forming a continuous deposition bead. The repetition of this sequence enables the layer-by-layer fabrication of fully dense three-dimensional metallic components. Typical cooling rates during the DED process range from 10^3 to 10^5 °C/s, significantly affecting the resulting microstructure and mechanical properties of the deposited material [9].

Table 2.1. *DED process classification. Rearranged from [41].*

Feedstock	Feeding type	Thermal energy	Classification	Deposition mechanism	Ref
Powders	Co-axial and lateral off axis	Laser (CO2, Nd:YAG, Fiber)	LP-DED	Cladding	[7], [9], [40], [41], [42], [43], [44], [45]
Wire	Co-axial and lateral off axis	Laser	WLAM	Cladding and Welding	[7], [44], [45], [46]
	Co-axial and lateral off axis	Electric arc	WAAM	Welding (GMAW, GTAW, etc.)	[7], [9], [40], [43], [44], [45], [47], [48], [49]
	Co-axial and lateral off axis	Plasma Arc		Welding (PAW, PTAW)	[45], [48], [49], [50], [51]
	Co-axial and lateral off axis	Electron beam (Thermionic and Plasma)	EBAM	Welding	[7], [43], [44], [49], [52], [53], [54]

DED systems can be classified according to different criteria, the most common being the type of feedstock employed. As shown in Table 2.1, DED technologies are generally divided into powder-fed and wire-fed systems. Powder-fed processes are predominantly based on laser energy sources, whereas wire-fed systems can employ electric arcs, plasma arcs, lasers, or electron beams as the heat source [44]. Material can be delivered into the

molten pool using either coaxial or lateral feeding configurations, each offering different advantages in terms of accessibility, deposition flexibility, and process stability. Off-axis feeding systems are generally more sensitive to feed orientation and deposition conditions, an effect that becomes especially significant in Wire Laser Additive Manufacturing (WLAM) processes [45].

The choice of energy sources strongly influences process characteristics and manufacturing performance. Laser, arc, and electron beam-based DED systems exhibit energy densities on the order of 10^6, 10^4, and 10^8 W/mm^2, respectively. Furthermore, Laser Powder DED, Wire Arc Additive Manufacturing (WAAM), and Wire Laser Additive Manufacturing require shielding gases to prevent oxidation of the molten pool during deposition, whereas Wire Electron Beam Additive Manufacturing (WEAM) is performed under vacuum conditions [41]. From a manufacturing perspective, WAAM generally offers the lowest equipment investment cost among the main DED technologies. Conversely, although wire-fed processes provide significantly higher deposition rates and larger layer thicknesses than powder-fed systems, they generally exhibit lower dimensional accuracy and higher residual stresses in the fabricated components. On the other hand, components produced by laser powder-fed DED typically show surface roughness values approximately 20-30% higher than those obtained through WLAM during planar deposition [50].

2.1.2 LP-DED working principles

Laser Powder Directed Energy Deposition (LP-DED) systems employ a deposition head designed to simultaneously deliver the laser beam, metallic powder, and shielding gas to a common interaction zone, where melting and material consolidation occur. The deposition head represents the core component of the process, as it governs the thermal energy distribution, powder transport efficiency, and protection of the molten pool from atmospheric contamination [27]. The laser beam, typically generated by a high-power fiber laser and transmitted through an optical fiber, enters the deposition head and is collimated before passing through a focusing lens. The optical assembly is designed to minimize beam divergence while producing the desired focal spot diameter on the substrate. Depending on the optical configuration, the focal position can be adjusted to optimize the energy density according to the deposition strategy and the geometrical characteristics of the component [41].



***Figure 2.1**. AltForm's machine laser powder deposition head.*

Surrounding the optical path, the head incorporates a series of powder feeding channels connected to external powder feeders through flexible hoses. Metallic powder is pneumatically transported by a carrier gas, generally argon or nitrogen depending on material compatibility, and is directed towards the focal region through a specially designed nozzle. Modern LP-DED systems predominantly employ coaxial nozzles, in which multiple converging powder streams create a symmetrical powder cone around the laser beam. This configuration provides directional independence, allowing material deposition regardless of the scanning direction while improving powder utilization efficiency and process stability [44].

During deposition, the laser beam locally melts both the substrate and the incoming powder particles, generating a molten pool into which fresh material continuously enters. As the deposition head moves relative to the workpiece, rapid solidification of the melt pool produces a metallurgically bonded track. The interaction between laser power, focal position, powder mass flow rate, gas flow dynamics, and traverse speed determines the geometry of the deposited bead, dilution with the substrate, thermal history, and ultimately the microstructure and mechanical properties of the fabricated component.

Among the physical phenomena governing melt pool behavior during Directed Energy Deposition, Marangoni convection plays a fundamental role in determining melt pool stability and fluid flow. The Marangoni effect is a thermocapillary convection phenomenon generated by surface tension gradients along the free surface of the molten pool, which primarily arise from spatial temperature variations and, to a lesser extent, differences in chemical composition. These surface tension gradients induce fluid flow from regions of lower surface tension towards regions of higher surface tension, thereby influencing the shape, dimensions, and penetration of the melt pool. Consequently, Marangoni convection affects the heat and mass transfer within the molten material and may indirectly influence the formation of process-induced defects, such as lack-of-fusion porosity, gas entrapment, and compositional inhomogeneities [50].

The relationship between surface tension gradients and melt pool flow was first described by Heiple and Roper [55], who demonstrated that the sign of the surface tension gradient with respect to temperature governs the direction of fluid circulation within the melt pool. The intensity of this thermocapillary flow is commonly characterized by the dimensionless Marangoni number M_a, reported in Equation 2.1, which expresses the relative importance of surface tension-driven convection with respect to thermal diffusion.

$$M_a = \frac{d\gamma}{dT} \cdot \frac{dT}{dx} \cdot \frac{L^2}{\eta\alpha} \tag{2.1}$$

where γ is the surface tension [N/m], dT/dx is the temperature gradient [K/m], α is the thermal diffusivity [m^2/s], L is the characteristic length [m], and η is the viscosity of the melt pool [Pa·s].

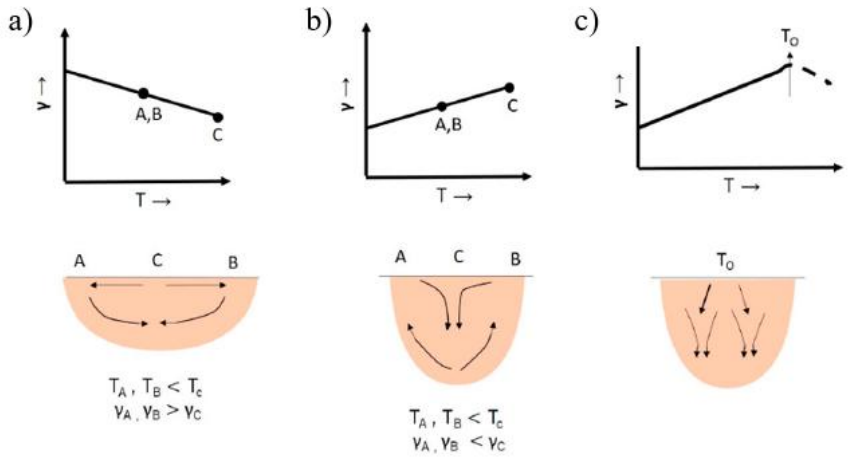


Figure 2.2. *Schematic illustration of the Marangoni effect according to the Heiple-Roper theory. a) Melt pool geometry for a negative surface tension gradient; b) melt pool geometry for a positive surface tension gradient; c) transition in melt pool geometry associated with a change in the surface tension gradient from positive to negative. Rearranged from [50].*

The influence of the surface tension gradient on melt pool morphology is schematically illustrated in Figure 2.2. When the surface tension decreases with increasing temperature, $d\gamma/dT < 0$, fluid flow is directed away from the hotter center of the melt pool towards the cooler periphery, promoting a wider and shallower melt pool associated with dominant surface flow Figure 2.2a. Conversely, when the surface tension increases with temperature $d\gamma/dT > 0$, the flow is redirected towards the center of the melt pool, producing deeper melt penetration and stronger bulk convection Figure 2.2b. In some alloy systems, the presence of surface-active elements may alter the sign of the surface tension gradient above a transition temperature T_o, resulting in a change in the dominant flow pattern, as schematically represented in Figure 2.2c. Therefore, the concentration of surface-active elements can significantly influence melt pool dynamics and, consequently, the final geometry and metallurgical quality of the deposited material [50].

2.1.3 Process variables

The fabrication of high-quality components by Directed Energy Deposition (DED) is a complex task owing to the large number of interacting process variables that govern the thermal history of the deposited material. These variables directly influence melt pool formation and solidification behavior, ultimately determining the microstructure, geometrical characteristics, and mechanical performance of the deposited material. In blown-powder DED systems, the process parameters can be broadly classified into three categories: (i) system-dependent parameters, (ii) feedstock-dependent parameters, and (iii) deposition process parameters [56]. Like fusion welding processes, the material response strongly depends on the intrinsic properties of the powder feedstock, including its chemical composition, melting temperature, thermal conductivity, laser reflectivity, specific heat capacity, melt viscosity, surface tension, and spectral emissivity [57].

Among the deposition process parameters, laser power, laser scanning speed (also referred to as traverse speed), and powder mass flow rate are generally regarded as the primary variables controlling the deposition process [9]. Other parameters, including hatch distance -the distance between two consecutive tracks considering the overlap between them-, laser beam diameter, layer thickness (z-step), and working distance, are typically maintained constant during parameter optimization following preliminary experimental

investigations, which commonly involve the deposition and characterization of single or overlapping tracks [58]. To facilitate process optimization, combinations of the primary process variables are often expressed through derived parameters such as the linear energy density LED [J/mm], volumetric energy density VED [J/mm^3], and powder density F [g/mm^2]:

$$LED = \frac{P}{v} \tag{2.2}$$

where P is the laser power [W] and v is the laser scan speed [mm/s],

$$VED = \frac{P}{t \cdot HD \cdot v} \tag{2.3}$$

where t is the layer thickness [mm] and HD is the hatching distance [mm],

$$F = \frac{G}{v \cdot d} \tag{2.4}$$

where G is the powder mass flow rate [g/s] and d is the laser beam diameter [mm].

These parameters provide a convenient framework for correlating process conditions with deposition continuity and bead geometry. Nevertheless, their predictive capability remains limited. For example, it has been demonstrated that identical energy density values may produce significantly different material densities during the deposition of Al-Mg alloys [59]. This observation indicates that energy density alone cannot be considered a robust descriptor of the process, as the final deposition quality is also strongly affected by material-dependent properties, such as laser absorptivity, thermal conductivity, melt pool surface tension, and powder feeding conditions [56].

Since the feedstock is delivered directly into the molten pool through the deposition nozzle, the powder mass flow rate determines the amount of material available for deposition. However, the effective material deposited per unit length also depends on the laser scanning speed, which simultaneously controls both the interaction time between the laser beam and the substrate, and the energy delivered to the deposited material. Consequently, the combination of powder mass flow rate and scanning speed determines the effective residence time of the laser per unit mass of injected powder [50]. Longer residence times generally increase both the energy transferred to the material and the amount of powder incorporated into the molten pool, resulting in larger deposited beads. Laser scanning speed also plays a fundamental role in controlling melt pool solidification behavior [60], thereby significantly affecting the resulting microstructure and mechanical properties of the deposited material. Not all the injected powder contributes to the final deposit. The fraction of powder that is successfully incorporated into the molten pool is commonly referred to as the powder catchment efficiency [61]. Besides the powder mass flow rate, this parameter is influenced by several factors, including melt pool temperature, surface tension, and powder stream characteristics such as particle dispersion [62]. These factors ultimately affect the geometry and dimensional accuracy of the deposited bead. It has been shown that increasing the laser power generally produces wider and deeper melt pools without significantly increasing the deposited layer height. This behavior was attributed to an increase in catchment efficiency resulting from the larger molten pool surface area, which allows a greater fraction of the injected powder to be captured while simultaneously distributes the deposited material over a wider melt pool [56].

In multilayer DED processes, dilution plays a fundamental role in ensuring adequate metallurgical bonding between successive layers while limiting excessive remelting of the substrate. During the fabrication of a component, repeated deposition results in progressive heat accumulation, modifying the thermal history of the process and consequently influencing the microstructure and final properties of the deposited material. The quality of the metallurgical bond between adjacent layers is commonly evaluated through the dilution D:

$$D = \frac{p}{h + p} \tag{2.5}$$

where p is the melt pool penetration depth [mm] and h is the height of the deposited material above the substrate [mm]. A large value of h generally results from a high powder mass flow rate or insufficient energy input, leading to low dilution and potentially causing lack-of-fusion defects between adjacent layers. Conversely, excessive penetration depth p is typically associated with high energy input or low powder feed rate, resulting in excessive dilution and, in extreme cases, keyhole formation [50]. Therefore, an optimum dilution level is required to simultaneously ensure adequate metallurgical bonding while avoiding excessive substrate remelting. Dilution values between approximately 10% and 30% are generally considered optimal for achieving sound metallurgical bonding in DED processes and are widely adopted throughout literature [63].

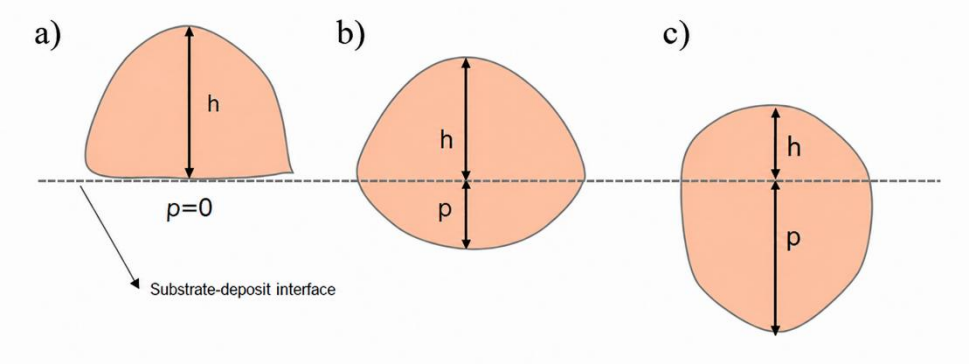


Figure 2.3. *Cross-sectional view schematic of a deposited track. a) Zero penetration (p = 0) or low penetration. b) optimal level of dilution. c) high penetration. Rearranged from [50].*

2.1.4 Defects

Directed Energy Deposition is an inherently non-equilibrium manufacturing process characterized by high heating and cooling rates, as well as steep thermal gradients. These thermal conditions strongly influence the solidification behavior of the deposited material and may lead to complex microstructural evolution, residual stress development, and geometrical distortion. Furthermore, if not properly controlled, they can promote the formation of process-induced defects, such as porosity and cracking, which may adversely affect the corrosion resistance and mechanical performance of the fabricated components, ultimately compromising their service life [56].

2.1.4.1 Residual stress

Residual stresses are an unavoidable consequence of virtually all thermomechanical manufacturing processes. In DED, their development is primarily associated with the layer-by-layer fabrication strategy, during which the material undergoes repeated cycles of

melting, remelting, and reheating as subsequent layers are deposited [64]. Furthermore, DED is an inherently non-equilibrium manufacturing process characterized by rapid cooling rates, typically ranging from 10^2 to 10^4 K/s [65], and steep thermal gradients on the order of 10^4-10^5 K/m [64]. These extreme thermal conditions promote complex microstructural evolution and phase transformations, while simultaneously generating heterogeneous thermal strains throughout the component. Therefore, significant residual stresses develop within the deposited material, exhibiting highly non-uniform spatial distributions and steep stress gradients that may reach values of approximately 10^2 MPa/mm [66]. Like conventional fusion welding, the evolution of residual stresses and the associated component distortion in DED are governed by the interaction between thermal expansion, constrained contraction, and repeated thermal cycling [12], as shown by Figure 2.4. Depending on the scale over which they act, residual stresses are commonly classified into three categories: macroscopic Type I, microscopic Type II, and atomic-scale Type III stresses [67].

Residual stress measurement remains a challenging task because these stresses cannot be measured directly and must instead be inferred from measurable physical quantities, such as component deformation, lattice spacing, or acoustic wave propagation. The available techniques are generally classified as either destructive or non-destructive. Destructive methods rely on the mechanical relaxation of residual stresses and include techniques such as hole drilling, serial sectioning, and ring-core drilling [64]. Conversely, non-destructive techniques estimate residual stresses through measurements of lattice spacing using diffraction methods, ultrasonic wave velocity, or Barkhausen noise, which is generated by ferromagnetic materials subjected to an external magnetic field [68]. Since each technique relies on specific assumptions regarding the material behavior and stress state, careful consideration must be given to their applicability to the component under investigation.

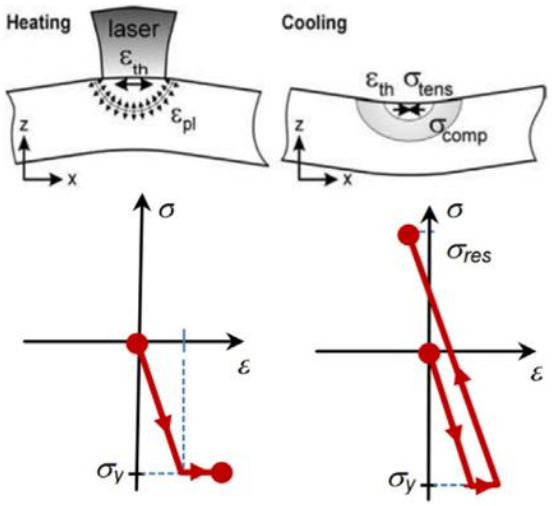


Figure 2.4. *Model for residual stress formation during heating (left) and cooling (right) cycles [56].*

Several approaches have been proposed to mitigate residual stress development during and after the DED process. One of the most widely adopted strategies is substrate, build chamber, or component preheating during deposition, which reduces thermal gradients and consequently lowers the magnitude of thermally induced stresses [27]. Corbin et al. [69] demonstrated that preheating the substrate to 400 °C reduced the distortion generated during deposition of the first layer by 27.4%. Furthermore, combining substrate preheating with build chamber heating resulted in reductions of residual stresses and distortion of up to

80.2% and 90.1%, respectively. Similarly, Vasinonta et al. [70] reported that uniform preheating of both the substrate and the deposited component significantly decrease residual stresses, achieving reductions of approximately 40% when both were heated to 400 °C. Although preheating substantially alleviates thermal stresses, it does not completely get rid of them, and additional post-processing treatments are often required. Residual stresses accumulation can also be reduced through appropriate optimization of the deposition strategy. Process parameters such as shorter scan lengths, checkerboard deposition strategies, spiral-in scanning patterns, increased scanning speeds, reduced layer thicknesses below the melt pool depth, and appropriate overlap between adjacent tracks through optimized hatch spacing were found to decrease both residual stresses and distortion [27]. For example, Woo et al. [71] investigated the influence of scan strategy on functionally graded materials manufactured by laser DED and reported that the residual stress range decreased from approximately 950 MPa using a 0° hatch rotation to 680 MPa with a 90° hatch rotation and was further reduced to approximately 430 MPa using an island scanning strategy.

Post-deposition heat treatment represents another effective approach for residual stress relief [9]. Compared with conventionally manufactured materials, additively manufactured components generally exhibit higher stress relaxation rates under identical thermal and mechanical loading conditions owing to differences in grain structure and crystallographic texture. However, heat treatment may also promote carbide precipitation, alter the stress-free lattice spacing and potentially introduce errors in residual stress measurements. Consequently, heat treatment schedules should be specifically tailored to the alloy being processed to maximize stress relief while avoiding undesirable microstructural changes [56].

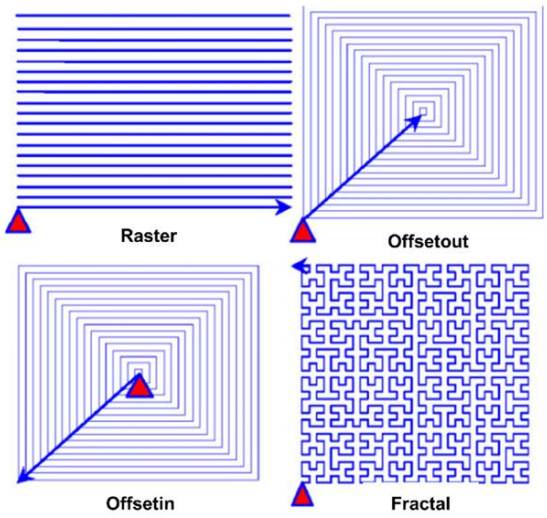


Figure 2.5. *Different deposition pattern strategies [56].*

Finally, post-processing surface treatments were also proved effective in modifying the residual stress state of DED components. Magnetic Field-Assisted Finishing (MAF), for example, was found to reduce tensile surface residual stresses from approximately 200 MPa to 70 MPa while simultaneously introducing beneficial compressive stresses at the component surface [72]. Likewise, Laser Shock Peening (LSP) was successfully applied to laser-DED Ti6Al4V components, modifying the surface residual stress state from approximately 100 MPa to 200 MPa in compression while increasing the surface microhardness from approximately 361 VHN to 420 VHN [73].

2.1.4.2 Porosity

Porosity is one of the most common defects encountered in Directed Energy Deposition and represents a major factor affecting the quality and structural integrity of additively manufactured components. Three principal mechanisms are generally responsible for pore formation [56]. The first is keyhole porosity [74], which occurs under excessive energy input when localized material vaporization produces an unstable keyhole cavity that subsequently collapses, entrapping gas within the solidifying melt pool. The second mechanism is lack-of-fusion (LoF) porosity, resulting from insufficient melt pool penetration into the substrate or the previously deposited layer because of inadequate energy input. This condition may arise when the linear heat input is insufficient, owing to a combination of low laser energy input, high scanning speed, excessive powder feed rate, or an unfavorable combination of these parameters, ultimately preventing complete melting of the deposited material [50].The third mechanism is gas porosity, which originates from gases initially contained within the powder feedstock, selective evaporation of volatile alloying elements during melting, or entrapment of the shielding gas inside the molten pool. From a geometrical perspective, porosity is commonly classified as either interlayer porosity, typically associated with lack of fusion, or intralayer porosity, which is generally distributed randomly throughout the deposited material [75].

The morphology of pores provides valuable information regarding their origin. Keyhole pores are generally relatively large and exhibit either a nearly circular cross-section combined with elongation along the build direction or a characteristic tapered shape that is wider near the surface than at its base, Figure 2.6a. LoF defects are generally larger, irregularly shaped, and have dimensions comparable to those of the melt pool Figure 2.6b, whereas gas pores are typically the smallest defects and exhibit an almost spherical morphology [76], Figure 2.7. Quantitative characterization of pore morphology is frequently performed using the sphericity factor, which facilitates the identification of the dominant porosity mechanism. In general, sphericity values below 0.6 are associated with LoF defects or partially melted powder particles, values exceeding 0.7 are characteristic of keyhole porosity, and values greater than 0.92 are indicative of gas porosity [77].

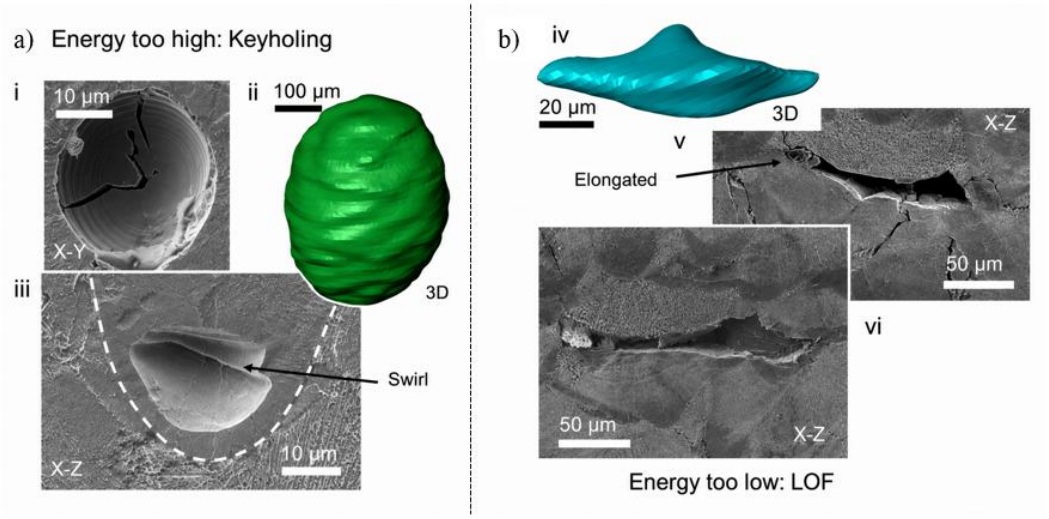


Figure 2.6. *Taxonomy of keyholing and Lack-of-Fusion. a) Images i and iii are SEM of keyhole pores, image ii shows an XCT reconstruction. b) Image iv shows an XCT reconstruction of LoF pore, images v and vi are SEM of LoF pore. Rearranged from [77].*

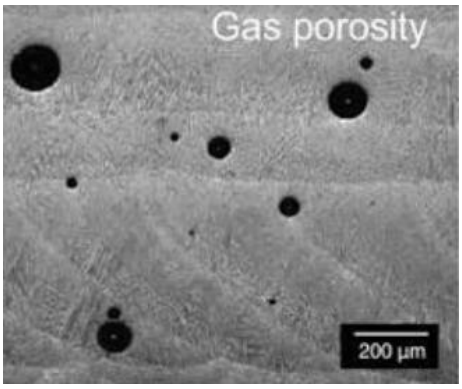


Figure 2.7. *Gas porosity [78].*

Since porosity acts as a stress concentrator and promotes crack initiation and propagation, minimizing its occurrence is essential for achieving high-quality DED components. Consequently, density measurement is among the first quality control procedures performed during process development, with a relative density exceeding 99.5% commonly considered as the target for optimized deposition conditions. In blown-powder DED, porosity is primarily influenced by the powder feed rate, the energy input determined by laser power, laser spot size, and scanning speed, as well as by the intrinsic porosity of the powder feedstock [79].

The presence of pores has a detrimental effect on both the mechanical performance and environmental durability of DED components, particularly reducing fatigue resistance, increasing mechanical anisotropy, and decreasing oxidation and corrosion resistance [80]. However, the severity of these effects strongly depends not only on the overall porosity level but also on the size, morphology, distribution, and location of the pores. Irregular or clustered defects generate higher stress concentrations than spherical pores and are therefore considered particularly detrimental to mechanical performance, especially when oriented perpendicular to the loading direction [79]. Furthermore, fatigue life is mainly affected by the presence of large pores, surface or near-surface defects, and, under low-cycle fatigue (LCF) conditions, by the pore morphology and the spacing between neighboring defects, with closely spaced pores promoting earlier crack initiation. Owing to the combined influence of these parameters, fatigue behavior often exhibits significant scatter, making lifetime prediction more uncertain [80].

Continuous improvements in process optimization and the implementation of in situ process monitoring have enabled the routine fabrication of DED components with relative densities exceeding 99%. Several experimental techniques are available for porosity characterization, including the Archimedes method, ultrasonic pulse-echo measurements, metallographic image analysis, X-ray micro-computed tomography (µCT). Among these, X-ray micro-computed tomography is particularly valuable because it enables three-dimensional characterization of pore size, morphology, and spatial distribution without damaging the component [27].

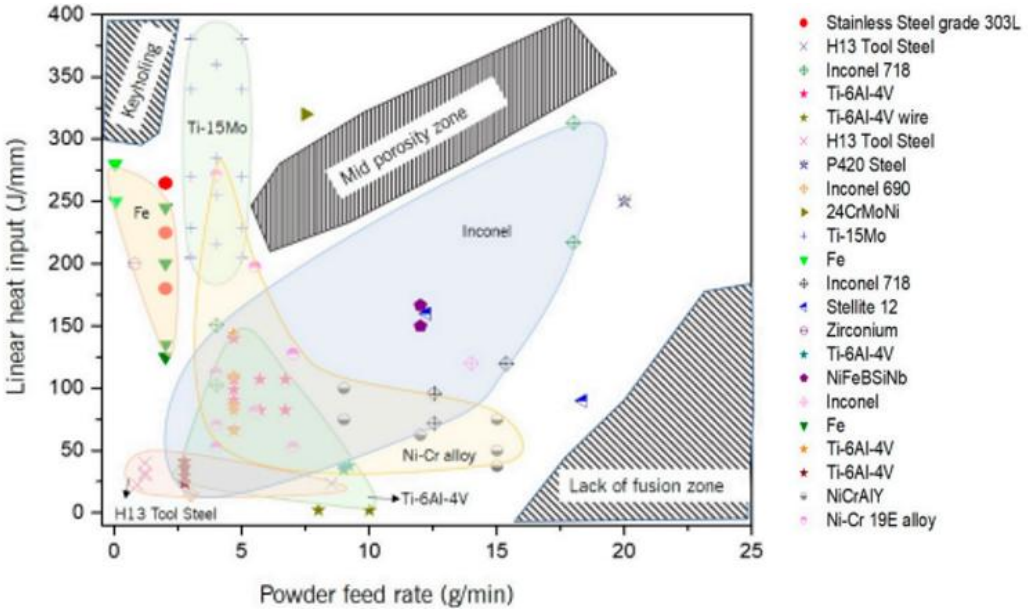


Figure 2.8. *Optimal processing regions for different alloys, along with the unsuitable processing zones. Rearranged from [50].*

The most effective strategy for minimizing porosity remains the optimization of the processing parameters. This generally involves adjusting laser power, scanning speed, hatch spacing, layer thickness, and powder feed rate, often using combined parameters such as linear energy density, volumetric energy density, and powder density to simplify process optimization [27]. Although appropriate parameter selection effectively minimizes interlayer LoF porosity, intralayer porosity is governed by more complex mechanisms and is therefore considerably more difficult to eliminate solely through parameter optimization [81]. Using analysis of variance (ANOVA), Liu et al. [82] demonstrated that laser power is the most influential processing parameter affecting the relative density of laser-DED AlSi10Mg components, contributing approximately 49% to the observed variation, whereas scanning speed accounts for approximately 34%.

In addition to process optimization, careful control of the powder feedstock is essential for reducing gas porosity. Since a fraction of the entrapped gas originates from the feedstock itself, powder production routes have a direct influence on the final defect population. Ahsan et al. [81] compared Ti6Al4V components manufactured using gas-atomized (GA) and plasma rotating electrode process (PREP) powders and reported consistently lower porosity levels in deposits produced from PREP powder.

Finally, post-processing treatments may further reduce the residual porosity. Hot Isostatic Pressing (HIP) is particularly effective in closing internal voids and improving mechanical properties [83]. Kobryn et al. [84] applied HIP to Ti6Al4V components manufactured by the DED process, achieving complete closure of lack-of-fusion defects and a significant improvement in ductility. Nevertheless, HIP is generally less effective in eliminating pores containing entrapped gas and therefore cannot always guarantee complete porosity removal [83].

2.1.4.3 Cracks and delamination

Delamination and cracking are among the most critical defects encountered in layer-wise additive manufacturing processes. In Directed Energy Deposition, their occurrence is further promoted by the significant thermal stresses generated during the repeated cycles of rapid heating and cooling that characterize the process. Delamination, defined as the separation

between two consecutive deposited layers or between the first deposited layers and the substrate, occurs when the interlayer residual stresses exceed the yield strength of the material [27]. This defect is generally associated with the incorporation of unmelted or partially melted powder particles, or with insufficient remelting of the underlying deposited layers, which compromises the metallurgical bonding between adjacent layers. Owing to the high stress concentrations that develop at the interface between the deposited material and the substrate, delamination is most frequently observed in this region [56].

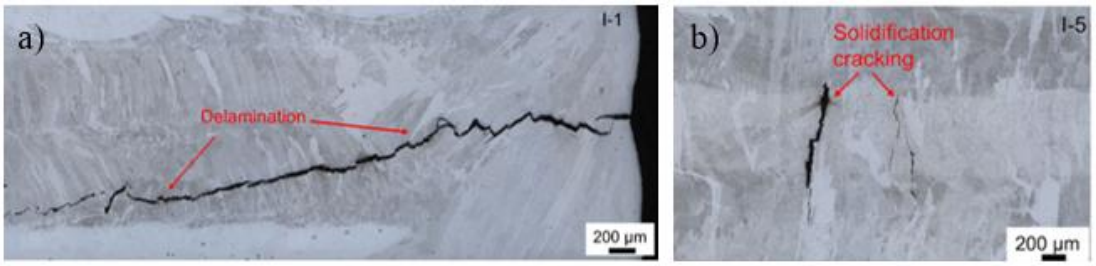


Figure 2.9. *Example of a) delamination and b) solidification cracking [85].*

The susceptibility to cracking strongly depends on the material being processed. In general, alloys that are prone to cracking during conventional fusion welding also exhibit a high tendency to crack during additive manufacturing processes. Three principal cracking mechanisms have been identified in additively manufactured components. The first is solidification cracking [193], also referred to as hot cracking, which develops along grain boundaries during the final stages of solidification. This defect originates from the higher thermal contraction of the recently deposited, hotter material relative to the underlying solidified layers or substrate, resulting in the development of high tensile stresses. The likelihood of solidification cracking increases when the applied energy input is excessive for the processed material and is strongly influenced by its solidification behavior [86], [87]. The second mechanism is liquation cracking, which occurs within the partially melted zone (PMZ). This type of cracking results from the melting of grain-boundary precipitates during rapid heating to temperatures below the liquidus, followed by the development of tensile stresses caused by solidification and thermal contraction during cooling [88].Consequently, alloys exhibiting a wide solidification temperature range, such as nickel-based superalloys, significant solidification shrinkage, such as Ti6Al4V, or high thermal contraction, such as aluminum alloys, are particularly susceptible to liquation cracking [27]. The third mechanism is ductility dip cracking, a solid-state intergranular cracking phenomenon that affects certain face-centered cubic (FCC) alloys within a specific elevated-temperature range [87]. Both delamination and cracking have a detrimental effect on the structural integrity of DED components, reducing their static and fatigue mechanical performance, decreasing corrosion resistance, and potentially leading to premature component failure.

The characterization of these defects can be performed using both destructive and non-destructive techniques, as well as through computational modelling. Destructive methods include metallographic cross-sectional analysis and fractographic investigation of opened cracks using scanning electron microscopy (SEM). Non-destructive testing (NDT) techniques include magnetic particle inspection, radiographic testing, X-ray micro-computed tomography, and ultrasonic testing, each providing different levels of sensitivity depending on the defect morphology and location [56].

Since post-processing techniques are generally unable to eliminate delamination and cracking, the most effective strategy is to prevent their formation during the deposition

process. This can be achieved through appropriate process optimization, including substrate and build chamber preheating, control of cooling rates, optimization of scan strategy, limitation of component aspect ratio and wall thickness, appropriate build orientation, and careful assessment of material compatibility when processing multi-material components [56].

2.1.4.4 Surface roughness

Surface roughness is one of the main limitations of DED technology. As a near-net-shape manufacturing process, DED generally requires complementary post-processing operations, such as machining or polishing, to achieve the dimensional tolerances and surface finish required for engineering applications. The relatively high surface roughness of DED components originates from several process-related phenomena, including the adhesion of partially melted powder particles caused by insufficient heat input or the use of coarse powder particles, as well as the balling phenomenon, which results from Rayleigh instability at high laser scanning speeds and causes the molten material to break into discrete droplets that accumulate at the edges of the melt pool [27], [87]. Additional contributors include the staircase effect, which is inherent to all layer-by-layer manufacturing processes and becomes particularly pronounced on inclined or curved surfaces, and the splashing of molten material during deposition. Consequently, the final surface quality is influenced by a combination of feedstock characteristics, component geometry, processing conditions, and post-processing operations [27], [89].

Not only surface roughness has a direct influence on the dimensional accuracy and geometrical tolerances of the fabricated components, but it can also significantly affect their mechanical performance, particularly under cyclic loading conditions. Especially, the presence of surface irregularities promotes stress concentration, facilitating crack initiation and consequently reducing fatigue resistance. It has been reported that a surface roughness of approximately 200 μm may reduce the fatigue strength of additively manufactured components by approximately 20-25%, depending on the specific manufacturing process [90].

Surface roughness can be quantitatively evaluated using a variety of contact and non-contact characterization techniques. Contact-based methods include stylus profilometry and atomic force microscopy (AFM), whereas non-contact techniques comprise confocal laser scanning microscopy (CLSM), white-light interferometry, and scanning electron microscopy (SEM), which also provides valuable qualitative information regarding surface morphology [56].

Several strategies have been proposed to reduce the surface roughness of DED components. Process optimization represents the first approach and generally involves increasing the heat input, provided that excessive energy input is avoided to prevent the development of high residual stress and non-uniform solidification. This objective can be achieved, for example, by combining relatively high laser power with low scanning speed. Additional improvements can be obtained by reducing the layer thickness and employing finer powder particles, both of which promote a more uniform deposition. Finally, post-processing operations, including machining, grinding, and chemical or electrochemical polishing, are commonly employed to further improve the surface finish of DED components [56]

2.1.5 Materials and applications

Laser Powder Directed Energy Deposition (LP-DED) is a highly versatile manufacturing technology capable of processing a broad range of metallic materials, including stainless steels, tool steels, titanium alloys, nickel-based superalloys, cobalt-based alloys, high-strength low-alloy steels and refractory metal alloys. The ability to process these materials enables the fabrication of components for demanding engineering applications requiring high mechanical performance, corrosion resistance, wear resistance, or elevated-temperature capability. Furthermore, the possibility of continuously varying the composition of the deposited material allows the production of Functionally Graded Materials (FGMs), in which local compositional variations are exploited to tailor the properties of different regions of a component according to service requirements [91].

Owing to this material flexibility, LP-DED has found applications across numerous industrial sectors. In the aerospace industry, it has been successfully employed to manufacture large and complex components, including titanium wing spars for the Comac C919 aircraft, turbine housings, helicopter engine combustion chambers, and gas turbine mixing nozzles, demonstrating its suitability for producing high-value structural components while reducing material waste compared with conventional manufacturing processes [92]. The technology has also been adopted for tooling applications, where the long lead times associated with conventional manufacturing have motivated the development of LP-DED solutions capable of significantly reducing production time [93]. In the biomedical field, Laser Powder DED has enabled the fabrication of patient-specific Ti6Al4V scaffolds for bone tissue engineering, exploiting the capability of additive manufacturing to produce customized geometries while mitigating the mismatch between the mechanical properties of metallic implants and natural bone [94]. Similarly, the automotive sector has benefited from Laser Powder Directed Energy Deposition through the production of components such as driveshaft spiders and suspension mounting brackets, achieving reductions of approximately 50% in manufacturing time together with material savings exceeding 90% compared with conventional manufacturing routes [92].

Beyond the production of new components, repair and remanufacturing represent one of the most mature and economically attractive applications of LP-DED. While damaged components are often replaced, repair becomes the preferred solution when dealing with high-value parts manufactured from expensive materials or characterized by complex geometries, where replacement involves substantial production costs [95]. In these cases, restoring the damaged region rather than replacing the entire component can lead to considerable economic benefits. Among the available repair technologies, LP-DED has become one of the most widely adopted processes owing to its relatively low heat input, limited distortion and residual deformation, high dimensional accuracy, and ability to produce sound metallurgical bonding while preserving the mechanical performance of the repaired component. These characteristics make Laser Powder DED particularly suitable for localized material restoration while minimizing the thermal damage typically associated with conventional repair techniques [96], [97].

The aerospace sector represents the most significant application of LP-DED repair technology because it extensively employs high-performance materials such as Ti6Al4V and nickel-based superalloys, whose high manufacturing cost makes component replacement economically unattractive [98]. The process has been successfully applied to the repair of turbine blades, blisks, and engine casings, while certification by Rolls-Royce Deutschland for fifteen different repair procedures further demonstrates the industrial maturity of the

technology [99]. Besides reducing maintenance costs, repairing aerospace components by LP-DED also provides environmental benefits by significantly reducing material consumption and waste generation during maintenance operations [96], [100].

The effectiveness of Laser Powder Directed Energy Deposition repair has also been demonstrated in several other industrial sectors. In tooling applications, the process has been successfully employed to restore dies and molds affected by wear or thermal cracking despite the limited weldability of many tool steels [101]. Automotive applications include the repair of grey cast iron engine components and crankshaft pulley hubs using stainless steel and cobalt-based alloys, respectively [102]. Similar advantages have been reported in the marine industry, where LP-DED has been used for the repair of large propellers and HSLA-100 steel structures for naval applications [103], as well as in the railway sector for the refurbishment of rails and railway wheels using wear-resistant and stainless steel alloys [104].

Table 2.2. *Summary table of the main materials used in Laser Powder Directed Energy Deposition and their applications.*

Material family	Representative alloys	Typical applications	References
Stainless steels	316L, 304L, 410, 420,17-4PH, 15-5PH, AM355	Repair, tooling, chemical industry	[50], [105], [106]
Tool steels	H13, AISI M2, A2, D2, Vanadis 4, CMP 9V, CPM 10	Dies, molds, hot-working tools	[50], [107], [108], [109], [110]
Nickel-based superalloys	Inconel 625, Inconel 718, Inconel 939, Hastelloy X, René 41	Aerospace, gas turbines	[27], [50], [100], [111], [112], [113], [114]
Titanium alloys	Ti6Al4V, Ti5553, Ti-6Al-2Sn-4Zr-2Mo	Aerospace, biomedical	[27], [50], [73], [84], [94], [112], [115]
Aluminum alloys	AlSi10Mg, Al6061, Al7075, Al5083	Lightweight structures	[27], [82]
Cobalt alloys	CoCrMo, Stellite 6, Stellite 12	Biomedical implants, wear-resistant coatings	[27], [50], [116]
Copper alloys	CuCrZr, GRCop-42, pure Cu	Heat exchangers, rocket combustion chambers	[9], [27]
Refractory metals and alloys	Nb alloys, C103; Ta, W, Mo alloys	Rocket nozzles, nuclear, high-temperature components	[27], [37], [38], [117], [118], [119], [120], [121]
High-Entropy Alloys (HEA's)	CoCrFeMnNi, AlCoCrFeNi, CrMnFeCoNi	Advanced structural materials	[27], [111]
Intermetallics	NiTi, TiAl	Biomedical devices, aerospace	[50]
Metal Matrix Composites	TiC/Ti64, WC/Ni, SiC/Al	Wear-resistant components	[50]
Functionally Graded Materials (FGA's)	Ti–Ni, Ti–Al, Ti–Steel, Inconel–Steel	Thermal barriers, transition joints	[50], [122]

2.2 REFRACTORY ALLOYS

2.2.1 Overview

Refractory metals are a class of metallic materials that has attracted increasing interest in additive manufacturing owing to their exceptional high-temperature performance. The most widely used refractory metals for structural applications include niobium (Nb), molybdenum (Mo), tantalum (Ta) and tungsten (W) [123]. Their extremely high melting temperatures and ability to retain mechanical strength under severe thermal conditions make them attractive for demanding aerospace and energy applications, where components must operate in extreme environments [124].

Despite these advantages, the widespread use of refractory metals remains limited by their poor oxidation resistance at elevated temperatures and limited fabricability, which complicate conventional manufacturing and processing [37]. Consequently, the selection of a refractory metal requires balancing thermomechanical performance, manufacturability and application requirements.

Niobium and tantalum have received the greatest industrial attention; however, niobium is generally preferred for structural applications because its significantly lower density enables the production of lightweight components while maintaining excellent high-temperature performance [121]. As a result, niobium and its alloys have become key materials for high-temperature engineering applications and are the focus of the following sections.

2.2.2 Niobium

Niobium was first discovered in 1801 by the English chemist Charles Hatchett during the analysis of an ore sent from Massachusetts to England [125], [126]. Industrial production began in the 1930s following the development of separation methods for niobium and tantalum, enabling the large-scale exploitation of niobium-bearing ores [126].

Niobium does not occur in its native metallic state in the Earth's crust and is generally associated with tantalum in naturally occurring minerals. Its principal mineral source is columbite, (Fe, Mn)Nb_2O_6-(Fe, Mn) Ta_2O_6. The abundance of niobium in the Earth's crust ranges from approximately 8 to 20 ppm [125], [126]. Brazil accounts for about 60% of global production, followed by Canada, Nigeria and the Democratic Republic of the Congo [125]. The discovery of extensive deposits in Brazil and Canada, together with the development of new industrial technologies and applications, has significantly increased niobium production since the second half of the twentieth century. Today, niobium concentrates are produced in approximately ten countries worldwide [126]. Owing to its strategic importance and the concentration of its global supply, niobium has recently been classified by the European Commission as a Critical Raw Material because of its high economic importance and the associated risk of supply disruption [39], see Figure 2.10.

Niobium is a shiny, silvery-grey metal with a body-centered cubic (BCC) crystal structure. In its high-purity state, it is comparatively soft and highly ductile, whereas impurities significantly increase its hardness [125]. Among refractory metals, niobium possesses the lowest density, around 8.4 g/cm^3, while maintaining a high melting temperature of 2468 °C, making it particularly attractive for lightweight high-temperature structural applications. It also exhibits the highest low-temperature ductility, a low ductile-to-brittle transition temperature and a high solubility for interstitial elements, resulting in reduced sensitivity of its ductile properties to interstitial content [127]. Chemically, niobium

exhibits excellent corrosion resistance and remains stable in many aggressive environments. It is resistant to hydrochloric, sulfuric, nitric and phosphoric acids, as well as to numerous inorganic and organic compounds, whereas it is attacked by concentrated hydrofluoric acid and HF/HNO_3 mixtures while remaining resistant to fused alkalis [125]. Nevertheless, owing to the high reactivity of refractory metals, the relationship between oxide precipitation and the resulting mechanical properties is still only partially understood. These oxidation-related phenomena remain one of the principal factors limiting the use of niobium-based alloys under extreme service conditions [128].

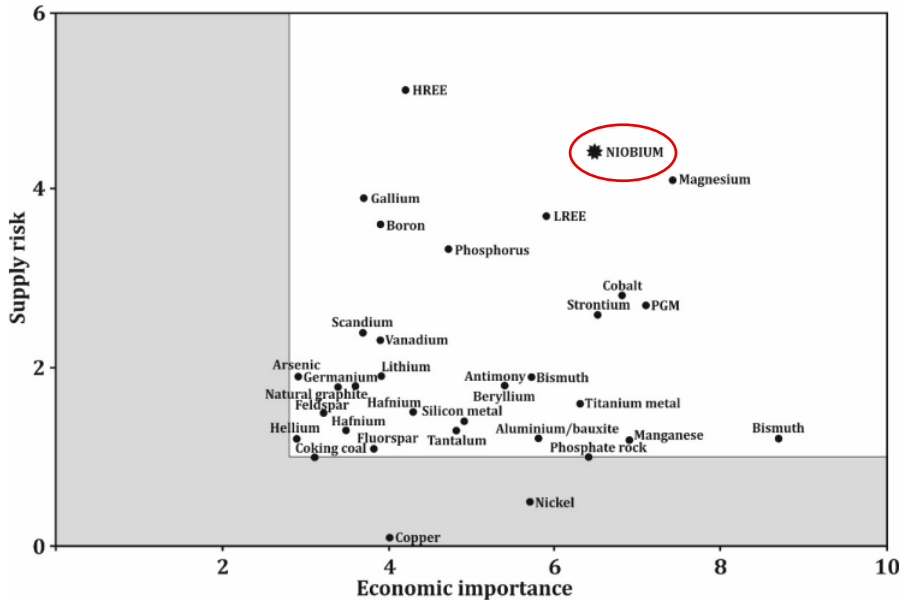


Figure 2.10. *Economic importance as function of supply risk for different Critical Raw Materials, including niobium, as per the European Community. Rearranged from [126].*

The combination of excellent thermophysical and mechanical properties has led to the widespread use of niobium in numerous engineering applications. It is extensively employed as an alloying element and grain refiner in high-strength low-alloy and stainless steels, where it improves tensile strength, hot ductility and resistance to thermal shock. Consequently, niobium-containing steels are widely used for oil and gas pipelines, structural components, shipbuilding, railway tracks, heavy vehicles and architectural applications [129]. Niobium and its compounds are also used in the electronics industry for the manufacture of ceramic capacitors, permanent magnets, optical materials, screens, lenses and chemical processing equipment. In addition, niobium and several of its alloys exhibit superconducting properties, making them suitable for high-powered magnets. Niobium carbide, together with the carbides of tantalum, titanium, tungsten and vanadium, is widely used in cutting tools because of its high hardness [125]. Owing to its high melting temperature and favorable strength-to-weight ratio, niobium is also employed in aerospace applications, including rocket propulsion systems, jet engine turbines and nuclear reactors [126]. More recently, niobium has gained increasing importance in renewable energy technologies, where niobium-containing steels are employed in wind turbine towers and blades, photovoltaic systems and lithium-ion batteries [130]. Its use has also expanded to solar cells, electric vehicles and charging infrastructure [131].

2.2.3 C103 alloy

Among niobium-based refractory alloys, C103 has long been regarded as one of the most promising materials for high-temperature structural applications. The increasing demand for propulsion systems capable of operating beyond the temperature limit of conventional nickel-based superalloys has renewed interest in refractory alloys, particularly for aerospace applications where operating temperatures above 1200 °C are required to improve engine efficiency [132]. Although refractory metals generally suffer from poor oxidation resistance and limited formability, recent advances in thermal barrier coatings and additive manufacturing have created new opportunities for their implementation in extreme operating environments [133].

C103 was one of the first refractory alloys successfully adopted by the aerospace industry. Owing to its ability to retain mechanical strength at elevated temperatures, it was employed in the nozzle extension of the Apollo Lunar Module, demonstrating the potential of niobium-based alloys for spacecraft propulsion systems[134]. The alloy has a melting temperature of approximately 2350 ± 50 °C [135] and a nominal composition depicted in Table 2.3, where the weight percentage has to be intended as maximum percentage unless otherwise specified.

Table 2.3. *General C103 alloy chemical composition [135].*

Element	Niobium (Nb)	Hafnium (Hf)	Titanium (Ti)	Zirconium (Zr)	Tungsten (W)	Tantalum (Ta)	Oxygen (O)	Carbon (C)	Nitrogen (N)
%wt	Balance	9-11	0.7-1.3	0.700	0.500	0.500	0.025	0.015	0.010

The excellent high-temperature performance of C103 originates from the synergistic action of its alloying elements. Hafnium is the primary strengthening element, providing significant solid-solution strengthening through its large atomic size mismatch with niobium and contributing to high-temperature stability by forming thermodynamically stable oxides. Titanium mainly improves room-temperature ductility and low-temperature strength while providing additional solid-solution strengthening. Because both elements are completely soluble in the niobium body-centered cubic matrix, C103 retains a single-phase BCC microstructure throughout its service temperature range without forming equilibrium intermetallic compounds [128], [136].

This alloy design provides an attractive combination of mechanical properties. Compared with commercially pure niobium and simpler Nb-1Zr alloys, C103 exhibits substantially improved high-temperature strength and creep resistance while maintaining approximately 20% elongation at room temperature and a ductile-to-brittle transition temperature close to -150°C [136]. The presence of hafnium also delays creep deformation at temperatures above 1000 °C by reducing diffusion-controlled deformation mechanisms, allowing the alloy to retain its structural stability up to temperatures approaching its melting point. Since no phase transformations occur during heating, the alloy remains microstructurally stable throughout service, while hafnium oxide precipitates formed during oxidation can also contribute to limiting grain growth [137].

Besides improving the mechanical properties, the alloying additions also influence the oxidation behavior of C103. Pure niobium forms a Nb_2O_5 surface scale that is susceptible to spallation, whereas the presence of hafnium and titanium promotes the formation of more stable HfO_2 and TiO_2 oxides, reducing the oxidation rate compared with unalloyed niobium.

Nevertheless, oxidation remains one of the major limitations of niobium alloys at elevated temperatures, and C103 components are commonly protected using silicide-based coatings for long-term service in oxidizing environments. Silicide-based coatings generally consist of intermetallic compounds formed between silicon and a refractory or transition metal and can be broadly represented by the general formula M_xSi_y, where M may include elements such as Mo, W, Nb, Cr, or Ti. Their use for protecting niobium alloys at elevated temperatures is primarily associated with the ability of the silicon-containing phases to promote the formation of a continuous and adherent SiO_2-rich oxide scale upon exposure to oxidizing environments. This silica-based layer acts as a diffusion barrier, limiting the transport of oxygen towards the underlying C103 substrate and thereby reducing the oxidation rate. Consequently, silicide-based coatings can significantly improve the oxidation resistance and high-temperature durability of C103 components operating in environments where the unprotected alloy would otherwise undergo rapid oxidation [128], [138].

Despite its outstanding high-temperature capabilities, the widespread adoption of C103 has historically been limited by manufacturing considerations rather than by its intrinsic material performance. Conventional production routes, including casting, forging and extensive machining, require long production lead times and are associated with very high buy-to-fly ratios, typically between 20:1 and 50:1, resulting in elevated production costs and substantial material waste [37]. Consequently, the industrial use of C103 progressively declined despite its excellent thermomechanical properties. The recent development of additive manufacturing has renewed interest in C103 by addressing many of the limitations associated with conventional processing. Near-net-shape fabrication significantly reduces material waste, minimizes machining requirements and enables the production of geometrically complex components. Moreover, recent studies have demonstrated the good printability of C103 (see Table 2.2) using additive manufacturing technologies, highlighting its potential for the fabrication of next-generation aerospace propulsion systems [139].

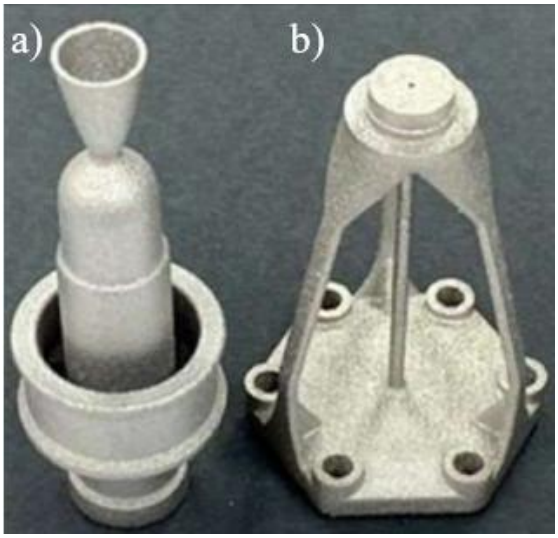


Figure 2.11. *Example of C103 aerospace components manufactured through AM. NASA MSFC a) Green Propulsion Thruster and b) Stand-off. Rearranged from [37].*

3 METHODOLOGY AND MATERIALS

The experimental campaign was structured into four stages: (i) single-track analysis, involving the fabrication of 35 single scan tracks; (ii) cube analysis, based on the production of six samples; (iii) fabrication of one tensile test specimen; and (iv) manufacturing of a case study component developed in response to a third-party request.

Different process parameters were investigated at each stage. During the single-track analysis, the input variables were laser power [W], laser scanning speed [mm/min] and powder feeder rotational speed [rpm]. For the cube analysis, the layer thickness [mm] was evaluated, while the process parameters identified in the previous stage were kept constant.

At the end of each experimental stage, the optimal process parameters were selected and adopted for the subsequent step. Following the cube analysis, a porosity assessment was carried out to verify that the deposited material satisfied the porosity requirements specified by the third party. Once the porosity criteria were met, the tensile test specimen was manufactured and mechanically characterized. After successful validation of the tensile properties, the final case study component was produced.

3.1 DED MACHINE

All samples were manufactured using AltForm's Cartesian robot machine, a large-scale Laser Powder Directed Energy Deposition system with a building volume of 6x4x1.5 m^3. The deposition head mounted on the Cartesian robot provides a working envelope of 4 m along the X-axis, 1 m along the Y-axis and 1 m along the Z-axis. In addition, the system is equipped with a roto-tilt table, allowing a total of 11 degrees of freedom (DoF): three associated with the machine portal, four with the deposition head, two with the roto-tilt table and two with the galvanometric scan head.

The laser system consists of a 3 kW laser source whose beam is transmitted to the deposition zone through an optical fiber and a set of optical lenses and galvanometric mirrors, ending in a 2 mm laser spot size. The deposition head, manufactured from a copper alloy, features a coaxial configuration in which four powder nozzles are symmetrically arranged around the laser beam. This design ensures that the powder stream converges at the laser focal point during deposition. To prevent contamination of the optical components by metallic powder, a protective screening lens is installed at the end of the laser head.

The entire laser-deposition head assembly is enclosed within a COAXshield gas shielding nozzle developed by Fraunhofer. This system creates a localized inert atmosphere spanning 13 cm^3 around the melt pool, enabling the processing of highly reactive materials without requiring complete inertization of the building chamber. Throughout this work, argon was employed as the shielding gas. To maintain stable operating conditions, the deposition head is cooled by a chiller using a water-glycol heat-exchange circuit.

Metal powder is delivered to the deposition head through antistatic polymer tubes connected to a powder feeder comprising a rotating dosing disk and an inert storage tank. The powder feed rate is controlled by adjusting the rotational speed of the dosing disk.

Two collection tanks, located beneath both the deposition platform and the roto-tilt table, recover the unfused powder generated during the process. After the collection using a dedicated vacuum system, the recovered powder can be reused after appropriate mixing with

virgin powder. Finally, process fumes, shielding gas and fine powder particles generated during deposition are removed by a fixed extraction system installed above the cell.

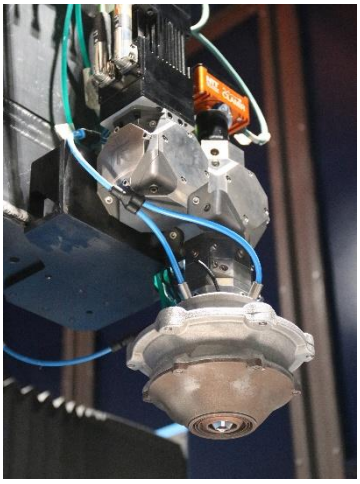


Figure 3.1. *Gas shielding deposition head.*

3.2 POWDER

The feedstock material employed in this study was a C103 niobium alloy powder supplied by 6K Additive and manufactured using the proprietary UniMelt® process, an industrial-scale microwave plasma technology. During the process, the metallic feedstock is introduced into a controlled plasma environment, where it is rapidly melted and spheroidized to produce spherical metal powder. The powder exhibited a particle size range of 20-63 µm. Prior to deposition, its chemical composition was characterized by energy-dispersive X-ray spectroscopy (EDS), Figure 3.2 to verify its elemental composition. The measured composition is reported in Table 3.1. The powder properties reported in Table 3.2 were obtained from the manufacturer's datasheet supplied with the powder.

Table 3.1*. C103 powder chemical composition.*

Element	Niobium (Nb)	Hafnium (Hf)	Oxygen (O)	Titanium (Ti)	Rubidium (Rb)	Bromine (Br)
%wt	Balance	11.35	9.78	1.53	1.41	0.48

Table 3.2*.C103 powder properties.*

D10	**D50**	**D90**	**Hall flow**	**Apparent density**
24 µm	38.5 µm	57 µm	10.5 s	5.15 g/cm^3

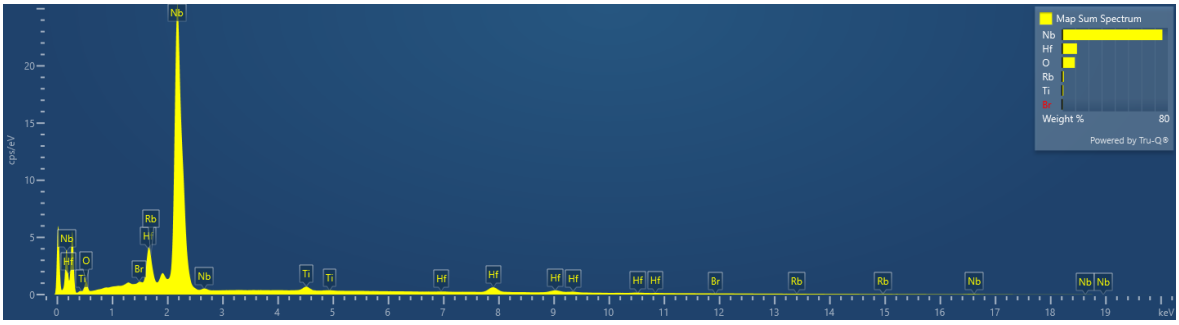


Figure 3.2*. EDS analysis performed on virgin C103 powder sample from 6K Additive.*

The acquired spectrum is dominated by the characteristic X-ray emission lines of niobium, confirming that Nb is the principal constituent of the investigated powder. Additional signals corresponding to hafnium and titanium are also detected, which is consistent with the nominal composition of the C103 niobium alloy, based on the Nb-Hf-Ti alloying system. A comparatively weak oxygen signal is also observed. Although EDS does not allow the origin of this signal to be established unambiguously, it may be associated with the presence of surface oxides on the powder particles, which can form during powder production, handling and storage. The spectrum also shows minor features tentatively attributed to bromine and rubidium; however, their very low intensity and the absence of these elements from the nominal C103 composition make their identification and significance uncertain. Therefore, these signals should not be interpreted as representative of the bulk chemical composition without further quantitative or complementary chemical analysis. Overall, the EDS spectrum qualitatively confirms the expected Nb-based nature of the virgin powder and the presence of Hf and Ti as alloying elements.

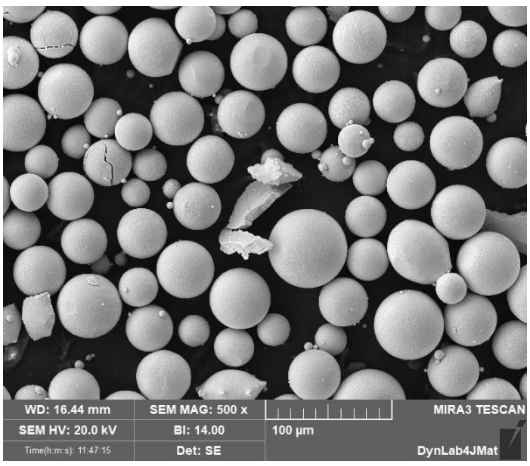


Figure 3.3. *Virgin C103 powder morphology SEM image, taken at 20.0 kV and 500x magnification.*

Figure 3.3 shows a scanning electron microscopy micrograph of the virgin C103 powder produced using the UniMelt® process at 500x magnification. The powder exhibits predominantly spherical particles with relatively smooth surfaces, indicating a morphology suitable for powder-based additive manufacturing processes. A limited number of satellites and irregularly shaped particles can also be observed, although these features represent a minor fraction of the overall powder population. The predominantly spherical morphology is expected to promote good powder flowability and consistent powder feeding during LP-DED, whereas the presence of irregular particles and satellites may locally affect powder flow characteristics. In addition to these morphological features, a limited number of surface defects can be observed on individual powder particles. Crack-like linear discontinuities are visible on some particles. Although these features appear consistent with surface cracks, their extension into the particle volume cannot be determined from the SEM image alone. Their presence may represent a potential powder quality concern, as pre-existing surface discontinuities could act as preferential sites for defect formation during subsequent melting and solidification. However, based on the present analysis, no direct correlation can be established between these features and the defects observed in the deposited material.

Prior to the deposition experiments, the powder feed rate was calibrated to establish the relationship between the rotational speed of the powder feeder and the delivered mass flow rate. For this purpose, the polymer tube normally connected to the deposition head was

redirected into a collection container positioned on an electronic balance. For each measurement, the powder feeder and a timer were started simultaneously. A collection time of 4 min was selected to ensure stable powder flow throughout the measurement. At the end of the test, the collected powder was weighed, and the average powder feed rate [g/min] was calculated by dividing the measured mass by the collection time. The procedure was repeated at powder feeder rotational speeds of 2, 3, 4, 5, and 8 rpm. The resulting calibration curve, shown in Figure 3.4, reports the powder feed rate as a function of the feeder rotational speed. A linear interpolation of the experimental data demonstrated a linear relationship, allowing the calibration curve to be used for estimating the powder feed rate at intermediate rotational speeds.

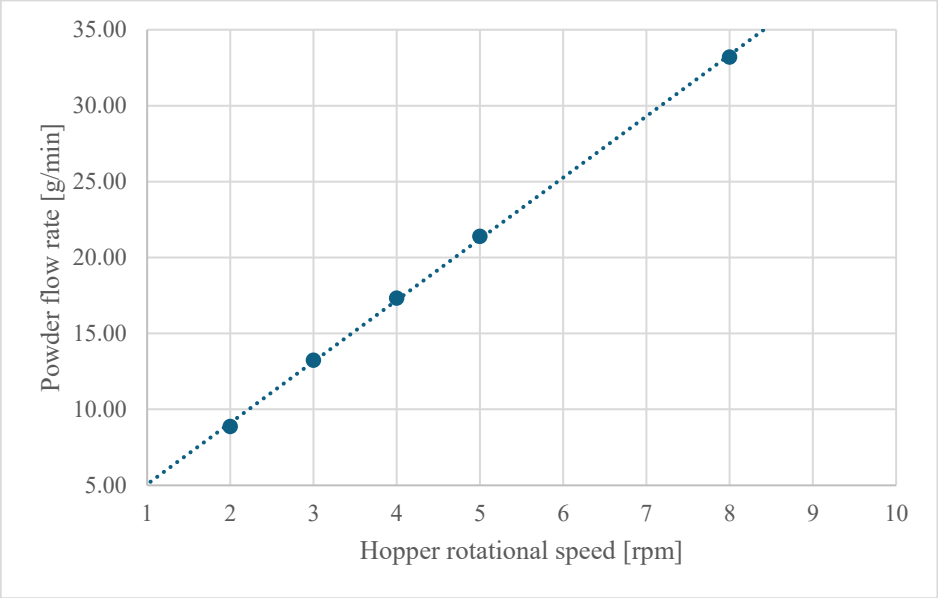


Figure 3.4. *Powder flow rate analysis.*

3.3 DEPOSITION STRATEGY

For all deposition experiments, except for the single-track specimens and the case study component, a deposition strategy consisting of a contour pass followed by a zigzag infill pattern was adopted. To improve the homogeneity of the deposited material and reduce the accumulation of directional effects, the deposition direction was rotated by 90° after the completion of each layer. A schematic representation of the adopted deposition strategy is shown in Figure 3.5.

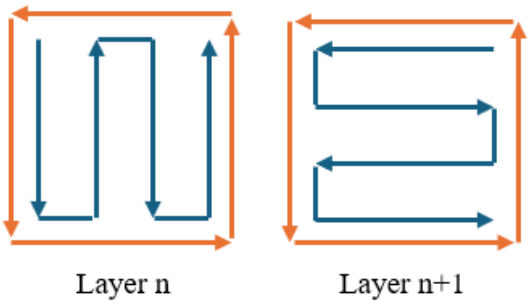


Figure 3.5*. Schematic of the deposition strategy. Boundary passes in orange and filling in blue.*

Regarding the case-study component, the deposition strategy was modelled using Mastercam software and subdivided into three main regions, each corresponding to a different deposition strategy. This subdivision was necessary both because of geometrical

restrictions imposed by the gas-shielding envelope and to optimize the deposition strategy according to the geometrical features of each region. The three regions are shown in Figure 3.6. The adopted deposition strategies were as follows:

- Region 1: one boundary contour followed by a zigzag filling pattern. The deposition direction was rotated by 90° after each layer.
- Region 2: the solid geometry was first converted into a surface to be used as reference geometry. The surface slicing function available in Mastercam was then used to generate the deposition paths along the reference surface and it was extended for the required number of beads. Since this region was inclined, the cylindrical substrate was mounted on a roto-tilt table. During the deposition of the first bead, the roto-tilt table was tilted and rotated while the deposition head was kept fixed. This configuration enabled a more precise and mechanically stable deposition. For the subsequent beads, the table was returned to its original position.
- Region 3: a different deposition strategy was required because of the geometrical restrictions imposed by the shielding head envelope. If the table had remained in its original position, the deposition head would have collided with the previously deposited Region 2. To overcome this limitation, the table was tilted by 90°, changing the Z-axis orientation from upward to leftward. The rotary slicing function implemented in Mastercam was then used to generate ring-like deposition paths, using the lateral surface of Region 1 as the deposition substrate. During deposition, the deposition head was kept fixed while the table was rotated.

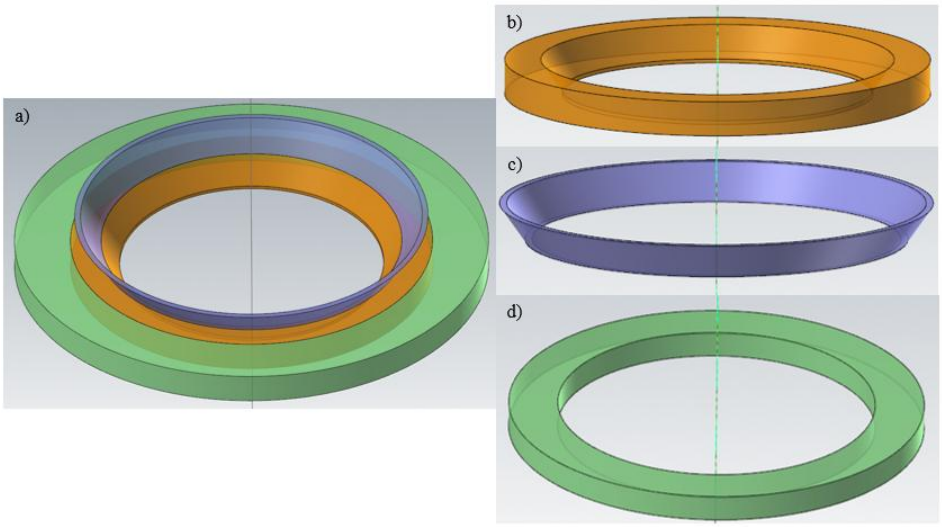


Figure 3.6. *a) complete case-study geometry; b) Region; c) Region 2; d) region 3.*

3.4 CUTTING

The components were deposited on 240x140x10 mm^3 Ti6Al4V substrate plates. The selection of this titanium alloy was based on a review of the available literature concerning the LP-DED processing of C103 alloy, in which Ti6Al4V is the substrate material most adopted [38], [117], [118], [119].

Cross-sectional specimens for both the single-track characterization and the porosity analysis of the cubes (Chapter 4) were prepared using a Mecatome T330 precision cutting machine by Presi. The samples were sectioned using an A60L cutting disk, having

dimensions 300x2x32 mm, under continuous coolant flow supplied through two nozzles, preventing excessive temperature rise during the cutting operation.



Figure 3.7. *Presi Mecatome T330 cutting machine.*

A different approach was adopted for the single scan tracks and the tensile specimen. Since the Mecatome T330 removes approximately 2 mm of material due to the thickness of the cutting disk, the tensile bar was cut at CIM 4.0-Competence for Industry and Manufacturing using wire electrical discharge machining (W-EDM). This process minimizes material loss, which is particularly important given the limited amount of deposited material available for mechanical testing. However, owing to the relatively low electrical conductivity of C103 (8.62–11.5 %IACS [140]), W-EDM is characterized by relatively long machining times.

Both the tensile specimen and the case study component were finished via machining to achieve the required geometrical dimensions and features, dimensional tolerances and surface finish.

The sectioning layouts used for the plate containing the single-track specimens and the cube specimens are illustrated in Figure 3.8 and Figure 3.9, respectively.

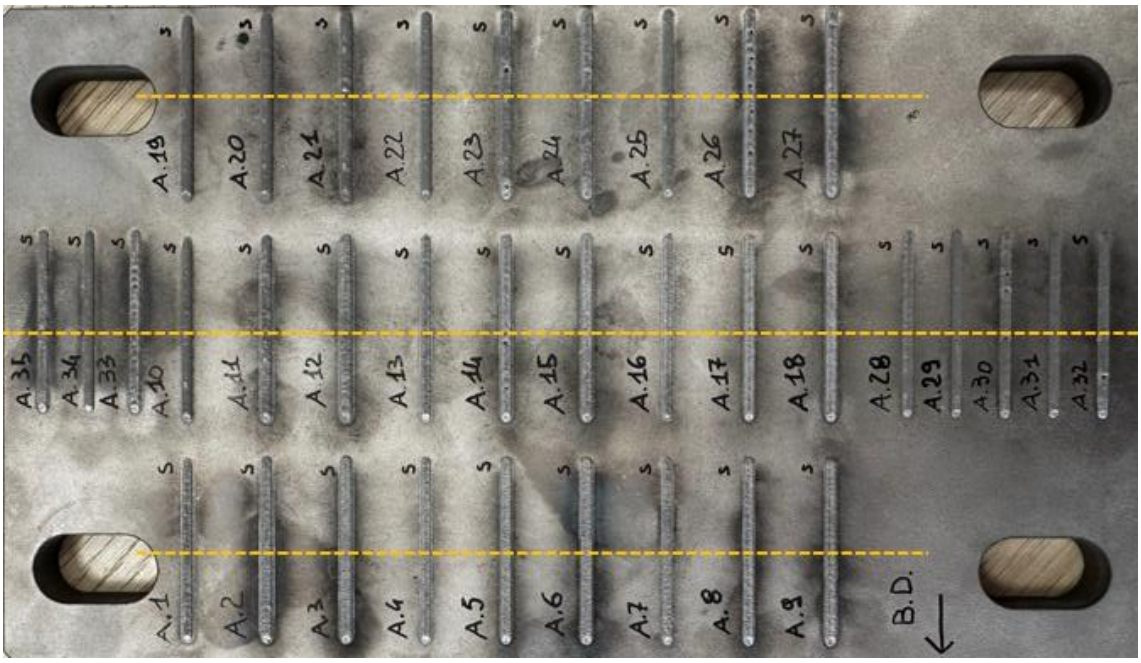


Figure 3.8. *Single-track scans cutting layout.*

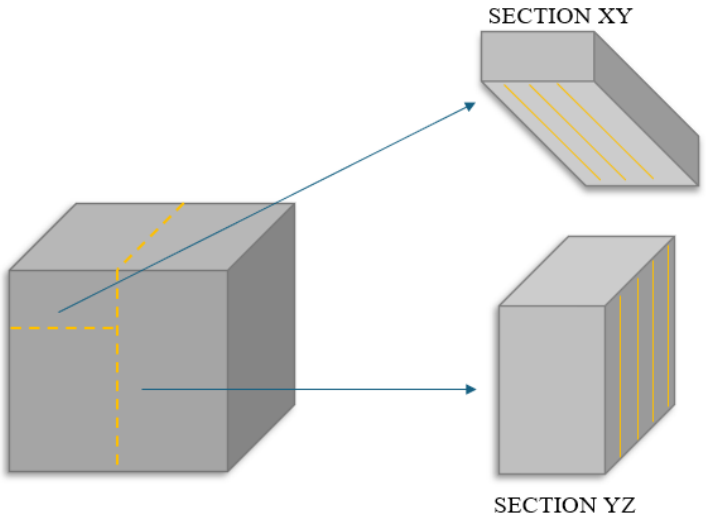


Figure 3.9. *Cubes cutting layout.*

3.5 MOUNTING

After sectioning, the samples were mounted using a combination of epoxy and phenolic resin with a Presi Mecapress 3 mounting press. Each specimen was placed on a 40 mm diameter mounting base and successively covered with epoxy, first, and then phenolic resin. The mounting press was then closed, and the encapsulation cycle was carried out under a load of 1100 daN. During the process, the resin was heated to 180 °C over 330 s, followed by a cooling stage lasting 210 s to obtain fully mounted specimens suitable for subsequent metallographic preparation



Figure 3.10. *Presi Mecapress 3 mounting machine.*

3.6 GRINDING AND POLISHING

After mounting, the samples were polished using a Presi Mecatech 234 automatic polishing machine. The system is equipped with a rotating specimen holder capable of both clockwise and counterclockwise rotation, ensuring uniform material removal during the polishing process. Lubrication and cooling were provided by a multijet water distribution system, in which water was continuously supplied to the polishing surface throughout the operation.



Figure 3.11. *Presi Mecatech 234 polishing machine.*

Each specimen underwent a multistep grinding and polishing procedure using progressively finer silicon carbide abrasive papers. After each polishing step, the surface was visually inspected to verify the complete removal of scratches generated during the previous stage or residual impurities. The abrasive papers employed and the corresponding polishing parameters are summarized in Table 3.3.

The objective of the polishing procedure was to obtain a mirror-like surface suitable for subsequent metallographic examination. Although the polishing sequence substantially reduced the surface defects, minor scratches remained visible after several polishing cycles. It must be pointed out that these scratches did not interfere with the metallographic analysis. Upon completion of the preparation, the specimens were cleaned with water or, when necessary, acetone, and finally dried using compressed air.

Table 3.3. *Grinding and polishing parameters*

Paper	Force [daN]	Time [s]	Disk RPM	Holder RPM
P120	0.8	120 (+60 extra if needed)	200	100
P180	0.5	120	200	100
P320	0.5	120	200	100
P400	0.5	180	200	100
P1000	1.5	600	200	100
P2500	1.5	600	200	100
P4000	1.5	600 (+300 extra if needed)	200	100

3.7 MICROGRAPHY

All microscopic images were acquired using a Motic AE2000 MET, an inverted metallurgical microscope designed to inspect polished cross-sections, equipped with a 5x objective lens, providing a total magnification of 100x. The acquired images were subsequently analyzed using the microscope manufacturer's proprietary software, Motic Images Plus 3.0.



Figure 3.12*. Motic AE2000 MET microscope.*

3.8 POROSITY ANALYSIS

The porosity of the cubic specimens was evaluated using the porosity analysis function available in Motic Images Plus 3.0. The software identifies differences in color within the metallographic images and calculates the area fraction occupied by black regions, which correspond to pores, including both gas porosity and lack-of-fusion defects. To ensure a representative characterization of the deposited material, the polished cross-section of each specimen was divided into five regions, as shown in Figure 3.13. Five micrographs were acquired and analyzed for each region. The porosity results are reported as the average area fraction for each region together with the corresponding standard deviation. All images were acquired using the same magnification and analyzed using identical threshold settings.

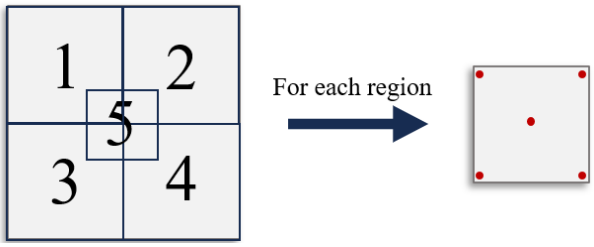


Figure 3.13. *Cube surface subdivision for porosity analysis and points where images were taken for each region.*

According to the third-party requirements, the deposited specimens were required to exhibit a minimum relative density of 95%. Consequently, only specimens satisfying this acceptance criterion were considered suitable for the subsequent stages of the study.

3.9 TENSILE TEST

A tensile specimen complying with the ASTM E8/E8M-25 [141] standard was machined from a deposited bar measuring 20x100x20 mm. The chosen specification was the one for test specimens with gauge length five times the diameter. The tensile test was carried out at CIM 4.0 using an Instron 68FM-100 universal testing machine under controlled laboratory conditions at an ambient temperature of 24 °C.



Figure 3.14. *Instron 68FM-100 Dual Column Floor Model.*

4 RESULTS AND DISCUSSION

4.1 SINGLE-TRACKS ANALYSIS

The first stage of the experimental campaign consisted of single-tracks analysis, aimed at identifying a suitable combination of laser power, scanning speed, and powder feed rate for the subsequent deposition experiments. The deposited tracks were sectioned, mounted, ground and polished to obtain metallographic cross-sections. A metallurgical microscope was then used to evaluate the main geometrical characteristics of the tracks, namely their width and height.

4.1.1 Parameters overview

A comprehensive literature review was initially conducted to establish a suitable starting point for the development of the deposition parameters. The selection criteria were limited to studies employing LP-DED for the processing of C103 alloy. Based on these criteria, six scientific publications were identified and used as the primary reference for defining the initial process parameters. The selected studies are summarized in Table 4.1.

***Table 4.1**. Scientific papers identified for process parameters development.*

Author	Building strategy	Building substrate material	Reference
Colon et al.	Bulk specimens	Ti6Al4V	[117]
Panicker et al.	Multi tracks single layer	Ti6Al4V	[119]
Colon et al.	Thin walls	Ti6Al4V	[38]
Palacios	Thin walls	Molybdenum	[121]
Colon et al.	Thin walls	Ti6Al4V	[118]
Thapliyal et al.	n.a.	Ti6Al4V	[120]

Based on the information extracted from the literature, an initial design of experiments for the single-track deposition was established. Three levels of laser power, three scanning speeds and three powder feed rates were selected, resulting in the parameter combinations reported in Table 4.2 for tracks A.1-A.27. Following the deposition of the first tracks, an additional set of experiments, Table 4.3, was designed to investigate the feasibility of alternative processing conditions. All the remaining process parameters, including the laser spot size, shielding gas flow rate and central purge flow rate, were kept constant throughout the study.

Table 4.2. *Process parameters choice after literature review.*

#Track	Laser power [W]	Scanning speed [mm/min]	Hopper rotational speed [rpm]
A.1	1000	400	3
A.2	1300		
A.3	1500		
A.4	1000	600	
A.5	1300		
A.6	1500		
A.7	1000	800	
A.8	1300		
A.9	1500		
A.10	1000	400	4
A.11	1300		
A.12	1500		
A.13	1000	600	
A.14	1300		
A.15	1500		
A.16	1000	800	
A.17	1300		
A.18	1500		
A.19	1000	400	5
A.20	1300		
A.21	1500		
A.22	1000	600	
A.23	1300		
A.24	1500		
A.25	1000	800	
A.26	1300		
A.27	1500		

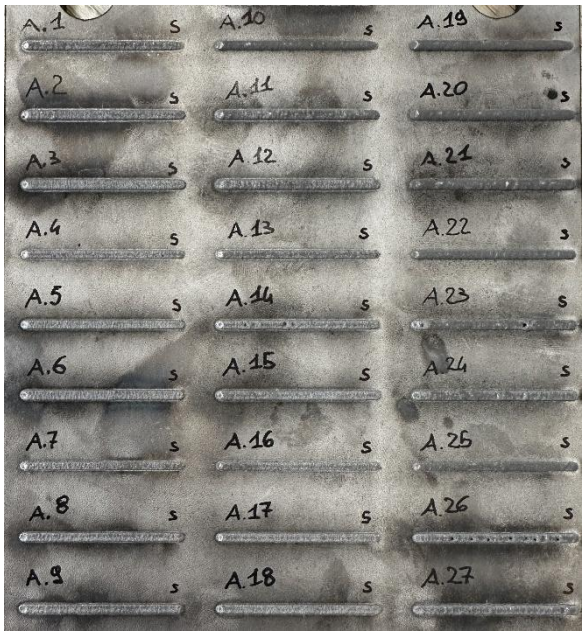


Figure 4.1. *Deposited tracks A.1-A.27, where s indicates the deposition starting point*

Table 4.3. *Second set of process parameters choice.*

#Track	Laser power [W]	Scanning speed [mm/min]	Hopper rotational speed [rpm]
A.28	1000	1000	5
A.29	1000		6
A.30	1300		
A.31	1000	1100	
A.32	1300		
A.33	1500		
A.34	1000	1200	
A.35	1300		

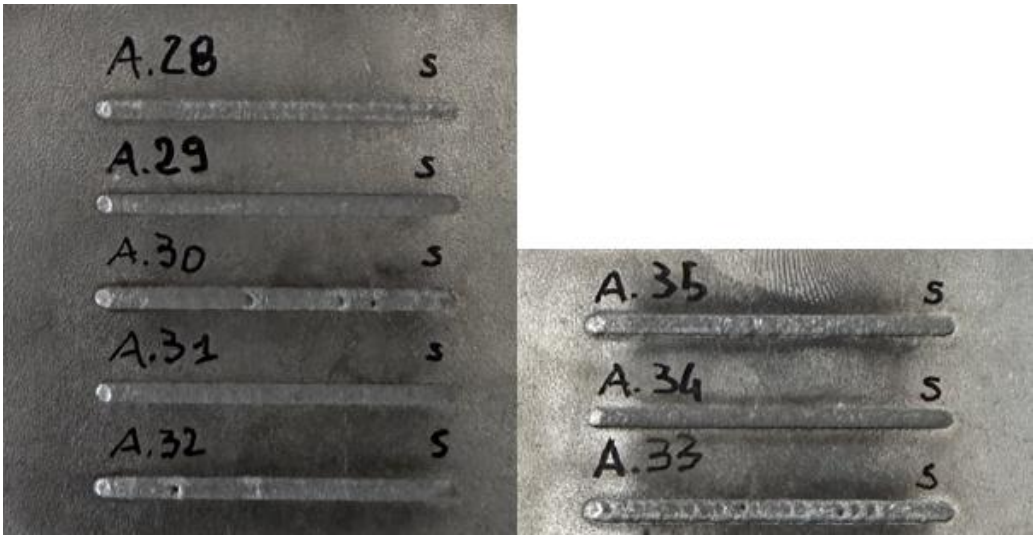


Figure 4.2. *Deposited tracks A.28-A.35, where s indicates the deposition starting point.*

4.1.2 Visual inspection

Following the deposition of all single-track specimens, a preliminary visual inspection was carried out to identify the presence of major surface defects prior to metallographic characterization. This initial assessment revealed eight tracks exhibiting visible porosity, namely A.14, A.23, A.24, A.26, A.30, A.32, and A.33. In addition, track A.29 exhibited poor adhesion to the substrate, as part of the deposited bead could be detached by applying a small lateral force manually.

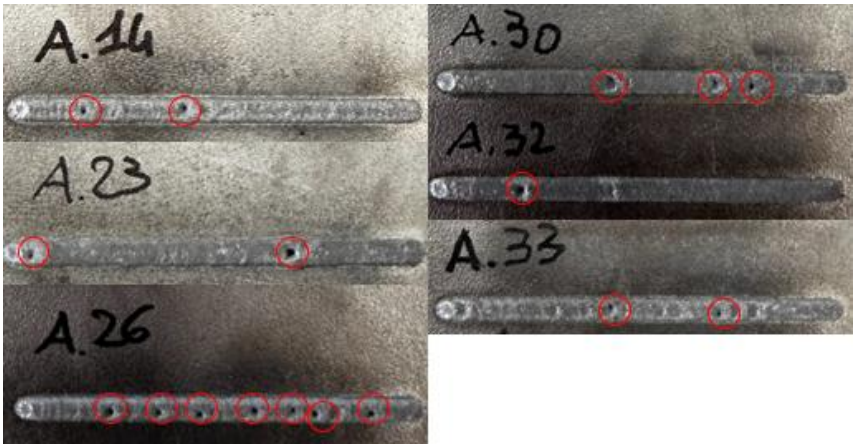


Figure 4.3. *Tracks with visible pores.*

4.1.3 Micrography

All single-track specimens were sectioned and prepared for metallographic examination according to the procedure described in Sections 3.4-3.7. The cross-sectional analysis was performed to measure the main geometrical characteristics of the deposited tracks, namely the track height, width and penetration depth. The values reported in Table 4.4 correspond to the average of three measurements performed for each geometrical parameter. Based on the measured track height and penetration depth, the dilution was subsequently calculated according to Equation 2.5. The corresponding dilution values are also reported in Table 4.4.

Table 4.4. *Tracks dimensions report.*

#Track	Height [mm]	Penetration [mm]	Width [mm]	Dilution
A.1	0.757	0.143	1.878	16%
A.2	0.753	0.249	2.142	25%
A.3	0.774	0.283	2.337	27%
A.4	0.438	0.122	1.756	22%
A.5	0.593	0.333	2.218	36%
A.6	0.555	0.209	2.019	27%
A.7	0.401	0.156	1.762	28%
A.8	0.463	0.263	2.059	36%
A.9	0.519	0.357	2.212	41%
A.10	1.038	0.035	1.880	3%
A.11	0.991	0.269	2.193	21%
A.12	1.070	0.305	2.408	22%
A.13	0.680	0.140	1.915	17%
A.14	0.780	0.140	2.119	15%
A.15	0.729	0.245	2.201	25%
A.16	0.500	0.087	1.890	15%
A.17	0.530	0.193	2.000	27%
A.18	0.567	0.200	2.158	26%
A.19	1.126	0.000	2.006	0%
A.20	1.254	0.112	2.117	8%
A.21	1.233	0.192	2.438	13%
A.22	0.884	0.030	1.795	3%
A.23	0.833	0.183	2.186	18%
A.24	0.785	0.320	2.400	29%
A.25	0.645	0.156	1.972	20%
A.26	0.687	0.230	2.291	25%
A.27	0.751	0.250	2.210	25%
A.28	0.615	0.115	1.895	16%
A.29	0.776	0.000	1.769	0%
A.30	0.756	0.086	2.066	10%
A.31	0.682	0.000	1.703	0%
A.32	0.699	0.141	2.012	17%
A.33	0.617	0.185	2.141	23%
A.34	0.643	0.023	1.705	3%
A.35	0.572	0.145	1.908	20%

An initial assessment of the results reported in Table 4.4 highlights that some parameter combinations did not produce any penetration into the substrate and, consequently, exhibited zero dilution. This behavior was observed for tracks A.19, A.29 and A.31. Since adequate metallurgical bonding is a prerequisite for multilayer deposition, these parameter sets were excluded from further consideration. According to the literature, an acceptable dilution generally ranges between 10% and 30%; therefore, all parameter combinations falling outside this interval were discarded from the pool of candidate processing conditions. The deposited track height was then evaluated to identify a suitable layer thickness for subsequent multilayer deposition. Based on AltForm's industrial experience, a target height of approximately 0.7 mm was considered desirable, as larger layer thicknesses increase the deposition rate and reduce the overall manufacturing time. Finally, the measured track width was compared with the nominal laser spot diameter of 2 mm. Since the deposited material is expected to be distributed over an area close to the laser spot size, track widths approaching this value were considered indicative of stable deposition conditions.

The evaluation of the single-track deposition was not limited to the quantitative measurements reported in Table 4.4. A qualitative assessment of the metallographic cross-sections, Figures 4.4-4.7, was also performed to identify morphological defects that could compromise the quality of subsequent multilayer deposition.

Gas porosity was observed in tracks A.1, A.11-12, A.19-21, A.23-24, A.26-28, A.33, and A.35. Since porosity can negatively affect both the metallurgical integrity of the deposited material and the mechanical performance of the final component, these parameter combinations were considered unsuitable for further investigation.

The geometry of the deposited beads was also used as a selection criterion. Tracks A.4, A.14, A.16-17, A.33, and A.35 exhibited a flat-top surface which may reduce the overlap and metallurgical bonding between successive layers during multilayer deposition. Conversely, tracks A.3, A.5-6, A.8-9, A.18, A.24, and A.26 showed a concave bead profile, potentially leading to an unstable layer-by-layer growth along the build direction. Tracks A.25, 28, A.30-32, and A.34 presented irregular bead geometries. These latter defects were mainly observed at high powder feed rates, suggesting that excessive powder delivery may have contributed to the instability of the deposited tracks.

Track penetration was considered another key selection criterion. Tracks A.1, A.4, A.7, A.10, A.13-14, A.16-17, A.19-23, A.25, and A.28-35 exhibited penetration depths below 0.2 mm, which was considered the minimum acceptable value to ensure sufficient metallurgical bonding with the substrate. In addition, tracks A.10, A.19, A.20, A.22, A.29, A.31, and A.34 showed dilution values below 10%, whereas no track exceeded the upper acceptance limit of 30%.

Based on the measured geometrical characteristics, the calculated dilution values and the qualitative analysis of the metallographic cross-sections, two parameter sets were selected for the subsequent cube deposition.

Table 4.5. *Parameter sets chosen for I manufacturing trial..*

#Track	Laser Power [W]	Scanning Speed [mm/min]	Hopper rotational speed [rpm]	Width [mm]	Height [mm]	Dilution
A.2	1300	400	3	2.142	0.753	25%
A.15	1500	600	4	2.201	0.729	25%

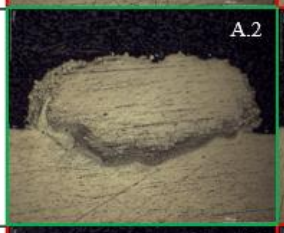
3 RPM = 13.23 g/min	400 mm/min	600 mm/min	800 mm/min
1000 W			
1300 W			
1500 W			

Figure 4.4. *Cross-sectional images tracks A.1-A.9.*

4 RPM = 17.33 g/min	400 mm/min	600 mm/min	800 mm/min
1000 W			
1300 W			
1500 W			

Figure 4.5. *Cross-sectional images tracks A.10-A.18.*

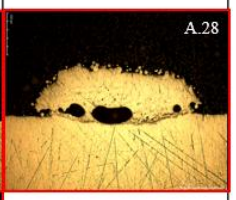
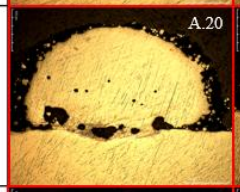
5 RPM = 21.40 g/min	400 mm/min	600 mm/min	800 mm/min	1000 mm/min
1000 W				
1300 W				/
1500 W				/

Figure 4.6. *Cross-sectional images tracks A.19-A.28.*

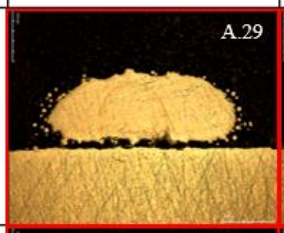
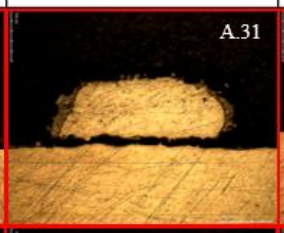
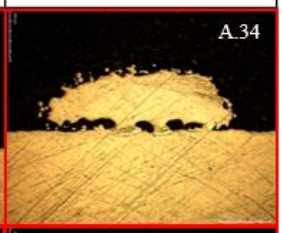
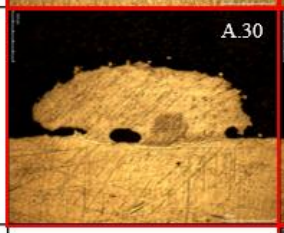
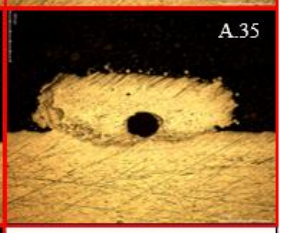
6 RPM = 26.52 g/min	400 mm/min	600 mm/min	800 mm/min
1000 W			
1300 W			
1500 W	/		/

Figure 4.7*. Cross-sectional images tracks A.29-A.35.*

4.2 CUBE ANALYSIS

4.2.1 I manufacturing trial

***Table 4.6**. Parameters for the I manufacturing trial.*

#Cube	Laser Power [W]	Scanning Speed [mm/min]	Hopper rotational speed [rpm]	Layer thickness [mm]	Overlap
B.1	1300	400	3	0.7	30%
B.2	1500	600	4	0.7	30%

The process parameters selected from the single-track analysis, Section 4.1, were adopted for the first cubes manufacturing trial. Since neither single-layer nor thin-wall deposition analyses were performed, the hatch spacing was defined based on AltForm's industrial experience. A track overlap of 30% was selected, which, considering a nominal laser spot diameter and average track width of 2 mm, corresponds to a hatch distance of 1.4 mm. The layer thickness was determined from the results of the single-track analysis. As the average track height was approximately 0.7 mm, this value was adopted as the nominal layer thickness for the cubes deposition. Furthermore, to address the limited penetration observed during the single-track experiments, the Ti6Al4V substrate was preheated to 120 °C, corresponding to the maximum temperature achievable with the available equipment. The same preheating strategy was adopted from the first manufacturing trial onwards and maintained throughout all subsequent deposition experiments.

Figure 4.8 shows specimen B.1. As can be observed, the specimen exhibits a regular geometry with only a limited accumulation of adhered powder particles on the lateral faces parallel to the powder delivery direction. The top view of the specimen, Figure 4.8b, reveals that two deposition tracks are missing in the final layer. This defect resulted from an unexpected laser fault, which interrupted the deposition process before completion. Figure 4.8 shows the specimen in the as-built condition, prior to surface cleaning. The yellow oxide layer was superficial and was subsequently removed using a metallic brush.

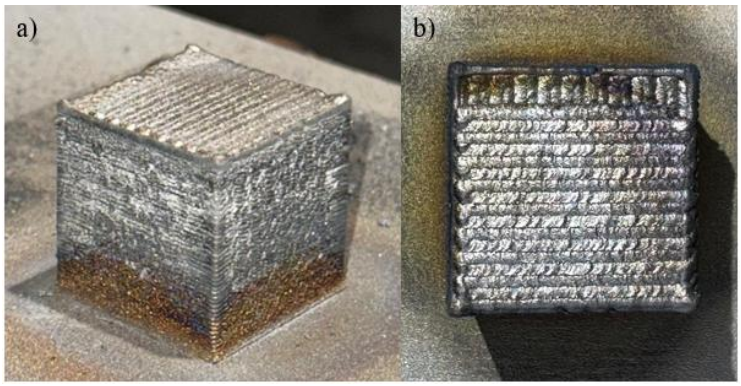


***Figure 4.8.** Cube B.1. a) side view; b) top view.*

During the deposition of the cube B.2, a failure of the gas supply system occurred, resulting in insufficient shielding and purge gas flow. Consequently, severe oxidation of both the deposited material and the Ti6Al4V substrate was observed. As shown in Figure 4.9, the substrate exhibited blue-purple colors, while the deposited material presented yellow-blue oxidation colors, confirming the loss of adequate shielding during the deposition process. The inadequate process conditions were also associated with excessive heat

accumulation, as indicated by the formation of surface bulges and material accumulation on both the top surface and the lateral faces of the specimen. Throughout the deposition process, the cube remained incandescent until the process was interrupted, indicating significant heat accumulation and insufficient cooling between successive laser passes.

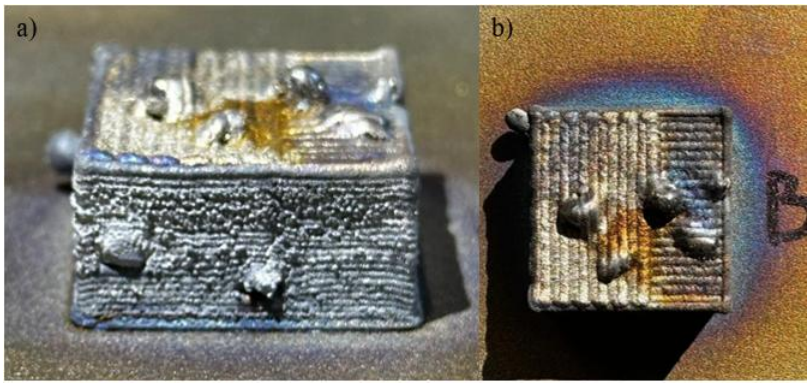


Figure 4.9. *Cube B.2. a) side view; b) top view.*

The calculated Volumetric Energy Density, according to Equation 2.3, resulted in 199.0 J/mm^3 for cube B.1 and 153.1 J/mm^3 for B.2.

4.2.1.1 Micrography and porosity analysis

Only specimen B.1 was subjected to porosity analysis, following the procedure described in Sections 3.4-3.7. Specimen B.2 was not analyzed because the deposition process was interrupted due to the gas supply failure previously described, preventing the manufacture of a representative sample. The micrographs presented in Figure 4.10 are representative examples, all porosity measurements were performed on the complete dataset according to the methodology described in Section 3.8

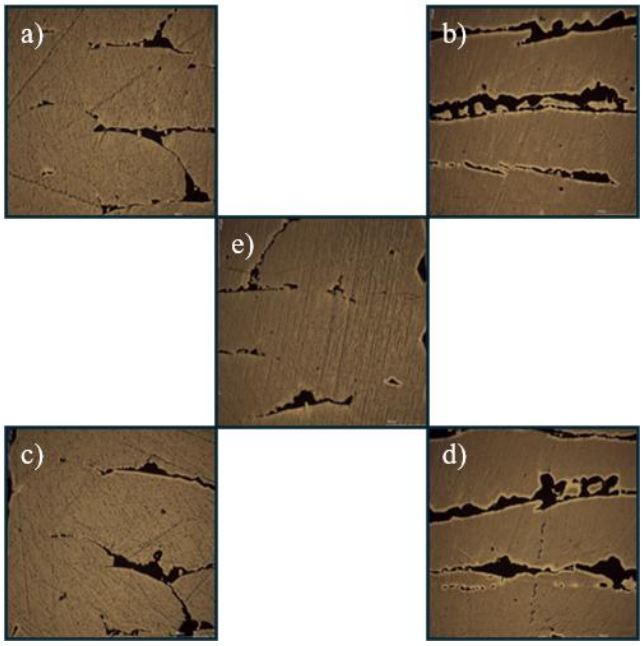


Figure 4.10. *Cube B.1 YZ plane micrograph. a) taken from region 1; b) taken from region 2; c) taken from region 3; d) taken from region 4; e) taken from region 5.*

As can be observed from Figure 4.10, lack-of-fusion defects represent the predominant porosity mechanism in specimen B.1, whereas only a limited amount of gas porosity is

visible. The quantitative results for plane YZ, reported in Table 4.7, further confirm that the measured porosity level, mainly associated with lack-of-fusion defects, exceeds the acceptance criterion established for the study.

Table 4.7. *Cube B.1 YZ plane porosity measurements.*

Region	Max porosity	Min porosity	Average porosity	Standard deviation
1	11.68%	4.25%	7.87%	3.50
2	9.79%	2.31%	5.52%	3.23
3	9.57%	5.85%	7.93%	1.53
4	10.11%	2.47%	6.58%	2.97
5	11.57%	6.88%	9.59%	1.96

Being the porosity threshold non achieved, the porosity in the XY plane was not measured for B.1 sample.

4.2.2 II manufacturing trial

Table 4.8. *Parameters for the II manufacturing trial.*

#Cube	Laser Power [W]	Scanning Speed [mm/min]	Hopper rotational speed [rpm]	Layer thickness [mm]	Overlap
C.1	1300	400	3	0.5	30%
C.2	1400	600	3	0.5	30%

For the second manufacturing trial, the process parameters adopted for specimens B.1 and B.2 were refined to increase the relative density by reducing the occurrence of lack-of-fusion defects. For both specimens, the layer thickness was reduced from 0.7 mm to 0.5 mm to improve the overlap between successive layers. In addition, the process parameters of specimen C.2 were further modified by reducing the laser power to 1400 W to limit heat accumulation. The powder feeder rotational speed was also decreased to match that adopted for specimen C.1. The complete set of process parameters is reported in Table 4.8. Using these parameters C.1 has a Volumetric Energy Density equal to 278.6 J/mm^3 whereas C.2 has a VED of 200.0 J/mm^3.

Figure 4.11 shows specimen C.1. The specimen exhibits a regular cubic geometry with no visible macroscopic distortions, although its overall geometry appears slightly less regular than that of specimen B.1. This behavior may be attributed to the reduced specimen dimensions adopted to minimize powder consumption. The smaller deposition area likely resulted in more frequent laser passes over the same region, promoting greater heat accumulation (not as high as specimen B.2) during the manufacturing process. Adhered powder particles are visible on the lateral surfaces parallel to the powder delivery direction and appear more pronounced than those observed for specimen B.1. In addition, localized material accumulation is present at the cube corners. A similar surface morphology was also observed for specimen C.2, Figure 4.12.

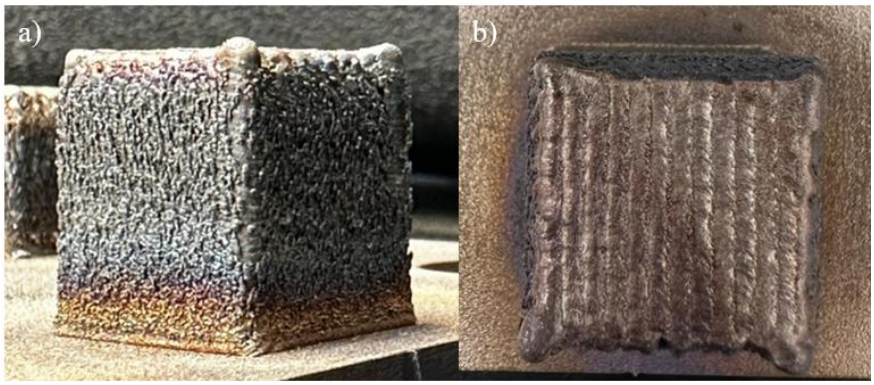


***Figure 4.11**. Cube C.1. a) side view; b) top view.*

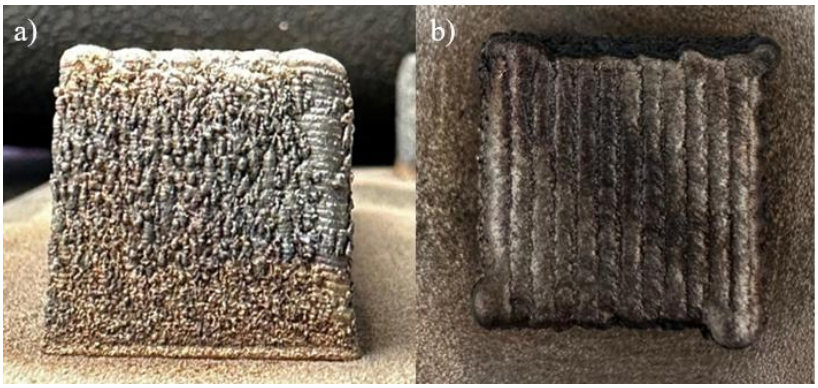


***Figure 4.12.** Cube C.2. a) side view; b) top view.*

4.2.2.1 C.1 micrography and porosity analysis

Figure 4.13 presents representative micrographs of specimen C.1 in the YZ plane. The corresponding quantitative porosity measurements are reported in Table 4.9. As can be observed from the micrographs, lack-of-fusion defects remain the predominant porosity mechanism, although their occurrence is lower than that observed for specimen B.1. Gas porosity remains limited throughout the analyzed cross-section.

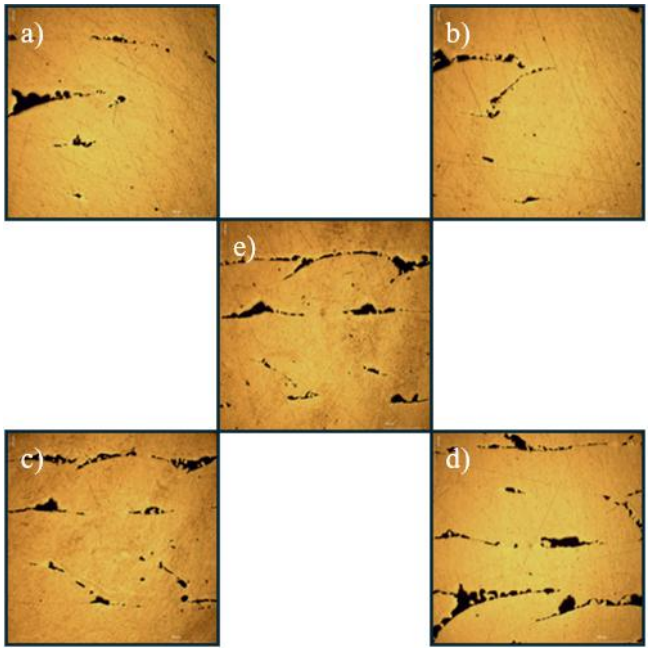


***Figure 4.13.** Cube C.1 YZ plane micrograph. a) taken from region 1; b) taken from region 2; c) taken from region 3; d) taken from region 4; e) taken from region 5.*

Table 4.9. *Cube C.1 YZ plane porosity measurements.*

Region	Max porosity	Min porosity	Average porosity	Standard deviation
1	3.32%	1.75%	2.54%	0.72
2	4.08%	1.91%	2.80%	0.90
3	5.27%	2.03%	4.31%	1.34
4	5.87%	2.47%	4.86%	1.43
5	5.87%	3.13%	4.59%	1.22

The quantitative porosity measurements are consistent with the qualitative observations obtained from the metallographic images. Although some of the analyzed regions exhibited a maximum porosity value slightly exceeding the maximum admissible limit, the average porosity of specimen C.1 remained below the 5% acceptance criterion established by the third party. Therefore, the specimen was not discarded, and the porosity analysis was extended to the XY plane to further assess the porosity distribution throughout the deposited material. Representative micrographs of the XY cross-section are shown in Figure 4.14.

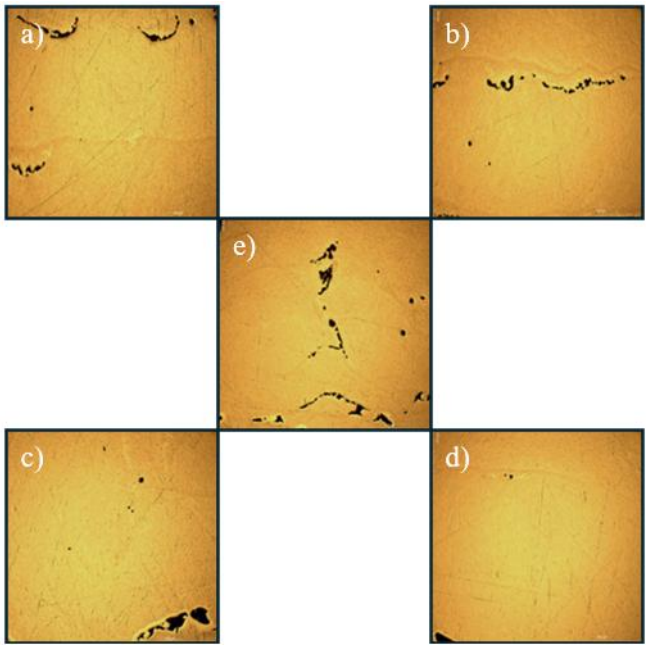


Figure 4.14. *Cube C.1 XY plane micrograph. a) taken from region 1; b) taken from region 2; c) taken from region 3; d) taken from region 4; e) taken from region 5.*

Table 4.10. *Cube C.1 XY plane porosity measurements.*

Region	Max porosity	Min porosity	Average porosity	Standard deviation
1	10.70%	0.98%	4.28%	3.87
2	7.19%	0.73%	2.31%	2.78
3	3.16%	1.20%	2.06%	0.81
4	1.98%	0.09%	1.18%	0.93
5	10.70%	1.61%	5.37%	4.37

The porosity analysis performed on the XY plane revealed a considerable variation in the porosity values measured within regions 1, 2 and 5. In these regions, the maximum porosity

reached approximately 10%, whereas the minimum values were below 1%, indicating a non-uniform distribution of porosity within the deposited material. Despite this variability, the average porosity remained below the maximum admissible threshold in all regions except region 5, where it slightly exceeded the acceptance criterion.

4.2.2.2 C.2 micrography and porosity analysis

The porosity analysis was repeated on specimen C.2 in the YZ plane following the same procedure. The representative micrographs shown in Figure 4.15 indicate a further reduction in the amount of lack-of-fusion defects compared with specimen C.1, suggesting an improvement in the deposited material quality achieved through the modified process parameters. This observation is consistent with the quantitative porosity measurements reported in Table 4.11, which confirm the reduction in porosity.

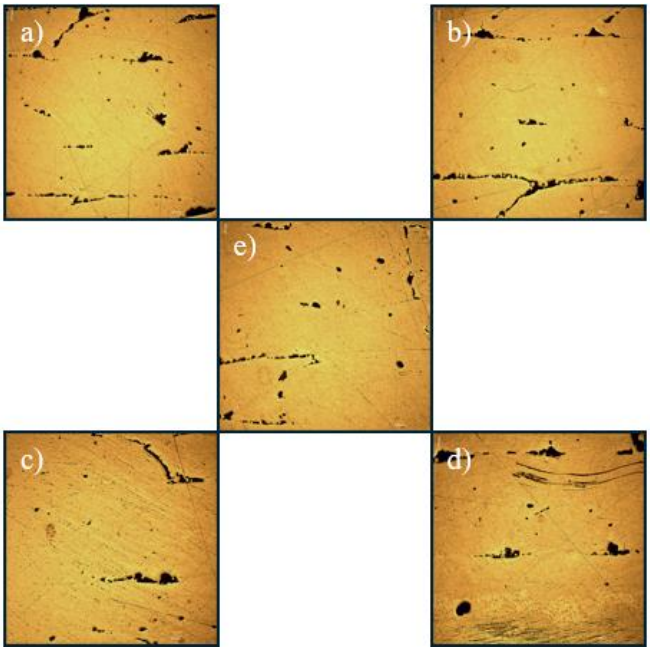


Figure 4.15. *Cube C.2 YZ plane micrograph. a) taken from region 1; b) taken from region 2; c) taken from region 3; d) taken from region 4; e) taken from region 5.*

Table 4.11. *Cube C.2 YZ plane porosity measurements.*

Region	Max porosity	Min porosity	Average porosity	Standard deviation
1	4.63%	1.06%	2.96%	1.45
2	4.55%	1.15%	2.43%	1.28
3	4.05%	2.07%	3.16%	0.86
4	4.25%	2.15%	3.28%	0.88
5	4.55%	2.58%	3.34%	0.94

The process parameters adopted for specimen C.2 resulted in maximum porosity values below the 5% acceptance threshold in all five analyzed regions, thereby satisfying the third-party requirements. Although the occurrence of lack-of-fusion defects was further reduced compared with specimen C.1, the metallographic analysis revealed a slightly more pronounced and widespread presence of gas porosity across the analyzed regions. A possible explanation is that the higher scanning speed reduced the melt pool lifetime, limiting the time available for entrapped gas bubbles to escape before solidification. However, since both

the laser power and the scanning speed were modified simultaneously, the individual contribution of each parameter cannot be isolated from the present results, and further investigations would be required to confirm this hypothesis. Nevertheless, from a process development perspective, the modified parameter set successfully reduced the occurrence of the more critical lack-of-fusion defects while maintaining the overall porosity below the acceptance threshold, representing an improvement over the previous manufacturing trial.

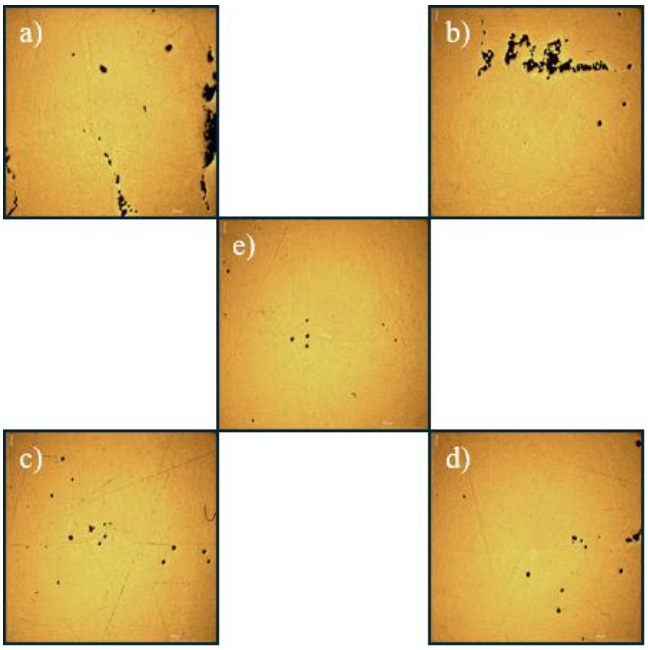


Figure 4.16. *Cube C.2 XY plane micrograph. a) taken from region 1; b) taken from region 2; c) taken from region 3; d) taken from region 4; e) taken from region 5.*

Table 4.12. *Cube C.2 XY plane porosity measurements.*

Region	Max porosity	Min porosity	Average porosity	Standard deviation
1	3.96%	1.63%	2.88%	0.98
2	4.99%	2.29%	3.71%	1.15
3	3.42%	0.01%	1.15%	1.59
4	2.53%	0.06%	0.87%	1.12
5	3.96%	0.09%	1.95%	2.00

The same trend observed in the YZ plane was also confirmed by the analysis of the XY cross-section. In this plane, the occurrence of lack-of-fusion defects was further reduced, whereas a higher number of smaller gas pores was observed throughout the area analyzed. This observation is consistent with the results obtained in the YZ plane and further supports the effectiveness of the selected process parameters in mitigating the more critical lack-of-fusion defects while maintaining the overall porosity within the acceptance limit.

4.2.3 III manufacturing trial

Table 4.13. *Parameters for the III manufacturing trial.*

#Cube	Laser Power [W]	Scanning Speed [mm/min]	Hopper rotational speed [rpm]	Layer thickness [mm]	Overlap
D.1	1500	600	3	0.35	30%
D.2	1400	600	2.5	0.35	30%

In the third manufacturing trial, the process parameters were further refined to reduce the lack-of-fusion defects observed during the YZ porosity analysis of the previous specimens. To increase the overlap between successive layers, the layer thickness was reduced from 0.5 mm to 0.35 mm for both specimen D.1 and D.2. In addition, the hopper rotational speed of specimen D.2 was decreased from 3 to 2.5 rpm, resulting in 11.02 g/min, to evaluate whether a proportional reduction in powder feed rate, consistent with the reduced layer thickness, could further improve the deposition quality. The resulting volumetric energy density was 306.1 J/mm^3 for specimen D.1 and 285.7 J/mm^3 for specimen D.2.

Figures 4.17 and 4.18 show the as-built specimens D.1 and D.2. Although both cubes were successfully manufactured, their geometry was less regular than that observed in the previous manufacturing trial. A possible explanation is the increased heat accumulation during deposition, which may have become more pronounced owing to the smaller specimen dimensions and the reduced layer thickness, resulting in more frequent laser passes over the same area. Adhered powder particles were still visible on the lateral surfaces, similarly to the specimens produced in the previous trials.

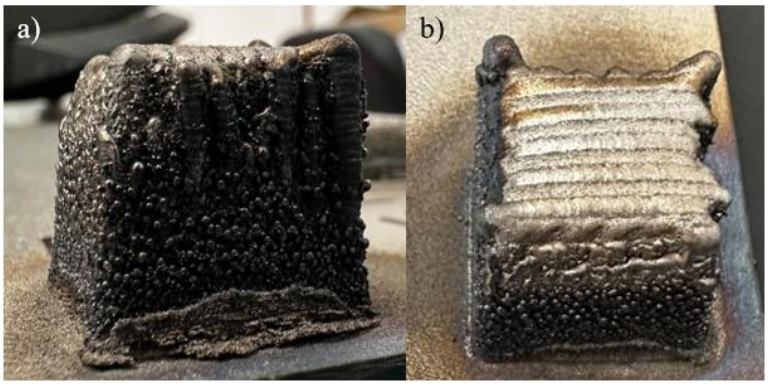


Figure 4.17. *Cube D.1. a) side view; b) top view.*

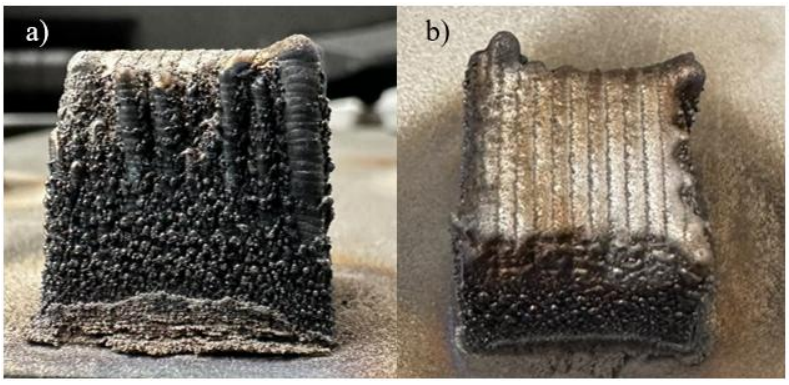


Figure 4.18. *Cube D.2. a) side view; b) top view.*

4.2.3.1 D.1 micrography and porosity analysis

Figure 4.19 shows a further reduction in the occurrence of lack-of-fusion defects compared with the specimens produced in the previous manufacturing trials. This observation is consistent with the quantitative porosity measurements reported in Table 4.14. As in the previous manufacturing trials, lack-of-fusion remained the dominant porosity mechanism, whereas gas porosity was comparatively limited.

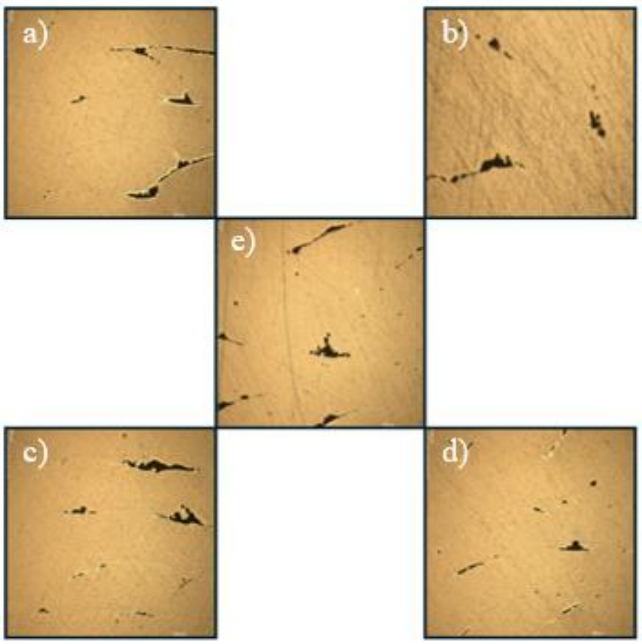


Figure 4.19. *Cube D.1 YZ plane micrograph. a) taken from region 1; b) taken from region 2; c) taken from region 3; d) taken from region 4; e) taken from region 5.*

Table 4.14*. Cube D.1 YZ plane porosity measurements.*

Region	Max porosity	Min porosity	Average porosity	Standard deviation
1	1.51%	0.81%	1.26%	0.29
2	1.87%	1.15%	1.42%	0.29
3	2.00%	0.27%	1.49%	0.69
4	1.82%	0.25%	1.28%	0.60
5	2.00%	1.14%	1.48%	0.37

The quantitative porosity measurements indicate a substantial improvement in the quality of the deposited material. The average porosity remained remarkably consistent across the five analyzed regions, ranging from 1.26% to 1.49%, suggesting a relatively uniform porosity distribution throughout the specimen. Furthermore, the maximum porosity measured in each region remained well below the 5% acceptance threshold.

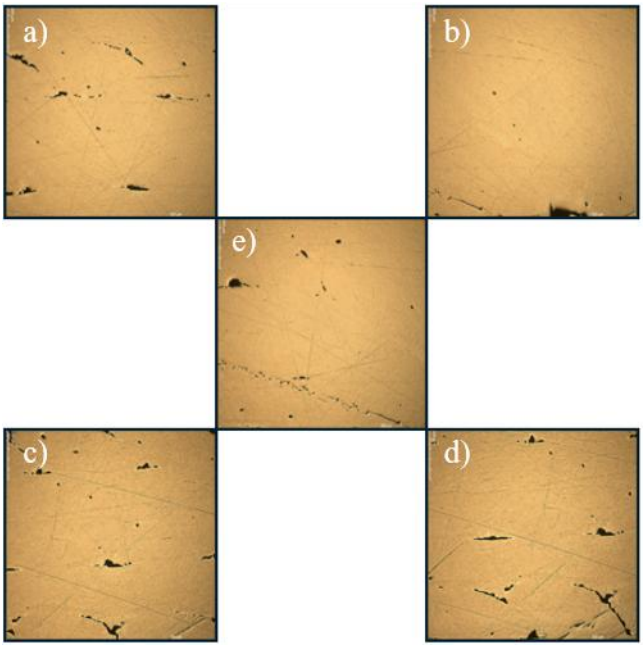


Figure 4.20. *Cube D.1 XY plane micrograph. a) taken from region 1; b) taken from region 2; c) taken from region 3; d) taken from region 4; e) taken from region 5.*

Table 4.15. *Cube D.1 XY plane porosity measurements.*

Region	Max porosity	Min porosity	Average porosity	Standard deviation
1	2.02%	1.00%	1.56%	0.43
2	0.97%	0.02%	0.57%	0.36
3	2.37%	0.93%	1.37%	0.63
4	1.20%	0.72%	0.94%	0.22
5	2.02%	0.86%	1.20%	0.55

Compared with the YZ plane, the porosity analysis performed on the XY plane revealed a lower overall average porosity, although some variability among the analyzed regions was still observed, Figure 4.20 and Table 4.15. The average porosity ranged from 0.57% to 1.56%, while the maximum porosity remained below 2.5% in all regions. The relatively low standard deviation values indicate a reasonably homogeneous porosity distribution throughout the analyzed plane.

4.2.3.2 D.2 micrography and porosity analysis

The process parameters adopted for specimen D.2 resulted in a further reduction in porosity compared with specimen D.1. These results suggest that reducing the powder feed rate, while maintaining the same layer thickness, had a beneficial effect on the deposition quality. A possible explanation is that the lower powder feed rate improved the interaction between the laser beam and the powder stream, reducing the amount of unmelted or partially melted particles and consequently mitigating the occurrence of lack-of-fusion defects. This trend was consistently observed in both the YZ and XY cross-sections, Figure 4.21 and Figure 4.22, indicating that the improvement in deposition quality was not limited to a single observation plane.

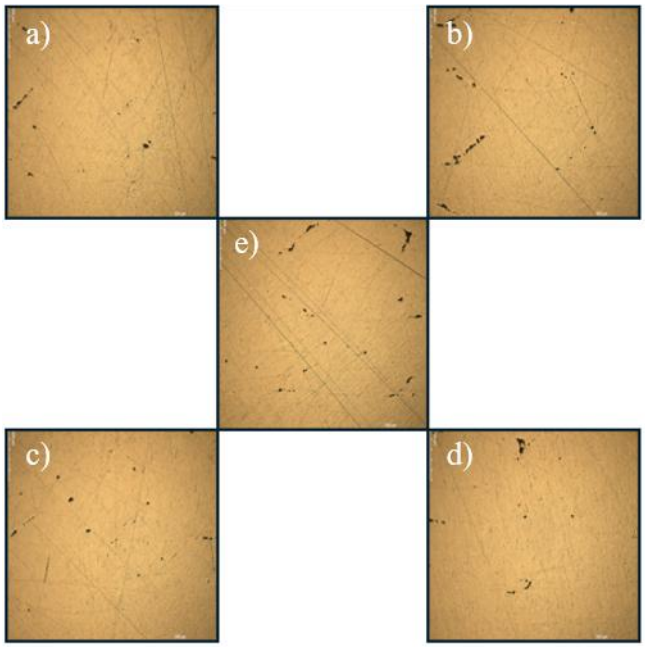


***Figure 4.21**. Cube D.2 YZ plane micrograph. a) taken from region 1; b) taken from region 2; c) taken from region 3; d) taken from region 4; e) taken from region 5.*

***Table 4.16.** Cube D.2 YZ plane porosity measurements.*

Region	Max porosity	Min porosity	Average porosity	Standard deviation
1	0.52%	0.15%	0.33%	0.18
2	0.49%	0.30%	0.41%	0.07
3	0.52%	0.33%	0.43%	0.08
4	0.56%	0.10%	0.40%	0.20
5	0.56%	0.41%	0.48%	0.07

The quantitative porosity measurements reported in Table 4.16 demonstrate a substantial improvement in the deposition quality compared with specimen D.1. The average porosity was reduced by approximately 70%. Furthermore, the maximum measured porosity did not exceed 0.56% in any of the analyzed regions, remaining almost one order of magnitude lower than the 5% acceptance threshold.

In addition to the reduction in average porosity, the relatively low standard deviation values indicate limited local variability among the analyzed regions. This suggests that the residual porosity was more uniformly distributed throughout the specimen than in specimen D.1, further confirming the robustness of the selected process parameters.

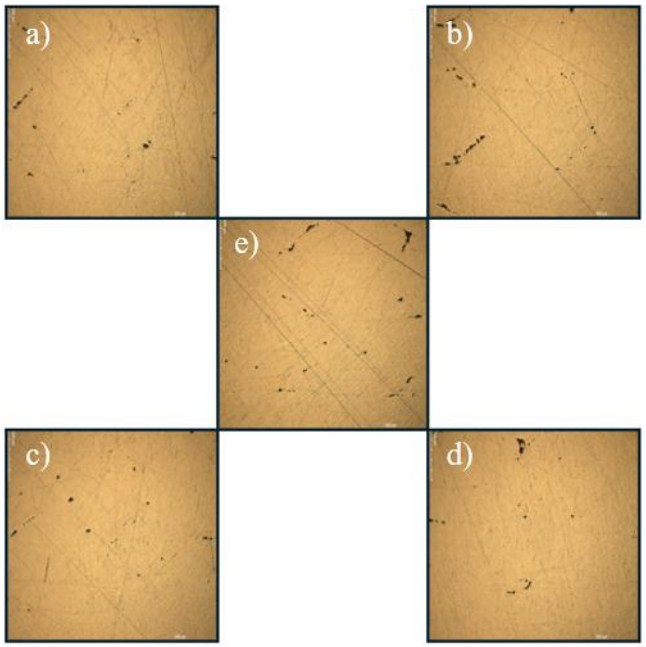


Figure 4.22. *Cube D.2 XY plane micrograph. a) taken from region 1; b) taken from region 2; c) taken from region 3; d) taken from region 4; e) taken from region 5.*

Table 4.17. *Cube D.2 XY plane porosity measurements.*

Region	Max porosity	Min porosity	Average porosity	Standard deviation
1	1.10%	0.46%	0.78%	0.45
2	1.14%	0.54%	0.84%	0.42
3	0.71%	0.25%	0.48%	0.33
4	0.46%	0.16%	0.31%	0.21
5	0.71%	0.46%	0.59%	0.18

Although the XY plane exhibited slightly higher average porosity and greater local variability than the YZ plane, the measured values remained consistently low throughout the analyzed specimen. In particular, the maximum porosity did not exceed 1.14. These results confirm that the optimized process parameters enabled the production of a dense component regardless of the observation plane, while indicating only limited anisotropy in the spatial distribution of residual porosity.

4.2.3.3 Parameters validation

Since specimen D.2 did not fully meet the intended geometrical specifications, and this was considered likely to be associated with heat accumulation during deposition, an additional specimen was manufactured to further assess the process. Instead of a cube, a parallelepiped with dimensions of 45x20x10 mm was deposited. The increased dimensions allowed a longer time interval between successive laser passes over the same area, thereby promoting more effective heat dissipation during the deposition process. Following deposition, the dimensions of the as-built component were measured and found to be compliant with the design specifications, even though some material accumulation was present at the top corners. The as-built specimen is shown in Figure 4.23. This additional manufacturing trial demonstrated that increasing the specimen dimensions enabled the production of a geometrically compliant component while maintaining the optimized

process parameters. These observations suggest that, in addition to process parameter optimization, the thermal conditions experienced during deposition should also be considered when manufacturing LP-DED components.

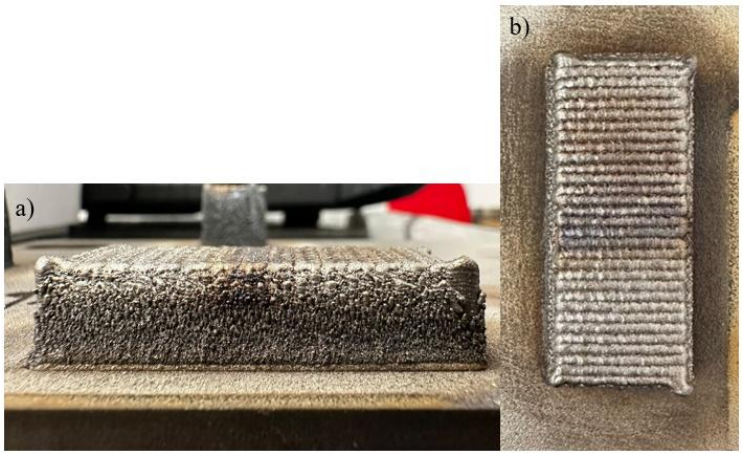


Figure 4.23. *Specimen D.3 a) side view; b) top view.*

4.3 TENSILE TEST

The tensile specimen was manufactured during the second manufacturing trial, before the production of specimens D.1 and D.2. Therefore, the process parameters selected for specimen C.2 were adopted for its deposition. The tensile test was subsequently performed according to the procedure described in Section 3.9. The tensile properties are reported in Table 4.13. Both the yield strength and the ultimate tensile strength (UTS) exceeded the minimum values required, although the corresponding acceptance limits cannot be disclosed. Compared with the results reported by Colon et al. [117], the yield strength obtained in the present study was 6.95% higher, whereas the UTS was 12.5% lower. It should be noted, however, that the specimens investigated by Colon et al. underwent a stress-relief heat treatment prior to testing, whereas the specimen examined in the present work was tested in the as-built condition. The most significant difference concerns the elongation at fracture, which was substantially lower than the value of approximately 10% typically reported for as-built C103 alloy. This result suggests that, despite the satisfactory strength values, the deposited material still exhibited limited ductility under tensile loading. The residual porosity observed in specimen C.2 indicates that additional process optimization may further improve the mechanical performance of the deposited material. A reduction in porosity is expected to have a beneficial effect on the elongation at break, which is generally the mechanical property most sensitive to internal defects.

Although the measured tensile properties were not fully compliant with the third-party acceptance criteria, both the Young's modulus and the elongation at break were consistent with the values typically reported for cold-rolled C103 alloy [140].

Table 4.18. *C103 specimen mechanical properties.*

Properties	Values
Elongation at break [%]	3.12
Force at Break [kN]	3.47
Young modulus [GPa]	87.85
0.2% offset Yield strength [MPa]	333.67
Ultimate tensile strength [MPa]	371.02



Figure 4.24. *Tensile test specimen after failure.*

Figure 4.24 shows the two halves of the tensile specimen after fracture. Failure occurred within the gauge section, indicating that the specimen fractured in the intended testing region. A limited reduction in cross-sectional area is observed near the fracture location, suggesting restricted plastic deformation prior to failure. The fracture surfaces exhibit a macroscopically irregular morphology. Overall, the limited necking observed is consistent with the relatively low elongation at break measured during the tensile test.

4.4 CASE-STUDY COMPONENT

Following the assessment of the mechanical properties, a case-study component was manufactured using the process parameters adopted for specimen C.2. Due to confidentiality constraints the final geometry of the component can be disclosed; therefore, only the as-built component is shown in Figure 4.25. Consistently with the previous manufacturing trial, the component was deposited onto a cylindrical Ti6Al4V substrate, which was adequately pre-heated prior to deposition. As observed in the previously manufactured specimens, powder particle adhesion was also observed on the case-study component, particularly on its planar surfaces. Conversely, no significant powder accumulation was observed on the inclined portion of the component. This difference may be attributed to the effect of the component geometry on powder-particle deposition and removal: the inclination of the surface may have facilitated the evacuation of loosely deposited particles from the deposition area, reducing their accumulation compared with the planar surfaces.

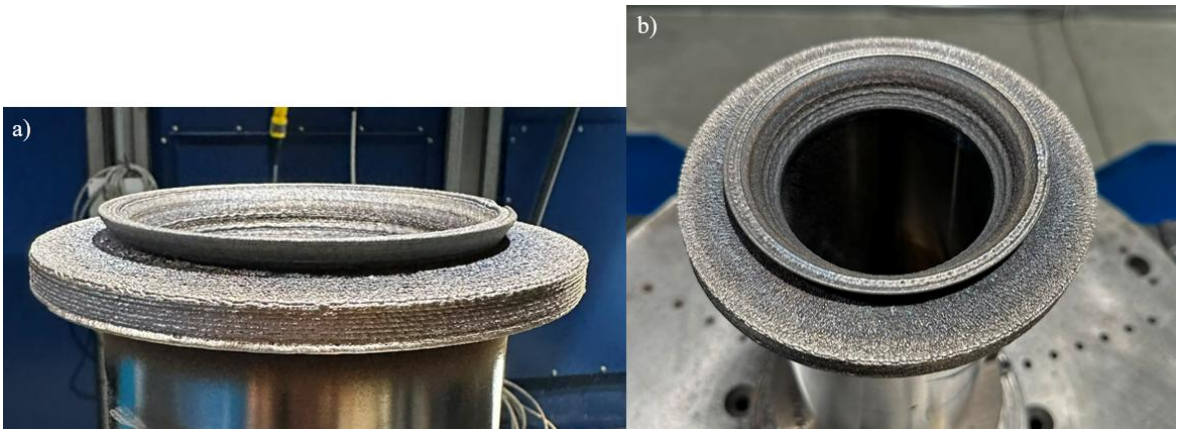


Figure 4.25. *As-built case-study component. a) side view; b) top view.*

5 CONCLUSIONS AND FUTURE WORK

This work investigated the development of suitable process parameters for the fabrication of C103 niobium alloy by Laser Powder Directed Energy Deposition. Starting from the available literature, an experimental methodology based on the progressive refinement of the process parameters was developed and validated through successive manufacturing trials. The adopted approach enabled the systematic optimization of the deposition process by progressively refining the laser power, scanning speed, powder feed rate and layer thickness according to the experimental observations obtained after each manufacturing stage. The proposed optimization strategy successfully identified a process parameter set capable of producing C103 specimens with an average relative density of 99.50%, largely exceeding the minimum target of 95% established at the beginning of this work. The porosity analyses performed on both the YZ and XY cross-sections, demonstrated a progressive reduction of deposition defects throughout the experimental campaign. In particular, the final manufacturing trial showed a reduction of approximately 70% in average porosity compared with the previous parameter set, confirming the effectiveness of the adopted iterative optimization strategy.

The developed process was further validated through the manufacture of a tensile specimen and a representative case-study component. Although the tensile specimen was manufactured before completion of the optimization procedure, the measured yield strength and ultimate tensile strength satisfied the requirements, while the limited elongation at failure suggests that further improvements in process optimization are still possible. Moreover, the successful manufacture of the case-study component demonstrated the feasibility of producing C103 alloy parts by LP-DED using the developed process parameters.

An additional outcome of this work concerns the influence of component geometry on the final manufacturing quality. The experimental results showed that, despite the adoption of optimized process parameters, heat accumulation associated with small component dimensions can significantly affect the final geometrical accuracy. This observation highlights that successful process development for LP-DED should not rely exclusively on process parameter optimization but should also consider the thermal history associated with component geometry.

Overall, this work provides a systematic methodology for the development of LP-DED process parameters for C103 alloy and demonstrates the potential of this technology for manufacturing high-density C103 niobium alloy components for demanding aerospace applications.

Future work should focus on validating the optimized parameter set through tensile testing to assess whether the improved porosity levels translate into enhanced ductility in the as-built condition. In addition, further process optimization aimed at increasing deposition productivity, for example through higher layer thicknesses or scanning speeds while maintaining near full density, would facilitate the industrial implementation of LP-DED for large C103 components.

6 REFERENCES

[1] M. Ghobakhloo, "Industry 4.0, digitization, and opportunities for sustainability," Apr. 10, 2020, *Elsevier Ltd*. doi: 10.1016/j.jclepro.2019.119869.

[2] A. G. Frank, L. S. Dalenogare, and N. F. Ayala, "Industry 4.0 technologies: Implementation patterns in manufacturing companies," *Int. J. Prod. Econ.*, vol. 210, pp. 15–26, Apr. 2019, doi: 10.1016/j.ijpe.2019.01.004.

[3] A. Martinelli, A. Mina, and M. Moggi, "The enabling technologies of industry 4.0: Examining the seeds of the fourth industrial revolution," *Industrial and Corporate Change*, vol. 30, no. 1, pp. 161–188, Feb. 2021, doi: 10.1093/icc/dtaa060.

[4] J. Müller, "Enabling Technologies for Industry 5.0 Results of a workshop with Europe's technology leaders," 2020, doi: 10.2777/082634.

[5] Maija. Breque, Lars. De Nul, and Athanasios. Petridis, *Industry 5.0 : towards a sustainable, human-centric and resilient European industry*. Publications Office of the European Union, 2021.

[6] "Additive manufacturing - General principles -Fundamentals and vocabulary (ISO/ASTM 52900:2021)," British Standards Institution, 2022.

[7] W. E. Frazier, "Metal additive manufacturing: A review," 2014, *Springer New York LLC*. doi: 10.1007/s11665-014-0958-z.

[8] M. Jiménez, L. Romero, I. A. Domínguez, M. D. M. Espinosa, and M. Domínguez, "Additive Manufacturing Technologies: An Overview about 3D Printing Methods and Future Prospects," *Complexity*, vol. 2019, 2019, doi: 10.1155/2019/9656938.

[9] I. Gibson, D. Rosen, and B. Stucker, *Additive Manufacturing Technologies 3D Printing, Rapid Prototyping, and Direct Digital Manufacturing Second Edition*, Second. Springer.

[10] M. K. Thompson *et al.*, "Design for Additive Manufacturing: Trends, opportunities, considerations, and constraints," *CIRP Ann. Manuf. Technol.*, vol. 65, no. 2, pp. 737–760, 2016, doi: 10.1016/j.cirp.2016.05.004.

[11] L. Zhou *et al.*, "Additive Manufacturing: A Comprehensive Review," May 01, 2024, *Multidisciplinary Digital Publishing Institute (MDPI)*. doi: 10.3390/s24092668.

[12] M. Armstrong, H. Mehrabi, and N. Naveed, "An overview of modern metal additive manufacturing technology," Dec. 01, 2022, *Elsevier Ltd*. doi: 10.1016/j.jmapro.2022.10.060.

[13] K. S. Prakash, T. Nancharaih, and V. V. S. Rao, "ScienceDirect Additive Manufacturing Techniques in Manufacturing-An Overview," 2017. [Online]. Available: www.sciencedirect.com

[14] S. Mirzababaei and S. Pasebani, "A review on binder jet additive manufacturing of 316L stainless steel," Sep. 01, 2019, *MDPI Multidisciplinary Digital Publishing Institute*. doi: 10.3390/jmmp3030082.

[15] A. Mostafaei *et al.*, "Binder jet 3D printing—Process parameters, materials, properties, modeling, and challenges," Jun. 01, 2021, *Elsevier Ltd*. doi: 10.1016/j.pmatsci.2020.100707.

[16] A. Dass and A. Moridi, "State of the art in directed energy deposition: From additive manufacturing to materials design," 2019, *MDPI AG*. doi: 10.3390/COATINGS9070418.

[17] N. Matthews, “Additive Metal Technologies for Aerospace Sustainment,” in *Aircraft Sustainment and Repair*, Elsevier, 2018, pp. 845–862. doi: 10.1016/B978-0-08-100540-8.00015-7.
[18] A. Oleff, B. Küster, M. Stonis, and L. Overmeyer, “Process monitoring for material extrusion additive manufacturing: a state-of-the-art review,” Dec. 01, 2021, *Springer Science and Business Media Deutschland GmbH*. doi: 10.1007/s40964-021-00192-4.
[19] J. Gonzalez-Gutierrez, S. Cano, S. Schuschnigg, C. Kukla, J. Sapkota, and C. Holzer, “Additive Manufacturing of Metallic and Ceramic Components by the Material Extrusion of Highly-Filled Polymers: A Review and Future Perspectives,” *Materials*, vol. 11, no. 5, p. 840, May 2018, doi: 10.3390/ma11050840.
[20] Martin. Leary, *Design for additive manufacturing*. Elsevier, 2020.
[21] D. Moreno Nieto and S. I. Molina, “Large-format fused deposition additive manufacturing: a review,” *Rapid Prototyp. J.*, vol. 26, no. 5, pp. 793–799, May 2020, doi: 10.1108/RPJ-05-2018-0126.
[22] L. Bottini, A. Boschetto, F. Veniali, and P. Gaudenzi, “Additive manufacturing for CubeSat structure fabrication,” in *Next Generation CubeSats and SmallSats*, Elsevier, 2023, pp. 153–180. doi: 10.1016/B978-0-12-824541-5.00025-X.
[23] Martin. Leary, *Design for additive manufacturing*. Elsevier, 2020.
[24] O. Gülcan, K. Günaydın, and A. Tamer, “The state of the art of material jetting—a critical review,” Aug. 02, 2021, *MDPI AG*. doi: 10.3390/polym13162829.
[25] P. O’Neill, L. Jolivet, N. J. Kent, and D. Brabazon, “Physical integrity of 3D printed parts for use as embossing tools,” *Advances in Materials and Processing Technologies*, vol. 3, no. 3, pp. 308–317, Jul. 2017, doi: 10.1080/2374068X.2017.1330842.
[26] L. Ladani and M. Sadeghilaridjani, “Review of Powder Bed Fusion Additive Manufacturing for Metals,” *Metals (Basel).*, vol. 11, no. 9, p. 1391, Sep. 2021, doi: 10.3390/met11091391.
[27] T. DebRoy *et al.*, “Additive manufacturing of metallic components – Process, structure and properties,” Mar. 01, 2018, *Elsevier Ltd*. doi: 10.1016/j.pmatsci.2017.10.001.
[28] N. D. Dejene and H. G. Lemu, “Current Status and Challenges of Powder Bed Fusion-Based Metal Additive Manufacturing: Literature Review,” *Metals (Basel).*, vol. 13, no. 2, p. 424, Feb. 2023, doi: 10.3390/met13020424.
[29] Fraunhofer Institute for Manufacturing Technology and Advanced Materials IFAM, “Laser Powder Bed Fusion (PBF-LB/M).” Accessed: Jun. 30, 2026. [Online]. Available: https://www.ifam.fraunhofer.de/en/technologies/laser-beam-melting.html
[30] M. Zenou and L. Grainger, “Additive manufacturing of metallic materials,” in *Additive Manufacturing: Materials, Processes, Quantifications and Applications*, Elsevier, 2018, pp. 53–103. doi: 10.1016/B978-0-12-812155-9.00003-7.
[31] P. M. Bhatt, A. M. Kabir, M. Peralta, H. A. Bruck, and S. K. Gupta, “A robotic cell for performing sheet lamination-based additive manufacturing,” *Addit. Manuf.*, vol. 27, pp. 278–289, May 2019, doi: 10.1016/j.addma.2019.02.002.
[32] A. Kumar, A. R. Dixit, and S. Sreenivasa, “Mechanical properties of additively manufactured polymeric composites using sheet lamination technique and fused deposition modeling: A review,” *Polym. Adv. Technol.*, vol. 35, no. 4, Apr. 2024, doi: 10.1002/pat.6396.

[33] A. Pilipović, “Sheet lamination,” in *Polymers for 3D Printing*, J. Izdebska-Podsiadły, Ed., Elsevier, 2022, ch. 11, pp. 127–136. doi: 10.1016/B978-0-12-818311-3.00008-2.

[34] M. Pagac *et al.*, “A review of vat photopolymerization technology: Materials, applications, challenges, and future trends of 3d printing,” Feb. 02, 2021, *MDPI AG*. doi: 10.3390/polym13040598.

[35] J. V. Crivello and E. Reichmanis, “Photopolymer Materials and Processes for Advanced Technologies,” *Chemistry of Materials*, vol. 26, no. 1, pp. 533–548, Jan. 2014, doi: 10.1021/cm402262g.

[36] A. Al Rashid, W. Ahmed, M. Y. Khalid, and M. Koç, “Vat photopolymerization of polymers and polymer composites: Processes and applications,” *Addit. Manuf.*, vol. 47, p. 102279, Nov. 2021, doi: 10.1016/j.addma.2021.102279.

[37] O. R. Mireles, O. Rodriguez, Y. Gao, and N. Philips, “Additive manufacture of refractory alloy c103 for propulsion applications,” in *AIAA Propulsion and Energy 2020 Forum*, American Institute of Aeronautics and Astronautics Inc, AIAA, 2020, pp. 1–13. doi: 10.2514/6.2020-3500.

[38] B. J. Colón *et al.*, “Parameter development and characterization of laser powder directed energy deposition of Nb – Alloy C103 for thin wall geometries,” *Journal of Materials Research and Technology*, vol. 30, pp. 5028–5039, May 2024, doi: 10.1016/j.jmrt.2024.04.200.

[39] S. . Bobba, S. . Carrara, J. . Huisman, F. . Mathieux, and C. . Pavel, *Critical raw materials for strategic technologies and sectors in the EU : a foresight study*. Publications Office of the European Union, 2020.

[40] M. Schmidt *et al.*, “Laser based additive manufacturing in industry and academia,” *CIRP Annals*, vol. 66, no. 2, pp. 561–583, 2017, doi: 10.1016/j.cirp.2017.05.011.

[41] D. G. Ahn, “Directed Energy Deposition (DED) Process: State of the Art,” Mar. 01, 2021, *Korean Society for Precision Engineeing*. doi: 10.1007/s40684-020-00302-7.

[42] A. Jinoop, C. Paul, and K. Bindra, “Laser-assisted directed energy deposition of nickel super alloys: A review,” *Proceedings of the Institution of Mechanical Engineers, Part L: Journal of Materials: Design and Applications*, vol. 233, no. 11, pp. 2376–2400, Nov. 2019, doi: 10.1177/1464420719852658.

[43] A. Singh, S. Kapil, and M. Das, “A comprehensive review of the methods and mechanisms for powder feedstock handling in directed energy deposition,” Oct. 01, 2020, *Elsevier B.V.* doi: 10.1016/j.addma.2020.101388.

[44] D. G. Ahn, “Direct metal additive manufacturing processes and their sustainable applications for green technology: A review,” Oct. 01, 2016, *Korean Society for Precision Engineering*. doi: 10.1007/s40684-016-0048-9.

[45] D. Ding, Z. Pan, D. Cuiuri, and H. Li, “Wire-feed additive manufacturing of metal components: technologies, developments and future interests,” Oct. 26, 2015, *Springer London*. doi: 10.1007/s00170-015-7077-3.

[46] S. H. Mok, G. Bi, J. Folkes, and I. Pashby, “Deposition of Ti-6Al-4V using a high power diode laser and wire, Part I: Investigation on the process characteristics,” *Surf. Coat. Technol.*, vol. 202, no. 16, pp. 3933–3939, May 2008, doi: 10.1016/j.surfcoat.2008.02.008.

[47] F. Li, S. Chen, J. Shi, H. Tian, and Y. Zhao, “Evaluation and optimization of a hybrid manufacturing process combining wire arc additive manufacturing with milling for

the fabrication of stiffened panels," *Applied Sciences (Switzerland)*, vol. 7, no. 12, Nov. 2017, doi: 10.3390/app7121233.

[48] S. W. Williams, F. Martina, A. C. Addison, J. Ding, G. Pardal, and P. Colegrove, "Wire + Arc Additive Manufacturing," *Materials Science and Technology*, vol. 32, no. 7, pp. 641–647, May 2016, doi: 10.1179/1743284715Y.0000000073.

[49] W. J. Sames, F. A. List, S. Pannala, R. R. Dehoff, and S. S. Babu, "The metallurgy and processing science of metal additive manufacturing," *International Materials Reviews*, vol. 61, no. 5, pp. 315–360, Jul. 2016, doi: 10.1080/09506608.2015.1116649.

[50] A. Dass and A. Moridi, "State of the art in directed energy deposition: From additive manufacturing to materials design," 2019, *MDPI AG*. doi: 10.3390/COATINGS9070418.

[51] E. A. Alberti, B. M. P. Bueno, and A. S. C. M. D'Oliveira, "Additive manufacturing using plasma transferred arc," *International Journal of Advanced Manufacturing Technology*, vol. 83, no. 9–12, pp. 1861–1871, Apr. 2016, doi: 10.1007/s00170-015-7697-7.

[52] M. T. Stawovy, "Comparison of LCAC and PM Mo deposited using Sciaky EBAM™," *Int. J. Refract. Metals Hard Mater.*, vol. 73, pp. 162–167, Jun. 2018, doi: 10.1016/j.ijrmhm.2018.02.009.

[53] S. Negi *et al.*, "Review on electron beam based additive manufacturing," *Rapid Prototyp. J.*, vol. 26, no. 3, pp. 485–498, Nov. 2019, doi: 10.1108/RPJ-07-2019-0182.

[54] M. Motta, A. G. Demir, and B. Previtali, "High-speed imaging and process characterization of coaxial laser metal wire deposition," *Addit. Manuf.*, vol. 22, pp. 497–507, Aug. 2018, doi: 10.1016/j.addma.2018.05.043.

[55] C. R. Heiple, J. R. Roper, R. T. Stagner, and Aden R. J., "Surface-active element effects on the shape of GTA, laser, and electron-beam welds," *Weld.J.*, no. 62, pp. 72–77, 1983.

[56] D. Svetlizky *et al.*, "Directed energy deposition (DED) additive manufacturing: Physical characteristics, defects, challenges and applications," Oct. 01, 2021, *Elsevier B.V.* doi: 10.1016/j.mattod.2021.03.020.

[57] E. O. Olakanmi, R. F. Cochrane, and K. W. Dalgarno, "A review on selective laser sintering/melting (SLS/SLM) of aluminium alloy powders: Processing, microstructure, and properties," *Prog. Mater. Sci.*, vol. 74, pp. 401–477, Oct. 2015, doi: 10.1016/j.pmatsci.2015.03.002.

[58] F. M. Sciammarella and B. Salehi Najafabadi, "Processing Parameter DOE for 316L Using Directed Energy Deposition," *Journal of Manufacturing and Materials Processing*, vol. 2, no. 3, p. 61, Sep. 2018, doi: 10.3390/jmmp2030061.

[59] D. Svetlizky *et al.*, "Directed energy deposition of Al 5xxx alloy using Laser Engineered Net Shaping (LENS®)," *Mater. Des.*, vol. 192, p. 108763, Jul. 2020, doi: 10.1016/j.matdes.2020.108763.

[60] V. Manvatkar, A. De, and T. DebRoy, "Spatial variation of melt pool geometry, peak temperature and solidification parameters during laser assisted additive manufacturing process," *Materials Science and Technology*, vol. 31, no. 8, pp. 924–930, Jun. 2015, doi: 10.1179/1743284714Y.0000000701.

[61] Y. Zhou, S. Chen, X. Chen, T. Cui, J. Liang, and C. Liu, "The evolution of bainite and mechanical properties of direct laser deposition 12CrNi2 alloy steel at different

laser power," *Materials Science and Engineering: A*, vol. 742, pp. 150–161, Jan. 2019, doi: 10.1016/j.msea.2018.10.092.

[62] H. Siva Prasad, F. Brueckner, and A. F. H. Kaplan, "Powder catchment in laser metal deposition," *J. Laser Appl.*, vol. 31, no. 2, May 2019, doi: 10.2351/1.5096130.

[63] I. J. Spalding, "Applied Laser Tooling," *J. Mod. Opt.*, vol. 35, no. 5, pp. 754–755, May 1988, doi: 10.1080/09500348814550811.

[64] M. L. Griffith *et al.*, "Understanding thermal behavior in the LENS process," *Mater. Des.*, vol. 20, no. 2–3, pp. 107–113, Jun. 1999, doi: 10.1016/S0261-3069(99)00016-3.

[65] V. Manvatkar, A. De, and T. DebRoy, "Heat transfer and material flow during laser assisted multi-layer additive manufacturing," *J. Appl. Phys.*, vol. 116, no. 12, Sep. 2014, doi: 10.1063/1.4896751.

[66] B. A. Szost *et al.*, "A comparative study of additive manufacturing techniques: Residual stress and microstructural analysis of CLAD and WAAM printed Ti–6Al–4V components," *Mater. Des.*, vol. 89, pp. 559–567, Jan. 2016, doi: 10.1016/j.matdes.2015.09.115.

[67] K. Carpenter and A. Tabei, "On Residual Stress Development, Prevention, and Compensation in Metal Additive Manufacturing," *Materials*, vol. 13, no. 2, p. 255, Jan. 2020, doi: 10.3390/ma13020255.

[68] N. S. Rossini, M. Dassisti, K. Y. Benyounis, and A. G. Olabi, "Methods of measuring residual stresses in components," *Mater. Des.*, vol. 35, pp. 572–588, Mar. 2012, doi: 10.1016/j.matdes.2011.08.022.

[69] D. J. Corbin, A. R. Nassar, E. W. Reutzel, A. M. Beese, and P. Michaleris, "Effect of Substrate Thickness and Preheating on the Distortion of Laser Deposited Ti–6Al–4V," *J. Manuf. Sci. Eng.*, vol. 140, no. 6, Jun. 2018, doi: 10.1115/1.4038890.

[70] A. Vasinonta, J. L. Beuth, and M. Griffith, "Process Maps for Predicting Residual Stress and Melt Pool Size in the Laser-Based Fabrication of Thin-Walled Structures," *J. Manuf. Sci. Eng.*, vol. 129, no. 1, pp. 101–109, Feb. 2007, doi: 10.1115/1.2335852.

[71] W. Woo, D.-K. Kim, Ed. J. Kingston, V. Luzin, F. Salvemini, and M. R. Hill, "Effect of interlayers and scanning strategies on through-thickness residual stress distributions in additive manufactured ferritic-austenitic steel structure," *Materials Science and Engineering: A*, vol. 744, pp. 618–629, Jan. 2019, doi: 10.1016/j.msea.2018.12.078.

[72] H. Yamaguchi, O. Fergani, and P.-Y. Wu, "Modification using magnetic field-assisted finishing of the surface roughness and residual stress of additively manufactured components," *CIRP Annals*, vol. 66, no. 1, pp. 305–308, 2017, doi: 10.1016/j.cirp.2017.04.084.

[73] W. Guo *et al.*, "Laser shock peening of laser additive manufactured Ti6Al4V titanium alloy," *Surf. Coat. Technol.*, vol. 349, pp. 503–510, Sep. 2018, doi: 10.1016/j.surfcoat.2018.06.020.

[74] C. Zhao *et al.*, "Critical instability at moving keyhole tip generates porosity in laser melting," *Science (1979).*, vol. 370, no. 6520, pp. 1080–1086, Nov. 2020, doi: 10.1126/science.abd1587.

[75] A. W. Prabhu, T. Vincent, A. Chaudhary, W. Zhang, and S. S. Babu, "Effect of microstructure and defects on fatigue behaviour of directed energy deposited Ti–6Al–4V," *Science and Technology of Welding and Joining*, vol. 20, no. 8, pp. 659–669, Nov. 2015, doi: 10.1179/1362171815Y.0000000050.

[76] D. Nursyifaulkhair, N. Park, E. R. Baek, and J. Lee, “Effect of Process Parameters on the Formation of Lack of Fusion in Directed Energy Deposition of Ti-6Al-4V Alloy,” *Journal of Welding and Joining*, vol. 37, no. 6, pp. 579–584, Dec. 2019, doi: 10.5781/JWJ.2019.37.6.7.

[77] R. Snell *et al.*, “Methods for Rapid Pore Classification in Metal Additive Manufacturing,” *JOM*, vol. 72, no. 1, pp. 101–109, Jan. 2020, doi: 10.1007/s11837-019-03761-9.

[78] S.-H. Li, P. Kumar, S. Chandra, and U. Ramamurty, “Directed energy deposition of metals: processing, microstructures, and mechanical properties,” *International Materials Reviews*, vol. 68, no. 6, pp. 605–647, Aug. 2023, doi: 10.1080/09506608.2022.2097411.

[79] D. Herzog, V. Seyda, E. Wycisk, and C. Emmelmann, “Additive manufacturing of metals,” *Acta Mater.*, vol. 117, pp. 371–392, Sep. 2016, doi: 10.1016/j.actamat.2016.07.019.

[80] A. J. Sterling, B. Torries, N. Shamsaei, S. M. Thompson, and D. W. Seely, “Fatigue behavior and failure mechanisms of direct laser deposited Ti–6Al–4V,” *Materials Science and Engineering: A*, vol. 655, pp. 100–112, Feb. 2016, doi: 10.1016/j.msea.2015.12.026.

[81] M. N. Ahsan, R. Bradley, and A. J. Pinkerton, “Microcomputed tomography analysis of intralayer porosity generation in laser direct metal deposition and its causes,” *J. Laser Appl.*, vol. 23, no. 2, May 2011, doi: 10.2351/1.3582311.

[82] Y. Liu *et al.*, “Optimization of parameters in laser powder deposition AlSi10Mg alloy using Taguchi method,” *Opt. Laser Technol.*, vol. 111, pp. 470–480, Apr. 2019, doi: 10.1016/j.optlastec.2018.10.030.

[83] A. W. Prabhu, T. Vincent, A. Chaudhary, W. Zhang, and S. S. Babu, “Effect of microstructure and defects on fatigue behaviour of directed energy deposited Ti–6Al–4V,” *Science and Technology of Welding and Joining*, vol. 20, no. 8, pp. 659–669, Nov. 2015, doi: 10.1179/1362171815Y.0000000050.

[84] P. A. Kobryn and S. L. Semiatin, “Mechanical Properties of Laser-Deposited Ti-6Al-4V,” *2001 International Solid Freeform Fabrication Symposium*, pp. 179–186, 2021, doi: http://dx.doi.org/10.26153/tsw/3261.

[85] M. Rott *et al.*, “In-situ directed energy deposition of Al based low density steel for automotive applications,” *Sci. Rep.*, vol. 13, no. 1, Dec. 2023, doi: 10.1038/s41598-023-49026-z.

[86] W. J. Sames, F. A. List, S. Pannala, R. R. Dehoff, and S. S. Babu, “The metallurgy and processing science of metal additive manufacturing,” *International Materials Reviews*, vol. 61, no. 5, pp. 315–360, Jul. 2016, doi: 10.1080/09506608.2015.1116649.

[87] H. L. Wei *et al.*, “Mechanistic models for additive manufacturing of metallic components,” *Prog. Mater. Sci.*, vol. 116, p. 100703, Feb. 2021, doi: 10.1016/j.pmatsci.2020.100703.

[88] S. Kou, “Solidification and liquation cracking issues in welding,” *JOM*, vol. 55, no. 6, pp. 37–42, Jun. 2003, doi: 10.1007/s11837-003-0137-4.

[89] E. Yasa, O. Poyraz, E. U. Solakoglu, G. Akbulut, and S. Oren, “A Study on the Stair Stepping Effect in Direct Metal Laser Sintering of a Nickel-based Superalloy,” *Procedia CIRP*, vol. 45, pp. 175–178, 2016, doi: 10.1016/j.procir.2016.02.068.

[90] H. Masuo *et al.*, “Effects of Defects, Surface Roughness and HIP on Fatigue Strength of Ti-6Al-4V manufactured by Additive Manufacturing,” *Procedia Structural Integrity*, vol. 7, pp. 19–26, 2017, doi: 10.1016/j.prostr.2017.11.055.

[91] G. K. Lewis and E. Schlienger, “Practical considerations and capabilities for laser assisted direct metal deposition,” *Mater. Des.*, vol. 21, no. 4, pp. 417–423, Aug. 2000, doi: 10.1016/S0261-3069(99)00078-3.

[92] G. Piscopo and L. Iuliano, “Current research and industrial application of laser powder directed energy deposition,” *The International Journal of Advanced Manufacturing Technology*, vol. 119, no. 11–12, pp. 6893–6917, Apr. 2022, doi: 10.1007/s00170-021-08596-w.

[93] L. Xue, “Laser Consolidation—A Rapid Manufacturing Process for Making Net-Shape Functional Components,” in *Advances in Laser Materials Processing*, Elsevier, 2018, pp. 461–505. doi: 10.1016/B978-0-08-101252-9.00016-9.

[94] M. N. Ahsan, C. P. Paul, L. M. Kukreja, and A. J. Pinkerton, “Porous structures fabrication by continuous and pulsed laser metal deposition for biomedical applications; modelling and experimental investigation,” *J. Mater. Process. Technol.*, vol. 211, no. 4, pp. 602–609, Apr. 2011, doi: 10.1016/j.jmatprotec.2010.11.014.

[95] V. Boehm, “Hybrid Manufacturing of Turbine Components,” *Laser Technik Journal*, vol. 13, no. 2, pp. 44–47, Apr. 2016, doi: 10.1002/latj.201600013.

[96] A. Saboori, A. Aversa, G. Marchese, S. Biamino, M. Lombardi, and P. Fino, “Application of Directed Energy Deposition-Based Additive Manufacturing in Repair,” *Applied Sciences*, vol. 9, no. 16, p. 3316, Aug. 2019, doi: 10.3390/app9163316.

[97] S. Nowotny, S. Scharek, E. Beyer, and K.-H. Richter, “Laser Beam Build-Up Welding: Precision in Repair, Surface Cladding, and Direct 3D Metal Deposition,” *Journal of Thermal Spray Technology*, vol. 16, no. 3, pp. 344–348, Aug. 2007, doi: 10.1007/s11666-007-9028-5.

[98] L. J. Kumar and C. G. Krishnadas Nair, “Current Trends of Additive Manufacturing in the Aerospace Industry,” in *Advances in 3D Printing & Additive Manufacturing Technologies*, Singapore: Springer Singapore, 2017, pp. 39–54. doi: 10.1007/978-981-10-0812-2_4.

[99] A. Gasser, G. Backes, I. Kelbassa, A. Weisheit, and K. Wissenbach, “Laser Additive Manufacturing,” *Laser Technik Journal*, vol. 7, no. 2, pp. 58–63, Feb. 2010, doi: 10.1002/latj.201090029.

[100] J. M. Wilson, C. Piya, Y. C. Shin, F. Zhao, and K. Ramani, “Remanufacturing of turbine blades by laser direct deposition with its energy and environmental impact analysis,” *J. Clean. Prod.*, vol. 80, pp. 170–178, Oct. 2014, doi: 10.1016/j.jclepro.2014.05.084.

[101] S. Jhavar, C. P. Paul, and N. K. Jain, “Causes of failure and repairing options for dies and molds: A review,” *Eng. Fail. Anal.*, vol. 34, pp. 519–535, Dec. 2013, doi: 10.1016/j.engfailanal.2013.09.006.

[102] V. Goepp, P. Zwolinski, and E. Caillaud, “Design process and data models to support the design of sustainable remanufactured products,” *Comput. Ind.*, vol. 65, no. 3, pp. 480–490, Apr. 2014, doi: 10.1016/j.compind.2014.02.002.

[103] G. F. Sun *et al.*, “Microstructure and mechanical properties of HSLA-100 steel repaired by laser metal deposition,” *Surf. Coat. Technol.*, vol. 351, pp. 198–211, Oct. 2018, doi: 10.1016/j.surfcoat.2018.07.048.

[104] A. Clare, O. Oyelola, J. Folkes, and P. Farayibi, “Laser cladding for railway repair and preventative maintenance,” *J. Laser Appl.*, vol. 24, no. 3, Aug. 2012, doi: 10.2351/1.4710578.
[105] Y. Zhu, Y. Yang, X. Mu, W. Wang, Z. Yao, and H. Yang, “Study on wear and RCF performance of repaired damage railway wheels: Assessing laser cladding to repair local defects on wheels,” *Wear*, vol. 430–431, pp. 126–136, Jul. 2019, doi: 10.1016/j.wear.2019.04.028.
[106] “Optomec Blisk Repair Solution.” Accessed: Jun. 20, 2026. [Online]. Available: https://www.optomec.com/wp-content/uploads/2014/04/Optomec_LENS_Blisk_Repair_Datasheet.pdf
[107] E. Toyserkani, A. Khajepour, and S. F. Corbin, *Laser Cladding*. CRC Press, 2004. doi: 10.1201/9781420039177.
[108] J. Leunda, C. Soriano, C. Sanz, and V. G. Navas, “Laser Cladding of Vanadium-Carbide Tool Steels for Die Repair,” *Phys. Procedia*, vol. 12, pp. 345–352, 2011, doi: 10.1016/j.phpro.2011.03.044.
[109] P. Kattire, S. Paul, R. Singh, and W. Yan, “Experimental characterization of laser cladding of CPM 9V on H13 tool steel for die repair applications,” *J. Manuf. Process.*, vol. 20, pp. 492–499, Oct. 2015, doi: 10.1016/j.jmapro.2015.06.018.
[110] X. Zhang, W. Li, X. Chen, W. Cui, and F. Liou, “Evaluation of component repair using direct metal deposition from scanned data,” *The International Journal of Advanced Manufacturing Technology*, vol. 95, no. 9–12, pp. 3335–3348, Apr. 2018, doi: 10.1007/s00170-017-1455-y.
[111] T. R. F. Cavalcante, F. E. Mariani, and J. A. A. Diaz, “Additive manufacturing of Inconel 718: A review on microstructures and mechanical properties of DED-LB-processed samples,” *J. Mater. Res.*, vol. 41, no. 1, pp. 2–24, Jan. 2026, doi: 10.1557/s43578-025-01663-y.
[112] N. K. Dey, F. W. Liou, and C. Nedic, “Additive Manufacturing Laser Deposition of Ti-6Al-4V for Aerospace Repair Applications ,” Missouri University of Science & Technology, St Louis, 2013.
[113] H. Qi, M. Azer, and P. Singh, “Adaptive toolpath deposition method for laser net shape manufacturing and repair of turbine compressor airfoils,” *The International Journal of Advanced Manufacturing Technology*, vol. 48, no. 1–4, pp. 121–131, Apr. 2010, doi: 10.1007/s00170-009-2265-7.
[114] Z. Lestan, M. Milfelner, J. Balic, M. Brezocnik, and I. Karabegovic, “Laser deposition of Metco 15E, Colmony 88 and VIM CRU 20 powders on cast iron and low carbon steel,” *The International Journal of Advanced Manufacturing Technology*, vol. 66, no. 9–12, pp. 2023–2028, Jun. 2013, doi: 10.1007/s00170-012-4478-4.
[115] A. Saboori, D. Gallo, S. Biamino, P. Fino, and M. Lombardi, “An Overview of Additive Manufacturing of Titanium Components by Directed Energy Deposition: Microstructure and Mechanical Properties,” *Applied Sciences*, vol. 7, no. 9, p. 883, Aug. 2017, doi: 10.3390/app7090883.
[116] D. Bartkowski and G. Kinal, “Microstructure and wear resistance of Stellite-6/WC MMC coatings produced by laser cladding using Yb:YAG disk laser,” *Int. J. Refract. Metals Hard Mater.*, vol. 58, pp. 157–164, Aug. 2016, doi: 10.1016/j.ijrmhm.2016.04.017.
[117] B. J. Colón, N. Philips, and F. Medina, “Response Surface Methodology for Parameter Development & Mechanical Testing of Laser Powder-Directed Energy

Deposition C103," *Metall. Mater. Trans. A Phys. Metall. Mater. Sci.*, vol. 56, no. 10, pp. 4410–4423, Oct. 2025, doi: 10.1007/s11661-025-07888-0.
[118] B. Colón, M. Pourjam, G. Demeneghi, K. Hazeli, O. Mireles, and F. Medina, "On the Mechanical Behavior of LP-DED C103 Thin-Wall Structures," *Metals (Basel).*, vol. 14, no. 9, Sep. 2024, doi: 10.3390/met14090958.
[119] N. Panicker *et al.*, "Integrated Process and Materials Modeling for Development of Additive Manufacturing of Refractory Materials for Critical Applications," Dec. 2023. [Online]. Available: www.osti.gov
[120] S. Thapliyal *et al.*, "Microstructural heterogeneities in additively manufactured refractory alloy C103 and their implications for room and elevated temperature mechanical behavior," *Materials Science and Engineering: A*, vol. 940, Sep. 2025, doi: 10.1016/j.msea.2025.148520.
[121] D. Palacios, "Statistical methods for process parameter development of Niobium alloy C103," Georgia Insitute of Technology, 2023.
[122] S. Singh, C. Kumar, and S. K. Sah, "Review on laser powder-based directed energy deposition for fabricating functionally graded materials: Microstructure, mechanical behavior, and defect analysis," *J. Laser Appl.*, vol. 37, no. 4, Nov. 2025, doi: 10.2351/7.0001838.
[123] V. V. Satya Prasad, R. G. Baligidad, and A. A. Gokhale, "Niobium and Other High Temperature Refractory Metals for Aerospace Applications," 2017, pp. 267–288. doi: 10.1007/978-981-10-2134-3_12.
[124] N. R. Philips, M. Carl, and N. J. Cunningham, "New Opportunities in Refractory Alloys," *Metallurgical and Materials Transactions A*, vol. 51, no. 7, pp. 3299–3310, Jul. 2020, doi: 10.1007/s11661-020-05803-3.
[125] I. Nowak and M. Ziolek, "Niobium Compounds: Preparation, Characterization, and Application in Heterogeneous Catalysis," *Chem. Rev.*, vol. 99, no. 12, pp. 3603–3624, 1999, doi: 10.1021/cr9800208.
[126] A. Gałaś, M. Krzak, and J. Szlugaj, "Niobium – a critical and conflict raw material of great economic significance – the state of the art," *Gospodarka Surowcami Mineralnymi / Mineral Resources Management*, vol. 40, no. 2, pp. 47–67, 2024, doi: 10.24425/gsm.2024.150827.
[127] E. N. Sheftel and O. A. Bannykh, "Niobium-Base Alloys," 1993.
[128] M. Sankar, R. G. Baligidad, D. V. V. Satyanarayana, and A. A. Gokhale, "Effect of internal oxidation on the microstructure and mechanical properties of C-103 alloy," *Materials Science and Engineering: A*, vol. 574, pp. 104–112, Jul. 2013, doi: 10.1016/j.msea.2013.02.057.
[129] N. Do, M. Cury, C. de, M. Pointer, and R. Alves, "Production of niobium: Overview of processes from the mine to products," *Journal of Mining and Metallurgy A: Mining*, vol. 58, no. 1, pp. 1–20, 2022, doi: 10.5937/JMMA2201001H.
[130] J. Szlugaj and B. Radwanek-Bąk, "Lithium sources and their current use," *Gospodarka Surowcami Mineralnymi - Mineral Resources Management*, pp. 61–88, Mar. 2022, doi: 10.24425/gsm.2022.140613.
[131] D. M. McCaffrey, N. T. Nassar, S. M. Jowitt, A. J. Padilla, and L. R. Bird, "Embedded critical material flow: The case of niobium, the United States, and China," *Resour. Conserv. Recycl.*, vol. 188, p. 106698, Jan. 2023, doi: 10.1016/j.resconrec.2022.106698.

[132] L. S. Bowling *et al.*, “Thermophysical modeling of niobium alloys informs materials selection and design for high-temperature applications,” *Mater. Des.*, vol. 248, Dec. 2024, doi: 10.1016/j.matdes.2024.113456.
[133] M. Vailhe, C. J. Torbet, F. Mignerot, and T. M. Pollock, “Very high cycle fatigue behavior of BCC refractory alloy C103,” *Int. J. Fatigue*, vol. 201, Dec. 2025, doi: 10.1016/j.ijfatigue.2025.109139.
[134] J. A. Halchak, J. L. Cannon, and C. Brown, “Materials for Liquid Propulsion Systems,” in *Aerospace Materials and Applications*, Reston ,VA: American Institute of Aeronautics and Astronautics, Inc., 2018, pp. 641–698. doi: 10.2514/5.9781624104893.0641.0698.
[135] “B654/B654M-25: Specification for Niobium-Hafnium Alloy Foil, Sheet, Strip, and Plate,” Apr. 01, 2025, *ASTM International, West Conshohocken, PA*. doi: 10.1520/B0654_B0654M-25.
[136] J. B. Lambert, “Refractory Metals and Alloys,” in *Properties and Selection: Nonferrous Alloys and Special-Purpose Materials*, ASM International, 1990, pp. 557–585. doi: 10.31399/asm.hb.v02.a0001079.
[137] B. P. Bewlay, P. W. Whiting, A. W. Davis, and C. L. Briant, “Creep Mechanisms in Niobium-Silicide Based In-Situ Composites,” *MRS Proceedings*, vol. 552, p. KK6.11.1, Feb. 1998, doi: 10.1557/PROC-552-KK6.11.1.
[138] H. Okamoto, M. E. Schlesinger, and E. M. Mueller, “Nb (Niobium) Binary Alloy Phase Diagrams,” in *Alloy Phase Diagrams*, ASM International, 2016, pp. 507–514. doi: 10.31399/asm.hb.v03.a0006187.
[139] N. R. Philips, M. Carl, and N. J. Cunningham, “New Opportunities in Refractory Alloys,” *Metallurgical and Materials Transactions A*, vol. 51, no. 7, pp. 3299–3310, Jul. 2020, doi: 10.1007/s11661-020-05803-3.
[140] Ansys Granta Edupack, “Niobium-Hf-Ti alloy, Alloy C-103, cold rolled General information.”
[141] ASTM International, “Test Methods for Tension Testing of Metallic Materials,” Jul. 01, 2025, *ASTM International, West Conshohocken, PA*. doi: 10.1520/E0008_E0008M-25.